

UNIVERSITY OF ALBERTA

**RETRIEVAL AND ANALYSIS OF REMOTELY SENSED
RAINFALL FOR BASIN HYDROLOGIC MODELING**

by

OSCAR ANTHONY KALINGA



A thesis submitted to the Faculty of Graduate Studies and Research
in partial fulfillment of the requirements for the degree of
Doctor of Philosophy

in

WATER RESOURCES ENGINEERING

DEPARTMENT OF CIVIL AND ENVIRONMENTAL ENGINEERING

Edmonton, Alberta

Fall, 2006



Library and
Archives Canada

Bibliothèque et
Archives Canada

Published Heritage
Branch

Direction du
Patrimoine de l'édition

395 Wellington Street
Ottawa ON K1A 0N4
Canada

395, rue Wellington
Ottawa ON K1A 0N4
Canada

Your file *Votre référence*
ISBN: 978-0-494-23050-3
Our file *Notre référence*
ISBN: 978-0-494-23050-3

NOTICE:

The author has granted a non-exclusive license allowing Library and Archives Canada to reproduce, publish, archive, preserve, conserve, communicate to the public by telecommunication or on the Internet, loan, distribute and sell theses worldwide, for commercial or non-commercial purposes, in microform, paper, electronic and/or any other formats.

The author retains copyright ownership and moral rights in this thesis. Neither the thesis nor substantial extracts from it may be printed or otherwise reproduced without the author's permission.

AVIS:

L'auteur a accordé une licence non exclusive permettant à la Bibliothèque et Archives Canada de reproduire, publier, archiver, sauvegarder, conserver, transmettre au public par télécommunication ou par l'Internet, prêter, distribuer et vendre des thèses partout dans le monde, à des fins commerciales ou autres, sur support microforme, papier, électronique et/ou autres formats.

L'auteur conserve la propriété du droit d'auteur et des droits moraux qui protègent cette thèse. Ni la thèse ni des extraits substantiels de celle-ci ne doivent être imprimés ou autrement reproduits sans son autorisation.

In compliance with the Canadian Privacy Act some supporting forms may have been removed from this thesis.

Conformément à la loi canadienne sur la protection de la vie privée, quelques formulaires secondaires ont été enlevés de cette thèse.

While these forms may be included in the document page count, their removal does not represent any loss of content from the thesis.

Bien que ces formulaires aient inclus dans la pagination, il n'y aura aucun contenu manquant.


Canada

Abstract

A satellite rainfall estimation technique (called IMRA) is designed to utilize infrared (IR) brightness temperatures (TBs) as the main input data. It uses Slope and Hessian techniques to determine the cloud-top temperature gradient for discriminating rain/no-rain pixels, and allows for adjustment of derived IR-rainfall estimates using microwave TBs and spatial filtering techniques. IMRA rainfall estimates for the Peace River Basin of Southwest Florida (USA) were assessed by comparing directly with gauge and radar rainfall data, and indirectly with the corresponding streamflow predicted by the SAC-SMA model. Generally, IMRA-Slope provided better rainfall estimates than IMRA-Hessian. The daily predicted streamflow using satellite rainfall estimates was comparable to that of radar and better than the gauge data reflecting the potential of satellite rainfall estimates in hydrologic modeling.

A Haar wavelet scheme was used to merge WSR-88D radar and gauged rainfall data in order to correct the underestimation of radar rainfall depths but at the same time maintain its original spatial variability as much as possible. The scheme was evaluated in terms of streamflow simulated by the semi-distributed, physics-based rainfall-runoff model (DPHM-RS) for the Blue River Basin of South Central Oklahoma (USA) driven by event-based, hourly rainfall data. The tests included the effect of radar data accuracy, radar rainfall spatial variability, model resolution, and

the gauge-radar merging techniques (wavelet scheme versus the Statistical Objective Analysis (SOA) Scheme) on the streamflow simulated by DPHM-RS.

Radar rainfall data simulated more accurate runoff hydrographs than gauged data for convective storms but significantly under-estimated the observed hydrographs for stratiform storms. The data merging schemes (i.e., Wavelet and SOA) substantially reduced radar's under-estimation of observed streamflow hydrographs for stratiform storms, with the wavelet performing better than SOA. The influence of model resolution and spatial variability of rainfall on predicted streamflow was evident, which justifies the expensive and tedious effort to account for spatial variability of rainfall and other basin properties via either dense raingauge monitoring networks, or radar meteorology, or meteorological satellites, and distributed or semi-distributed hydrologic modeling.

Acknowledgement

First, I would like to thank my supervisor Dr. Thian Yew Gan for his constant support, encouragement, stimulating advises, and patient guidance, which helped in re-directing my thinking during the course of research and brought new dimensions to my professional culture. He could not even realize how much I have learned from him, I owe him lots of gratitude.

My sincere appreciation goes to the members of my examination committee: Dr. Lawrence Martz, Dr. Peter Steffler, Dr. Kevin Devito, Dr. Paul Myers, and Dr. Hyongkwan Kim for their valuable comments and suggestions.

I gratefully acknowledge the financial support from the University of Alberta, Natural Sciences and Engineering Research Council of Canada (NSERC), Oklahoma Mesonet and Hydrology Laboratory (HL) of the National Weather Service (NWS) of USA through data provision. Also, my special thanks goes to Mr. Masao Fujinaga of Computing and Network Services for his cheerful assistance in compiling the Unix programs used in processing various satellite data, and Mr. Perry Fedun for his help with computing facilities in Water Resources Section.

My gratitude goes to my parents, sisters, brothers, members of Holy Spirit Lutheran Church in Edmonton, Members of Tanzanian community in Edmonton, friends, and fellow graduate students in the Water Resources program for their support and encouragement throughout my stay in Canada. Special thanks to my wife Evalyne for her patience and understanding, and my daughter Carlyne Leah for providing new joyful dimension to my life.

The chain of my gratitude would be definitely incomplete if I would forget to thank the first cause of this chain, GOD - The Prime Mover; my deepest and sincere gratitude for inspiring and guiding this humble being.

Table of Contents

Chapter 1	Introduction, Literature Review, Research Objectives, and Site Description	1
1.1	Introduction.....	1
1.2	Literature Review on Rainfall Estimation.....	2
1.2.1	Infrared (IR) and Visible (VIS) Rainfall Retrieval.....	3
1.2.2	Microwave (MW) Rainfall Retrieval.....	4
1.2.3	Application of Gauge and Remotely Sensed Rainfall in Basin Hydrology.....	6
1.3	Statement of Problems.....	9
1.4	Research Objectives.....	10
1.5	Study Site Description.....	11
1.6	Organization of Thesis.....	12
	References.....	13
Chapter 2	Estimation of Rainfall from Satellite Data for Basin Scale Hydrologic Modeling	18
2.1	Introduction.....	18
2.2	Peace River Basin (PRB).....	20
2.3	Data Description.....	21
2.3.1	Infrared (IR) and Passive Microwave (MW) Data.....	21
2.3.2	Rainfall and Streamflow Data.....	22
2.4	Infrared-Microwave Rainfall Algorithm (IMRA).....	23
2.4.1	Rain Rate and IR Brightness Temperature (R-TB _{IR}) Relationship...24	
2.4.2	Rain/No-Rain Discrimination.....	25
2.4.2.1	Slope Technique (ST).....	26
2.4.2.2	Hessian Technique (HT).....	26
2.4.2.3	IR Threshold Temperature.....	27
2.4.3	Microwave (MW) Adjustment of IR-Rainfall Rate.....	27

2.4.4	Spatial Smoothing/Filtering.....	29
2.4.4.1	Quad-Smoothing (QS).....	30
2.4.4.2	Median Filtering (MF).....	30
2.4.4.3	Trimming Filter (TF).....	30
2.4.5	Rainfall Rate Computation.....	31
2.5	Assessment of IMRA Rainfall Estimates.....	31
2.5.1	Spatial Evaluation of Rainfall Estimates.....	32
2.5.1.1	Effect of Cloud-Top-Temperature Gradient Factor.....	33
2.5.1.2	Effect of Spatial Smoothing/Filtering.....	34
2.5.1.3	Effect of Microwave (MW) Adjustment Factor.....	35
2.5.2	Point Scale Evaluation of Rainfall Estimates.....	36
2.5.2.1	Cumulative Traces of Rainfall Rates.....	36
2.5.2.2	Daily Comparison of Rainfall Rates at Grid Points.....	38
2.5.2.3	Histograms of Rainfall Rates.....	39
2.5.3	Hydrologic Simulation.....	39
2.5.3.1	Sacramento Soil Moisture Accounting (SAC-SMA) Model.....	41
2.5.3.2	Using IMRA Rainfall Estimates in Hydrologic Modeling...	43
2.6	Summary and Conclusions.....	46
	References.....	48

Chapter 3	Merging of Operational WSR-88D Radar Precipitation Data with Raingauge Measurements using Wavelet Analysis	76
1.3	Introduction.....	76
3.2	Processing of WSR-88D Precipitation Data.....	81
3.3	Study Site and Data Processing.....	82
3.3.1	Blue River Basin (BRB).....	82
3.3.2	Rainfall and Streamflow Data.....	83
3.3.3	Data Processing.....	84
3.4	Accuracy of WSR-88D Stage III Precipitation Data.....	84

3.5	Merging Radar and Gauged Rainfall Data.....	86
3.5.1	Statistical Objective Analysis (SOA) Scheme.....	87
3.5.2	Wavelet Scheme.....	88
3.5.2.1	Wavelet Analysis.....	89
3.5.2.2	Intuitive Description of Mallat Algorithm.....	90
3.5.2.3	Interpolation of Raingauge Data.....	92
3.5.2.4	Data Merging Rule.....	93
3.6	Analysis of Rainfall Data Merging Results.....	94
3.6.1	Original versus Merged Rainfall Data.....	95
3.6.2	Hydrologic Simulation.....	96
3.6.2.1	DPHM-RS Rainfall-Runoff Model.....	98
3.6.2.2	Effect of Merging Radar and Gauge Rainfall on Streamflow Simulation.....	99
3.7	Discussion and Conclusions.....	101
	References.....	106

Chapter 4 Influence of Storm Size and Spatial Variability on Radar Data

	Accuracy and Streamflow Prediction	139
4.1	Introduction.....	139
4.2	Study Site and Data Description.....	142
4.3	Streamflow Prediction Using DPHM-RS Model.....	144
4.4	Analysis of Results.....	146
4.4.1	Comparison of Radar and Gauge Basin MAP over BRB.....	146
4.4.2	Effect of Storm Type on Simulated Water Fluxes.....	148
4.4.3	Effect of Rainfall Spatial Variability on Streamflow Prediction...	150
4.4.4	Effect of Hydrologic Model Resolution on Streamflow Prediction.....	151
4.5	Discussion and Conclusions.....	153
	References.....	155

Chapter 5	Summary, Conclusions and Recommendations	175
5.1	Summary and Conclusions.....	175
5.2	Recommendations for Future Research.....	180
	References.....	182

List of Tables

Table 2.1	Comparison of rainfall rate statistics for IMRA (Threshold, Slope, & Hessian) at three pixel sizes for June 1- July 31, 2002 dataset in HOURLY basis.....	52
Table 2.2	Comparison of rainfall rate statistics for IMRA (Threshold, Slope, & Hessian) at three pixel sizes for August 1- September 30, 2003 dataset in HOURLY basis.....	53
Table 2.3	Comparison of rainfall rate statistics for IMRA (Threshold, Slope, & Hessian) at three pixel sizes for June 1- July 31, 2002 dataset in DAILY basis.....	54
Table 2.4	Comparison of rainfall rate statistics for IMRA (Threshold, Slope, & Hessian) at three pixel sizes for August 1- September 30, 2003 dataset in DAILY basis.....	55
Table 2.5	Rainfall rate statistics for IMRA Slope with MW adjustment (i.e., Threshold + Slope + MW) at three pixel sizes for both 2002 and 2003 dataset in DAILY basis.....	56
Table 2.6	Statistics of the simulated streamflow hydrographs by SAC-SMA model using gauge rainfall data during calibration and validation periods	57
Table 2.7	Statistics of simulated hydrographs by SAC-SMA using gauge, radar, and satellite rainfall data during application period.....	58
Table 3.1	1994-2000 annual information on the selected 89 storms and	

	the corresponding results of accuracy assessment of WSR-88D stage III precipitation data using raingauge data.....	112
Table 3.2	Radar-gauge comparison statistics for storm events observed in 1994 and 1998, where E_f is the efficiency coefficient and RMSE is the root mean square error	119
Table 3.3	Fitted spatial correlation models for hourly WSR-88D radar rainfall data	120
Table 3.4	Six storms used for radar-gauge data merging analysis: Total storm depths recorded by gauge and the radar-gauge differences are shown at each individual gauge site	121
Table 3.5	Statistical measures of original (raingauge and radar) and merged (SOA and wavelet) rainfall data in a 32 x 32 pixels window at 4 x 4 km pixel resolution	122
Table 3.6	Characteristics of the four flood/storm events used in hydrologic simulation.....	123
Table 3.7	Input data of DPHM-RS rainfall-runoff model.....	124
Table 3.8	Calibrated parameters of the DPHM-RS model (modified from Biftu and Gan, 2001)	125
Table 3.9	Statistics of the simulated hydrographs by DPHM-RS model for the merged and original radar/gage rainfall data	126
Table 4.1	Characteristics of the six selected flood/storm events used in the study.....	158
Table 4.2	Area, slope, and dominant soil types for each sub-basin of	

	Blue River Basin.....	159
Table 4.3	Percentage of different land cover types for each sub-basin of Blue River Basin.....	160
Table 4.4	Input data of DPHM-RS model (modified from Biftu and Gan, 2001).....	161
Table 4.5	Statistics of simulated hydrographs by DPHM-RS model for radar and gauge rainfall data.....	162

List of Figures

Figure 2.1	Map of Peace River Basin (Source: U.S. Geological Survey)	59
Figure 2.2	Map showing the Florida TRMM satellite ground-validation site.....	60
Figure 2.3	Collocated IR-Gauge rainfall data used in derivation of R-TB _{IR} power law relation that is used for computing IMRA rainfall estimates.....	61
Figure 2.4	Illustration of sliding window technique (Source: Datta et al., 2003).....	62
Figure 2.5	Illustration of Quad smoothing technique (Source: Datta et al., 2003)	63
Figure 2.6	Daily time series of point gauge rainfall data showing relatively light (2002) and heavy (2003) rainfall rate at three different stations: (a) Bartow, (b) Wauchula, and (c) Punta Gorda	64
Figure 2.7	Time series of hourly mean precipitation over Peace River Basin derived from the gauge-adjusted radar rainfall data for a 31-day period of August 2003.....	65
Figure 2.8	Comparison of daily cumulative satellite rainfall for 2002 dataset at Arcadia station derived by three IMRA techniques with respect to gauge and radar data.....	66
Figure 2.9	Comparison of daily cumulative satellite rainfall for 2003 dataset at Arcadia station derived by three IMRA techniques	

	with respect to gauge and radar data.....	67
Figure 2.10	Comparison of daily rainfall rates from radar and satellite for both 2002 and 2003 datasets at grid points with 20 km pixel resolution.....	68
Figure 2.11	Comparison of daily rainfall rates from radar and satellite for both 2002 and 2003 datasets at grid points with 100 km pixel resolution.....	69
Figure 2.12	Frequency distribution of daily rainfall rate from gauge-adjusted radar and satellite estimates for 2002 dataset at (a) 20 km grid resolution, and (b) 100 km grid resolution.....	70
Figure 2.13	Frequency distribution of daily rainfall rate from gauge-adjusted radar and satellite estimates for 2003 dataset at (a) 20 km grid resolution, and (b) 100 km grid resolution.....	71
Figure 2.14	Conceptualization of the SAC-SMA model illustrating the soil moisture storages, runoff components, and land surface – atmosphere exchanges (Source: Finnerty et al., 1997).....	72
Figure 2.15	Comparison of observed and predicted streamflow hydrographs by SAC-SMA model forced with gauge rainfall data during calibration and validation periods for the lumped basin approach.....	73
Figure 2.16	Observed and predicted streamflow hydrographs by SAC-SMA model forced with satellite rainfall estimates derived by IMRA (a) Slope and (b) Hessian with and without microwave (MW) adjustment.....	74

Figure 2.17	Observed and predicted streamflow hydrographs from gauge, radar, and satellite rainfall estimates for lumped basin case [(a) & (b)] and 4 sub-basins case [(c)].....	75
Figure 3.1	Map indicating WSR-88D radar sites providing coverage to Blue River Basin (BRB) of south central Oklahoma (USA)...	127
Figure 3.2	Scatterplots of hourly precipitation of radar versus raingauge for all storms selected in 1994 at (a) gauge #1, and (b) gauge #6.....	128
Figure 3.3	Scatterplots of hourly precipitation of radar versus raingauge for all storms selected in 1998 at (a) gauge #2, and (b) gauge #6.....	129
Figure 3.4	Spatial correlation functions fitted to hourly WSR-88D radar rainfall data for the BRB.....	130
Figure 3.5	Flow chart showing components of the wavelet rainfall data-merging scheme	131
Figure 3.6	A 2-D discretization grid at scales m and $(m+1)$; solid lines define the original spatial resolution at scale m , dashed lines show the grid size at the next higher dyadic scale $(m+1)$, solid circles shows arbitrary raingauge locations	132
Figure 3.7	Scatterplots of decomposed rainfall fields (mm) between gauge (g) and radar (r) for a typical storm.....	133
Figure 3.8	Total rainfall contour map (mm) for storm # 13 of December 8 (08:00) – 10 (02:00), 1994 with a 4.0mm contour Interval.....	134

Figure 3.9	Total rainfall contour map (mm) for storm # 9 of October 12 (08:00) – 13 (02:00), 1997 with a 3.0mm contour interval.....	135
Figure 3.10	Cumulative rainfall plots for all the six storms used in the radar-gauge merging analysis at the raingauge showing the largest radar underestimation of rainfall.....	136
Figure 3.11	Observed streamflow hydrographs simulated by DPHM-RS model forced by gauged and radar rainfall data during model calibration and validation.....	137
Figure 3.12	Observed streamflow hydrographs simulated by DPHM-RS model forced with gauged, radar, and radar-gauge merged rainfall data.....	138
Figure 4.1	Map of Blue River Basin (BRB) indicating (a) WSR-88D radar sites providing coverage, (b) seven sub-basins, and (c) 57 radar grid points falling within BRB.....	163
Figure 4.2	A schematic diagram showing the major components of DPHM-RS rainfall-runoff model.....	165
Figure 4.3	Kinematic surface runoff response functions for each of the seven sub-basins of Blue River Basin (see Figure 4.1b).....	166
Figure 4.4	Comparison of hourly rainfall measurements (mm) from gauge and radar. Four years of hourly data were used: 1994, 1995, 1998, and 1999.....	167
Figure 4.5	Scatterplots of radar and gauge hourly rainfall data and their corresponding simulated evapotranspiration and soil moisture	168

	at the active layer.....	
Figure 4.6	Total radar and gauged rainfall depths (mm) computed for seven sub-basins of Blue River Basin.....	169
Figure 4.7	Observed streamflow hydrographs simulated by DPHM-RS model forced by gauged and radar rainfall data.....	170
Figure 4.8	Streamflow prediction by radar inputs for averaged (lumped), fully distributed (distributed), one, two, and three grids.....	171
Figure 4.9	Streamflow prediction indicating hydrographs corresponding to radar and raingauge inputs for the case of 5 and 7 sub-basins.....	172
Figure 4.10	Peak flow prediction indicating hydrographs corresponding to radar and raingauge inputs for the case of 5 sub-basins.....	173
Figure 4.11	Kinematic surface runoff response functions of the Blue River Basin for the case of: (a) 20 sub-basins, (b) 13 sub-basins.....	174

Chapter 1

Introduction, Literature Review, Research Objectives, and Site Description

1.1 Introduction

Rainfall is one of the most important driving forces in hydrologic processes. Unfortunately, rainfall is also characterized by high spatial and temporal variability. There are two basic approaches to measure rainfall. The first is to measure rainfall with a raingauge, which is essentially a measuring cylinder. Raingauges generally measure accurate rainfall depths at a point scale, even though they suffer from measurement errors associated with the shape of the container, its exposure, the wind effect, and evaporation loss between measurements (e.g., Legates and DeLiberty, 1993; Groisman and Legates, 1994). Ideally, a dense network of raingauges can provide accurate estimates of the spatial distribution of rainfall. However, such a network is simply not practical because of prohibitive cost and sometimes also because of poor accessibility in remote sites.

The second approach of rainfall measurement is via some sort of remote sensors that are airborne, spaceborne, or ground-based and operate in the visible, infrared,

and microwave spectra. These sensors may be further subdivided into direct sensors where the sizes of precipitation droplets are measured and indirect sensors where some by-products of the precipitation process, such as clouds, are measured. Weather radar is one good example of direct sensors and developed countries such as the United States uses weather radar networks for operational rainfall measurements, e.g., Weather Surveillance Radar -1988 Doppler (WSR-88D) of USA (Crum and Alberty, 1993). However, if the radar beam originates from the ground surface (i.e., ground-based radar), within a few hundred kilometers it will reach a height that is mostly above majority of the precipitation droplets. This limits the area over which any one radar sensor may be used.

Since both raingauges and ground-based weather radars are limited in terms of cost and accessibility, one possible and practical solution is to use space borne satellite data. Useful rainfall data can be derived from satellites designed primarily for meteorological purposes, including polar orbiters such as Defense Meteorological Satellite Program (DMSP) and Tropical Rainfall Measuring Mission (TRMM) (Simpson et al., 1996), and geostationary satellites such as Geostationary Operational Environmental Satellite (GOES), Geostationary Meteorological Satellite (GMS), and Meteorological Satellite (METEOSAT) (e.g., Vicente et al., 1998; Chen and Li, 2002; Andersen et al., 2002). Geostationary satellites provide visible and infrared images with information about the cloud tops, while polar-orbiting satellites provide microwave signals that respond primarily to precipitation-sized water droplets within the clouds (e.g., Chen and Li, 2000).

1.2 Literature Review on Rainfall Estimation

The shortage of ground-based (i.e., gauge and radar) rainfall measurements over vast regions of the world landmasses is well known. This poses a problem for improving hydrologic modeling of large river basins particularly in developing countries (e.g., Andersen et al., 2002). Although imperfect, satellite observations

offer the only realistic means of estimating rainfall over large catchments. Satellite-based techniques for measuring precipitation exist for visible (VIS), infrared (IR), and microwave radiation. The visible and infrared sensors have the advantage that they can reside on geostationary space platforms. Therefore good spatial resolution (about 4 km x 4 km) visible and IR images are available on a global scale at 30-minutes or 1-hour intervals (Clark, 1983; Arkin and Meisner, 1987; Xu et al., 1999). Geostationary satellites' IR and VIS measurements correspond to the cloud-top brightness temperature, which is indirectly related to surface rainfall. In contrast, passive microwave (MW) radiation interacts strongly with raindrops in the entire atmosphere (Xu et al., 1999; Chen and Li, 2000). Therefore, rainfall retrievals from MW instruments are capable of producing more accurate instantaneous rainfall estimates. However, the poor resolution of MW radiometers limits them to low-orbiting satellites, and hence poor time resolution of the resulting microwave data (one or two overpasses per day) (Kummerow et al., 1998).

1.2.1 Infrared (IR) and Visible (VIS) Rainfall Retrieval

Kidder and Vonder Haar (1995) proposed four categories of rainfall estimation using VIS and IR images: cloud indexing, life history, cloud model, and bi-spectral analysis. The basic premise in the cloud indexing technique, pioneered by Barrett (1970), lies on the fact that it is relatively easy to identify and classify cloud types in satellite images, and, consequently a rain rate can be assigned to each cloud type. Life cycle history techniques are based on the cloud's life cycle. For this purpose, a series of geostationary satellite images are required. Typically, the relationship between the time rate of change of the area of a cloud and the rain rate of the thunderstorm is examined (Stout et al., 1979). The method requires, in addition to images, radar or raingauge measurements. The cloud model technique, as the name suggests, involve the physics of the cloud by parameterizing convection, or relating cloud top temperatures to observed rain rates, or including cloud microphysics (drop formation, collection and coalescence, and evaporation). Typical cloud model techniques developed to infer precipitation from IR radiation include the GOES

Precipitation Index (GPI) (Arkin and Meisner, 1987), the Auto-Estimator proposed by Vicente et al. (1998) and adopted by Rozumalski (2000) and Boi et al. (2004), and the Precipitation Estimation from Remotely Sensed Information using Artificial Neural Network Cloud Classification System (PERSIANN-CCS) by Hong et al. (2004), and others.

The bi-spectral techniques combine a set of rules that are capable of predicting clouds that are most probable to produce rain. Clouds that are bright in the VIS image are more likely to produce rain than darker clouds as brightness is related to optical and, consequently, to cloud thickness. Clouds that are cold in the IR image are also more likely to produce rain than warm clouds, because cold clouds have higher tops than warm clouds (Barrett and Martin, 1981). There are exceptions in the aforementioned premises, though. Stratus clouds are bright, but neither produce as much nor as frequent rain as cumulonimbus clouds; Cirrus clouds, although they are cold, do not produce as much rain as other warm clouds (Houze, 1993). Examples of bi-spectral techniques are those of Garand (1989) where rainfall is assigned based upon four infrared temperature intervals and six cloud albedo intervals obtained from the visible channel, and Tsonis et al. (1996) where the optimum boundary is defined in the VIS/IR domain and is used to discriminate between rain and no-rain. However, the major drawback of bi-spectral techniques is the unavailability of VIS images during the night that prevents estimation of night-time rainfall (Tsintikidis et al., 1999).

1.2.2 Microwave (MW) Rainfall Retrieval

Radiative transfer process of rain is separated into two regimes: emission/absorption and scattering (Wilheit et al., 1991). Factors determining the type of attenuation are precipitation particle sizes, phase of particles (ice or liquid), and spectral bands (Kidd et al., 1998). Microwave brightness temperature (TB) observed in emission regime represents observation of liquid hydrometeors within the rain cloud, while that in scattering regime depends on details of ice layer of raining clouds. The low

emissivity of ocean (0.5 is a typical value) provides a good cold background for viewing particles above it with relatively higher emissivities, such as rain. The variations in microwave TB due to rainfall rate (RR) over oceans is such that microwave TB increases with an increase in RR due to rainfall emission effect (Chiu et al., 1990). This applies to low frequency microwave channels (i.e., 10.7, 19.4, 21.3, and 37 GHz).

In contrast, since land surfaces have emissivities in the range of 0.8-0.95, low frequency channels are not suitable for over land applications because high surface emissions effectively mask the precipitation emission (Kidd et al., 1998). Due to high sensitivity of 85.5GHz channels to volumetric scattering by precipitation, especially ice above the freezing level (Spencer et al., 1989), these channels are suitable for developing scattering-based methods on both ocean and land. In this case, the microwave TB decreases with increasing RR due to volumetric scattering by precipitation. The TB at 37GHz also decreases with increasing RR, both due to scattering by larger raindrops and emission at lower temperatures (Spencer et al., 1986). Therefore, microwave observations at 37GHz also have potential to retrieve rainfall on both land and oceans.

Due to existence of multiple hydrometeors that can be detected by multi-frequency passive MW measurements, MW rain retrieval algorithms suffer from various obstacles. The difficulty is more severe for overland retrievals because of the warm background that limit the use of lower-frequency observations (i.e., 10, 19, and 22 GHz). Some algorithms, referred to as physically based, are derived using radiative-transfer algorithms through cloud-model simulated precipitation fields (e.g., Evans et al., 1995; Kummerow et al., 1996). These algorithms were mainly investigated in over ocean retrievals. Studies dealing with physically based retrieval algorithms over land are few and have not indicated better performance relative to purely statistical algorithms (Druen and Heinemann, 1998), which are conceptually simpler and more practical for applications.

1.2.3 Application of Gauge and Remotely Sensed Rainfall in Basin Hydrology

Traditionally, gauge rainfall data (point measurements) have been used with hydrologic models. However, raingauge networks alone are usually too sparse to capture the spatial variability of rainfall over a river basin. The point measurements at any raingauge location are usually extended over its area of influence (such as using the Thiessen polygon technique) in hydrologic studies, resulting in poor representations of rainfall spatial distribution. This problem usually becomes more critical as the size of river basins increases.

Numerous studies have been conducted in the past two decades addressing the sensitivity of streamflow hydrographs to the spatial and temporal variations in precipitation. Many of these studies examined the effects of raingauge sampling errors on the outflow hydrograph. Wilson et al. (1979) showed that the spatial distribution of rainfall had a marked influence on the streamflow hydrograph from a small catchment. On the other hand, Beven and Hornberger (1982) stated that rainfall patterns have only a secondary effect on streamflow hydrographs. For a small watershed, Krajewski et al. (1991) found a higher sensitivity to the temporal resolution of precipitation than to the spatial resolution. Ogden and Julien (1994) and Shah et al. (1996) also investigated the effects of precipitation variability on hydrologic simulations.

It is interesting to note that most of these studies were based on synthetically generated precipitation and streamflow records due to a lack of appropriate observed data. Furthermore, many of the studies emphasizing the importance of the spatial variability of precipitation used models based on the Hortonian (i.e., infiltration-excess) runoff generation mechanism. Winchell et al. (1998) noted that there has been a bias towards the use of infiltration-excess runoff mechanism as

opposed to the saturation-excess type. Their work with both types of runoff generation mechanisms found that saturation-excess and infiltration-excess models responded differently to uncertainties in precipitation, with the latter being more sensitive than the former. Koren et al. (1999) came to a similar conclusion based on simulation results from different rainfall-runoff partitioning mechanisms.

Weather radars have long been recognized for their ability to provide estimates of precipitation at high spatial and temporal resolution even though such data still have problems. Stellman et al. (2001) evaluated the difference between the WSR-88D (Weather Surveillance Radar-1988 Doppler) radar and raingage rainfall data. They reported a 50% under-estimation of radar data as compared to raingages during the winter months (dominated by stratiform rainfall), while in the summer (dominated by convective rainfall) radar reported slightly more rainfall than raingages. Similarly, Jayakrishnan et al. (2004) showed that WSR-88D radar underestimated the five-year precipitation at vast majority of the 545 raingages used in their study. They concluded that, meaningful hydrologic predictions are not possible unless the uncertainty associated with the radar-derived precipitation can be quantified and corrected for.

There have been some contradictory conclusions on the impact of errors in the radar precipitation data. For instance, Numeç (1985) argued that errors in precipitation input to a rainfall-runoff model would result in significant errors in estimated runoff. Wyss et al. (1990) suggested that errors in runoff predictions due to errors in the radar-estimated rainfall input are of less significance than errors introduced in the rainfall-runoff conversion. Winchell et al. (1998) stated that there has not been a consensus on the effects of uncertainty in radar rainfall on hydrologic modeling, nor has the topic received adequate attention, e.g., most of the research on radar rainfall uncertainty has been mainly confined to comparisons with their raingauge counterparts without analyzing their influence on the predicted streamflow hydrographs.

Besides the aforementioned problems with radar data, the lack of weather radars in most parts of the world has pushed the scientific community to explore the use of satellite data to estimate surface rainfall. Hardy et al. (1989) used daily satellite-derived rainfall as input to a conceptual rainfall-runoff model for daily flow prediction in two sub-catchments of the Senegal River Basin. They reported that the flow predictions were at least as good when satellite-based rainfall estimates were used as input in place of conventional raingauge data. In a similar study for Tano River in West Africa, Papadakis et al. (1993) found that the model simulations of monthly runoff based on satellite and raingauge rainfall inputs compared equally well to observations. Tsintikidis et al. (1999) did a similar analysis for the Nile River Basin using a conceptual semi-distributed model with daily time step and $1^{\circ} \times 1^{\circ}$ discretization. In their case a minor improvement was found using the remotely sensed rainfall and they recommended its use as input in hydrologic models. Andersen et al. (2002) used rainfall estimates from METEOSAT satellite data as input to a distributed, physically based hydrologic model applied to three sub-catchments in the Senegal River Basin. They reported similar model performances when compared to the simulated hydrographs obtained from conventional raingauge input. In all these studies either a bi-spectral technique of Tsonis et al. (1996) or the cold cloud duration (CCD) technique of Arkin and Meisner (1987) was used to derive the satellite rainfall estimates. Tsintikidis et al. (1999) recommended the modification of the bi-spectral technique (i.e., into a univariate frequency analysis method where only IR is used) to enable it to resolve a night-time rainfall, which is not possible with VIS frequency. Andersen et al. (2002) pointed out that the cold cloud duration (CCD) technique relies heavily on statistical relations and it is questionable to which degree it captures the physical processes.

1.3 Statement of Problems

- (1) Due to a lack of distributed precipitation data, distributed and semi-distributed, physically based hydrologic models still use gauged rainfall data (point measurements) as their input function. This means an inadequate representation of rainfall spatial variability when the raingauge network is sparse, and a mismatch between model complexity and the primary forcing function (precipitation) for computing basin-scale water fluxes (Boyle et al., 2001).

- (2) It is possible to map detailed precipitation fields from radar rainfall measurements with refined spatial and temporal resolutions, which should contribute to the progress of basin-scale hydrologic modeling. However, there are many uncertainties associated with rainfall (R) estimated from radar echoes, such as beam blockage caused by topography; attenuation by atmospheric gases and raindrops; effects of ground clutter and anomalous propagation; uncertainties in reflectivity (Z) measurement caused by radar hardware calibration and stability issues; inappropriate Z-R relationships; data processing problems (e.g., averaging of overlapping radar coverage); and radar range effects (Pereira et al., 1998). For example, Stellman et al. (2001) reported that radar Mean Areal Precipitation (MAP) underestimated the raingauge MAP by about 50% during winter dominated by stratiform storms. A key question is how to correct the underestimation of rainfall depth by radar rainfall data but at the same time maintain its detailed representation of the space-time variations of rainfall fields?

- (3) Currently, even the best surface rainfall observing systems (i.e., gauge and radar) fail to capture the true spatial distribution of precipitation systems (Rozumalski, 2000). Raingauge observations are limited by spatial coverage problems (Fulton et al., 1998). In addition, the accuracy and reliability of these gauges is also an issue. Although radar estimates are superior to gauge data in

areal coverage and resolution, they are limited by the assumptions of the standard reflectivity to rainfall rate, a Z-R power-law relationship (e.g., Battan 1973; Doviak and Zrníc 1984). In addition, both methods are severely limited over mountainous terrain and large bodies of water (e.g., lakes) where coverage is poor or nonexistent. Also, weather radars are more restricted to locations near major cities, except for the Weather Surveillance Radar -1988 Doppler (WSR-88D) network of USA. On the other hand, the growth of space borne satellite data has been tremendous and will continue to grow in the foreseeable future, especially with NASA of USA launching a series of Earth Observation Satellites (EOS) such as EOS AM-1 and EOS PM-1. These satellites carry infrared and microwave sounders to measure precipitation volumes, cloud thickness, and cloud water content, among others, at global or near global coverage. Apparently we can take advantage of such satellite data for rainfall estimation and hydrologic modeling.

1.4 Research Objectives

The general goal of this research is to contribute to the progress of basin hydrologic modeling by improving the primary input function, i.e., the precipitation field. So, this study has three objectives:

- (1) Develop an Infrared-Microwave Rainfall Algorithm (IMRA) for estimating rainfall at high spatial and temporal scales using satellite data. The algorithm should require less input information, be less dependent on rain gauge data, utilize infrared (IR) brightness temperatures (TBs) as the main satellite information input, and use cloud physical processes (e.g., cloud-top structure) for discriminating rain/no-rain pixels. The IMRA should allow for the adjustment of the derived IR-rainfall estimates using microwave (MW) TBs information and spatial filtering/smoothing techniques. IMRA rainfall estimates are compared with gauge and radar data through hydrologic simulation using the Sacramento Soil Moisture Accounting (SAC-SMA) model.

- (2) Develop a data merging scheme that is wavelet based to combine radar rainfall with raingauge data to take advantage of both the capability of radar to map the spatial variability of precipitation and accurate rainfall depth measurements offered by raingauges. If the attributes of both types of rainfall data can be preserved in the merged radar-gauge rainfall product, it will contribute to the progress of basin hydrologic modeling. The use of wavelet based interpolation scheme to merge these two types of data has never been done before.
- (3) Assess the effect of radar rainfall uncertainty, the spatial variability of rainfall, and that of hydrologic model resolution on streamflow simulation using a semi-distributed, physically based hydrologic model.

1.5 Study Site Description

The research on satellite rainfall estimation was carried out in Peace River Basin, while that on radar rainfall uncertainty and the merging with the corresponding gauge rainfall data using wavelet analysis was done in Blue River Basin. The two study sites are briefly described below.

(a) Peace River Basin (PRB)

The PRB is located in Southwest Floarida (USA) and receives surface runoff from an area of approximately 6086 km². Its headwaters are in central Polk County, and the river flows in a southerly direction for about 120 km to the Charlotte Harbor. Land-surface altitudes range from about 60 m above sea level near the headwaters to sea level at the mouth. Land use and land cover in the study area is dominated by agricultural land and rangeland, comprising about 70 percent of the total land area of PRB. Annual rainfall averages at about 1320 mm and temperature ranges from an average of about 27 °C during the summer to about 16 °C in December and January.

(b) Blue River Basin (BRB)

The BRB is located in South Central Oklahoma (USA) and has a total catchment area of 1233 km². Its elevation ranges from 153 to 350m above mean sea level. The basin has a relatively flat terrain, and the major soil groups are clay and loam mixed with sand or silt. Woody Savannah is the dominant vegetation cover occupying almost 80% of the basin. The average annual precipitation ranges from about 400mm in the extreme western panhandle to 1420mm in the southeastern corner of the State (Frederick et al., 1977). The January temperature ranges from a daytime high of 20⁰C to a nighttime low well below zero. The primary source of moisture is from the Gulf of Mexico. The Pacific Ocean off the coast of Mexico is a source of moisture under certain airflow patterns.

1.6 Organization of Thesis

This thesis consists of five chapters. Chapter 1 provides an overview of the general background on techniques used in rainfall estimation, particularly remotely sensed rainfall, and the influence of its spatial and temporal distribution in basin hydrologic modeling. Chapter 2 describes in detail the development and validation of an Infrared Microwave Rainfall Algorithm (IMRA) for estimation of rainfall suitable for small-scale hydrologic modeling using satellite data. The assumptions, cloud physical processes, and the data used in evaluating the IMRA in Peace River Basin are also discussed. In Chapter 3, the development and validation of a wavelet based data merging scheme for combining radar and gauge rainfall data is described in detail, while in Chapter 4, a detailed analysis of the effect of radar rainfall uncertainty, the spatial variability of rainfall, and model resolution on streamflow prediction using a semi-distributed physically based model is carried out. The assessment on advantages of radar data over gauge rainfall data in basin hydrologic modeling is also performed. Finally, summary, concluding remarks, and recommendations for future work are presented in Chapter 5.

References

- Andersen, J., Dybkjaer, G., Jensen, K. H., Refsgaard, J. C., and Rasmussen, K. (2002), Use of remotely sensed precipitation and leaf area index in a distributed hydrological model. *J. of Hydrology*, 264, 34-50.
- Arkin, P. A., and Meisner, B. (1987), The relationship between large-scale convective rainfall and cold cloud over the Western Hemisphere during 1982-1984. *Monthly Weather Review*, 115, 51-74.
- Barrett, E. C. (1970), The estimation of monthly rainfall from satellite data. *Monthly Weather Review*, 101, 215-222.
- Barrett, E. C., Martin, D. W. (1981), *The Use of Satellite Data in Rainfall Monitoring*. Academic Press, New York, 340 pp.
- Battan, L. (1973), *Radar Observation of the Atmosphere*. University of Chicago Press, 324 pp.
- Beven, K. J., and Hornberger, G. M. (1982), Assessing the effect of spatial pattern of precipitation in modeling stream flow hydrographs. *Water Resources Bulletin*, 823-829.
- Boi, P., Marrocu, M., and Giachetti, A. (2004), Rainfall estimation from infrared data using an improved version of the Auto-Estimator Technique. *Int. J. Remote Sensing*, 25 (21), 4657-4673.
- Boyle, D. P., Gupta, H. V., and Sorooshian, S. (2001), Toward improved stream flow forecast: value of semi-distributed modeling. *Water Resources Research*, 37(11), 2749-2759.
- Chen, W. -J., and Li, C. -C. (2000), Oceanic rain rate retrievals using TRMM Microwave Imager multi-channel brightness temperatures during the 1998 SCSMEX. *Terrestrial, Atmospheric and Oceanic Sciences*, 11, 765-788.
- Chen, W. -J., and Li, C. -C. (2002), Rain retrievals using Tropical Rainfall Measuring Mission and Geostationary Meteorological Satellite 5 data obtained during the SCSMEX. *Int. J. Remote Sensing*, 23(12), 2425-2448.

- Chiu, L. S., North, G. R., Short, D. A., and McConnel, A. (1990), Rain estimation from satellites: Effect of finite field of view. *J. of Geophys. Res.*, 95, 322-327.
- Clark, D. (1983), *The GOES User's Guide*. National Environmental Satellite and Data Information Service, Washington, DC, 163 pp.
- Crum, T. D., and Alberty, R. L. (1993), The WSR-88D and the WSR-88D operational support facility. *Bull. Amer. Meteor. Soc.*, 74, 1669-1687.
- Doviak, R., and Zrnica, D. (1984), *Doppler Radar and Weather Observations*. Academic Press, 458 pp.
- Druen, B., and Heinemann, G. (1998), Rain rate estimation from a synergetic use of SSM/I, AVHRR and meso-scale numerical model data. *Meteor. Atmos. Phys.*, 66, 65-85.
- Evans, K. F., Turk, J., Wong, T. M., and Stephens, G. L. (1995), A Bayesian approach to microwave precipitation profile retrieval. *J. Appl. Meteor.*, 34, 260-279.
- Frederick, R. H., Miller, J. F, and Tracey, R. J. (1977), *Five to Sixty Minute Precipitation Frequency for the Eastern and Central U.S.*, NOAA Technical Memorandum NWS Hydro-35, Silver Springs, MD.
- Fulton, R. A., Breidenbach, J. P., Seo, D. -J., Miller, D. A., and O'Bannon, T. (1998), The WSR-88D rainfall algorithm. *Weather & Forecasting*, 13, 377-395.
- Garand, L. (1989), Two automated methods to derive probability of precipitation fields over oceanic areas from satellite imagery. *J. Appl. Meteor.*, 28, 913-924.
- Groisman, P. Y., and Legates, D. R. (1994), The accuracy of United States precipitation data. *Bull. Amer. Meteor. Soc.*, 75, 215-227.
- Hardy, S., Dugdale, G., Milford, J. R., and Sutcliffe, J. V. (1989), The use of satellite derived rainfall estimates as inputs to flow prediction in the River Senegal. New directions for surface water modeling. *Proceedings of the Baltimore Symp.*, number 181 in IAHS publications.
- Hong, Y., Hsu, K., Sorooshian, S., and Gao, X. (2004), Precipitation Estimation from Remotely Sensed Imagery using an Artificial Neural Network Cloud Classification System. *J. of Applied Meteo.*, 43, 1834-1852.

- Houze, R.A. (1993), *Cloud dynamics*. Academic Press, 269 pp.
- Jayakrishnan, R., Srinivasan, R., and Arnold, J. G. (2004), Comparison of raingage and WSR-88D stage III precipitation data over the Texas-Gulf basin. *J. of Hydrology*, 292, 135-152.
- Kidd, C., Kniveton, D., and Barrett, E. C. (1998), The advantages and disadvantages of statistically derived-empirically calibrated passive microwave algorithms for rainfall estimation. *J. of the Atmospheric Sciences*, 55, 1576-1582.
- Kidder, S. Q., and Vonder Haar, T. H. (1995), *Satellite Meteorology*. Academic Press, San Diego, CA, 466 pp.
- Koren, V. I., Finnerty, B. D., Schaake, J. C., Smith, M. B., Seo, D.-J., Duan, Q. Y. (1999), Scale dependencies of hydrology models to spatial variability of precipitation. *J. of Hydrology*, 217, 285-302.
- Krajewski, W. F., Lakshmi, V., Georgakakos, K. P., and Jain, S. C. (1991), A monte-carlo study of rainfall sampling effect on a distributed catchment model. *Water Res. Research*, Vol. 27, No. 1, 119-128.
- Kummerow, C., Olson, W. S., and Giglio, L. (1996), A simplified scheme for obtaining precipitation and vertical hydrometeor profiles from passive microwave. *IEEE Trans. Geosci. Remote Sens.*, 34, 1213-1232.
- Kummerow, C., Barnes, W., Kozu, T., Shiue, J., and Simpson, J. (1998), The tropical rainfall measuring mission (TRMM) sensor package. *J. of Atmospheric and Oceanic Technology*, 15, 809-817.
- Legates, D. R., and DeLiberty, T. L. (1993), Measurement biases in the United States rain gauge network. *Water Resources Bulletin*, 29, 855-861.
- Numec, J. (1985), Water resources systems and climate change, in *Facets of Hydrology*, Vol. II, Edited by J.C. Rodda, pp. 131-152, John Wiley, New York.
- Ogden, F. L., Julien, P. Y. (1994), Runoff model sensitivity to radar rainfall resolution. *J. of Hydrology*, 158, 1-18.
- Papadakis, I., Napiorkowski, J., and Schultz, G. A. (1993), Monthly runoff generation by nonlinear model using multispectral and multitemporal satellite imagery. *Adv. Space Res.*, 13, 5-12.

- Pereira Fo, A. J., Crawford, K. C., and Hartzell, C. L. (1998), Improving WSR-88D Hourly Rainfall Estimates, *Weather and Forecasting*, 13, 1016-1028.
- Rozumalski, R. A., (2000), A quantitative assessment of NESDIS Auto-Estimator. *Weather and Forecasting*, 15, 397-415.
- Shah, S. M. S., O'Connell, P. E., and Hosking, J. R. M. (1996), Modeling the effects of spatial variability in rainfall on catchment response. 2. Experiments with distributed and lumped models. *J. of Hydrology*, 175, 89-111.
- Simpson, J., Kummerow, C., Tao, W. K., and Adler, R. F. (1996), On the tropical rainfall measuring mission (TRMM). *Meteo. and Atmos. Physics*, 60, 19-36.
- Spencer, R. W. (1986), A satellite passive 37-GHz scattering-based method for measuring oceanic rain rates. *J. of Climate and Applied Meteo.*, 25, 754-780.
- Spencer, R. W., Goodman, H. M., and Hood, R. E. (1989), Precipitation retrieval over land and ocean with the SSM/I: identification and characteristics of the scattering signal. *J. of Atmospheric and Oceanic Technology*, 6, 254-273.
- Stellman, K. M., Fuelberg, H. E., Garza, R., and Mullusky, M. (2001), An examination of Radar Rain Gauge-Derived Mean Aerial Precipitation over Georgia Watersheds. *Weather and Forecasting*, 16, 133-144.
- Stout, J. E., Martin, D. W., and Sikdar, D. N. (1979), Estimating GATE rainfall with Geosynchronous satellite images. *Mon. Wea. Rev.*, 107, 585-598.
- Tsintikidis, D., Georgakakos, K. P., Artan, G. A., and Tsonis, A. A. (1999), A feasibility study on mean areal rainfall estimation and hydrological response in the Blue Nile region using METEOSAT images. *J. of Hydrology*, 221, 97-116.
- Tsonis, A. A., Triantafyllou, G. N., and Georgakakos, K. P. (1996), Hydrological applications of satellite data 1. Rainfall estimation. *J. Geophys. Res.*, 101, 26517-26525.
- Vicente, G. A., Scofield, R. A., and Menzel, W. P. (1998), The operational GOES infrared rainfall estimation technique. *Bull. Amer. Meteor. Soc.*, 79 (9), 1883-1898.

- Wilheit, T. T., and Chang, A. T. C., and Chiu, L. S. (1991), Retrieval of monthly rainfall indices from microwave radiometric measurements using probability distribution functions. *J. of Atmospheric and Oceanic Technology*, 8, 118-136.
- Wilson, C. B., Valdes, J. B., and Rodriguez-Iturbe, I. (1979), On the Influence of the spatial distribution of rainfall on storm runoff. *Water Resources Research*, Vol 15(2), 321-328.
- Winchell, M., Gupta, H. V., and Sorooshian, S. (1998), On the simulation of infiltration- and saturation- excess runoff using radar-based rainfall estimates: Effects of algorithm uncertainty and pixel aggregation. *Water Resources Research*, Vol 34, No. 10, 2655-2670.
- Wyss, J., Williams, E. R., and Brass, R. L. (1990), Hydrologic modeling of New England river basins using radar rainfall data. *J. Geophys. Res.*, 95(D3), 2143-2152.
- Xu, L., Gao, X., Sorooshian, S., Arkin, P. A., and Imam, B. (1999), A microwave infrared threshold technique to improve GOES Precipitation Index. *J. of Applied Meteorology*, 38, 569-579.

Chapter 2

Estimation of Rainfall from Satellite Data for Basin Scale Hydrologic Modeling

2.1 Introduction

Reliable estimate of mean areal rainfall as input to hydrologic catchments is a crucial step for accurate prediction of catchment outflows. The lack of adequate ground-based rainfall measurements (i.e., rain gauges) has inspired a search for remotely sensed precipitation data from space platforms (Tsintikidis et al., 1999) and radar data. The interest in space platforms is predicated on the assumption that this information can potentially provide a cost-effective data source over temporal and spatial scales not possible from any other in situ or remote systems (Rozumalski, 2000). These precipitation estimates would be a valuable contribution to many hydrological applications where high-resolution data are not routinely available. A combination of dense networks of rain gauges and ground-based radar has been used to provide high-resolution rainfall information for limited areas (e.g., Klazura and Imy, 1993). However, for most parts of the earth the in-situ infrastructure necessary for this form of precipitation monitoring network is not available because of prohibitive costs and poor accessibility in remote sites and mountainous areas.

Satellite-based techniques for rainfall measurement have been actively explored to offer an alternative to ground-based data. Passive microwave (MW) data are able to provide accurate estimates of instantaneous rain rates, but the poor temporal sampling of low earth-orbiting satellites (once or twice per day) makes these data most suitable for estimation of accumulated rainfall over longer periods of perhaps a month or more (Adler et al., 1993). Satellite infrared (IR) data benefit from the high temporal sampling (30-minutes or 1-hour) of geostationary satellites such as Geostationary Operational Environmental Satellite (GOES), but IR radiances from cloud tops have only a weak, indirect relationship with surface rainfall. Therefore, many simple IR algorithms rely on the effects of scale averaging to improve accuracy, for instance the GOES Precipitation Index (GPI) which averages rainfall estimates in $2.5^\circ \times 2.5^\circ$ grid boxes (Arkin and Meisner, 1987). Compared to polar-orbiting satellite data, geostationary satellite data suffer from less sampling errors at all temporal scales because the latter can acquire an image every half-hour/hour as against the 1 or 2 images per day from polar-orbiting systems. As a result, many studies have focused their estimation of basin scale rainfall at short timescales (from a few hours to perhaps a few days) using data from geostationary satellites such as GOES (e.g., Vicente et al., 1998; Todd et al., 1999; and Hong et al., 2004).

The auto-estimator (AE), which uses GOES infrared (IR) data to compute real-time precipitation amounts (especially that of convective storms) at hourly to daily time steps and 12 km spatial scale has been developed and tested (Vicente et al., 1998). Comparing the results with gauge-adjusted radar precipitation data showed that AE produced useful 1 - 6 hour precipitation for flash flood monitoring but exaggerated the area of precipitation causing an overestimation of daily rainfall totals. In addition, AE uses model-generated relative humidity and precipitable water to scale the rainfall amount accordingly. Todd et al. (1999) introduced a continuously calibrated IR satellite rainfall estimation technique (CCB4) for computing rainfall rate at daily and 5 km spatial scale. Compared to GPI, CCB4 showed improved

skill in identifying rainy days and estimating daily rainfall amounts, but its major drawback is that it heavily relies on the availability of near-real-time rain gauge data. Similarly, a method to improve the GPI technique, termed the Universally Adjusted GPI (UAGPI) was proposed, where satellite IR and microwave data were combined and evaluated on monthly time step and a spatial scale of $2.5^{\circ} \times 2.5^{\circ}$ (Xu et al., 1999). The UAGPI results were superior to that of GPI, but it was tested at larger scales that are of little interest to basin hydrologic modeling.

From a slightly different perspective, an algorithm termed Precipitation Estimation from Remotely Sensed Information using Artificial Neural Network Cloud Classification System (PERSIANN-CCS) was developed (Hong et al., 2004). This algorithm uses IR satellite imagery to extract rainfall distributions at 4 km x 4 km resolution and every 30 minutes from local and regional cloud features. The PERSIANN-CCS rainfall estimates were evaluated using both radar and gauge rainfall measurements at hourly to daily, and spatially at 4 km, 12 km, and 25 km. However, the correlation with the observed data are low, partly because of the problems in separating cloud image into distinct cloud systems, or separable cloud-patch classes and how are these classes associated with the rainfall distribution.

This research presents the development and validation of a new IR/MW satellite technique for estimating rainfall rate (R) at high spatial and temporal scales, termed Infrared-Microwave Rainfall Algorithm (IMRA) (Section 2.4). It is designed to require less input parameters, less dependent on rain gauge data, and utilize both satellite IR and microwave brightness temperatures (TB) through locally derived nonlinear R-TB relationships.

2.2 Peace River Basin (PRB)

The Peace River Basin (PRB), located in Southwest Florida, USA was selected as the study site because it is neither regulated nor channelized, which is not the case

for most rivers in this area. Also, there is ready access to satellite observations and high spatial and temporal resolution raingauge data suitable for developing satellite rainfall retrieval algorithms. The Peace River receives surface runoff from an area of approximately 6086 km². Its headwaters are in central Polk County, and the river flows in a southerly direction for about 120 km to the Charlotte Harbor. Approximately 670 km² (11 percent) of the PRB drains into the river downstream from the gauging station at Arcadia (station 1, Figure 2.1) and the tributary gauges on Joshua Creek, Horse Creek, and Shell Creek (see Figure 2.1). Land-surface altitudes range from about 60 m above sea level near the headwaters to sea level at the mouth. Land use in the study area is dominated by agricultural land and rangeland, comprising about 70 % of the total land area of the PRB. Annual rainfall averages about 1320 mm, of which more than half occurs from June through September during local convective thunderstorms. The rainfall during fall, winter, and spring is usually the result of large frontal systems and tends to be more broadly distributed than rain associated with local thunderstorms. October through May is dry, with November usually being the driest month. Temperature ranges from an average of about 27 °C during the summer to about 16 °C in December and January.

2.3 Data Description

2.3.1 Infrared (IR) and Passive Microwave (MW) Data

The Infrared (IR) cloud-top brightness temperatures were obtained from two satellite sources: (a) the Visible/Infra-Red Scanner (VIRS) aboard the Tropical Rainfall Measuring Mission (TRMM) satellite provided the channel 4 (at 10.8 μm) brightness temperatures at 2.4 km and 12-hour or 24-hour resolutions, and (b) the Geostationary Operational Environmental Satellite (GOES) provided the channel 4 (at 10.7 μm) brightness temperatures at a spatial and temporal resolution of 4 km and 1-hour respectively. The level-1B01 VIRS IR data was deemed suitable for developing satellite rainfall retrieval algorithms due to their high spatial resolution, while the GOES IR data were used for the actual IR-derived rainfall estimation due

to their high temporal resolution (hourly). An effective 35 x 20 pixels window at 4 km resolution covering PRB and its vicinity was used, which is 37 x 22 pixels window with border pixels included, ranging from latitudes 26.84 N to 28.32 N and longitudes 81.64 W to 82.34 W.

The TRMM Microwave Imager (TMI) provided the passive microwave (MW) brightness temperatures (TBs). The level-1B11 microwave data used here are from microwave channels 8 and 9 at 85.5GHz, labeled as TB₈ and TB₉ to represent the level-1B11 TBs at 85.5 GHz vertical (V) and 85.5 GHz Horizontal (H) polarizations respectively. The time resolution for these data is once or twice per day, while the spatial resolution is about 5 km.

2.3.2 Rainfall and Streamflow Data

On the east side of the PRB, a dense rain gauge network has been installed around Melbourne-Florida ground-validation (GV) site in a field campaign, which is an integral component of the TRMM satellite extensive validation program (Figure 2.2). On this GV site, the rain gauge data are at a high spatial resolution and a time resolution of 1-minute recorded in a continuous basis for days and times when there was rainfall. These data are ideal for deriving infrared/microwave satellite rainfall retrieval algorithms. Another data used in this study are gauge-adjusted stage IV radar precipitation, developed by the National Centers for Environmental Prediction (NCEP), found at <http://wwwt.emc.ncep.noaa.gov/mmb/ylin/pcpanl/stage4/>. These data are at 1 hour and 4 km resolutions. Within the PRB there are five National Weather Service Meteorological sites (Figure 2.1), which provide continuous rainfall time series (from 1931 to Date) at daily time step. In the PRB, historical daily streamflow data have been collected as part of the National Water Information System (NWIS), and have been reviewed and approved for public release. Both the Peace River (at Arcadia) and its tributaries (Figure 2.1) have streamflow records starting from 1931 to present. These data sets have been quality controlled by U.S. Geological Survey.

2.4 Infrared-Microwave Rainfall Algorithm (IMRA)

The development of IMRA is based on the following assumptions: (a) raining clouds are associated with growing clouds exhibiting overshooting tops (Hong et al., 2004); (b) raining clouds with cold tops in the IR imagery produce more rainfall than those with warmer tops (Arkin and Meisner, 1987); and (c) passive microwave (MW) TBs can provide accurate estimates of instantaneous rain rates and this information can be used to improve rainfall estimates from IR data at high temporal frequency (Adler et al., 1993; Xu et al., 1999; Chen and Li, 2002; Marzano et al., 2004). Comparison of GOES IR cloud-top temperature imagery against collocated gauge-adjusted radar images have demonstrated that convective thunderstorms are characterized by rapid spatial and temporal changes in the structure of the cloud-top surface and very low cloud-top temperatures (Vicente et al., 1998). The correct rainfall estimates from satellite IR imagery depends not only on the accurate estimates of the instantaneous rainfall rates for every pixel, but also the effective screening of the non-raining pixels because rainfall tends to be a discontinuous variable. Since only the cloud tops can be observed, implying a weak and indirect relationship with surface rainfall, it becomes difficult to achieve that goal using one IR channel alone. However, analyzing the IR cloud-top temperature distribution on a pixel-by-pixel basis helps to locate precipitating areas (Hong et al., 2004).

For a given time step (e.g., hourly), IMRA provides estimates of rainfall rate at pixel scale through a three stage process. In stage 1, rainfall rates are computed from a nonlinear, power-law regression relationship between gauge measured rainfall data and IR cloud-top temperature ($R-TB_{IR}$). Gagin et al. (1985) suggested the use of a power-law relation between IR cloud-top temperature and rainfall rates, and the idea has been used in recent studies (e.g., Vicente et al., 1998; Hong et al., 2004). Stage 2 includes two techniques used to separate raining/non-raining pixels. First, based on the $R-TB_{IR}$ relationship, IR threshold values for minimum detectable

rainfall rates are determined for use as global (constant) rain/no-rain screening tools. Past studies have employed a minimum detectable rainfall rate of 0.25 mm/hr (Xu et al., 1999) and 1 mm/hr (Adler et al., 1993). Second, to account for the local-scale rainfall/cloud characteristics, analysis of the cloud-top temperature on a single IR image is employed to determine a cloud-top temperature gradient at pixel scale. Fully developed convective clouds have distinguishable overshooting tops, tight temperature gradients, and higher local pixel temperature variations while stratiform clouds show more gradual temperature gradients and lower temperature variations (Hong et al., 2004). Hence, spatial analysis of cloud systems texture using cloud-top temperature gradients can identify raining cloud areas (e.g., Adler and Negri, 1988; Vicente et al., 1998). In stage 3, IMRA uses MW-derived rainfall estimates to adjust the IR-derived rainfall estimates (see section 2.4.3). The MW-rainfall estimates are obtained through a nonlinear, power-law regression relationship between gauge rainfall measurements and MW TB (R-TB). Also, IMRA has a spatial filtering/smoothing component, which can be used to adjust the IR-derived rainfall estimates.

2.4.1 Rain Rate and IR Brightness Temperature (R-TB_{IR}) Relationship

The IMRA precipitation rates are computed using a power-law fit between coincident gauge measured rainfall and satellite measurements of IR TB at cloud top. The IR-gauge data were considered coincident if they were within time difference of less than 10 minutes and IR data points are within a 2 km x 2 km pixel surrounding a particular rain gauge. In order to have enough coincident IR-gauge data, the IR cloud-top TB from the Visible/Infrared Scanner (VIRS) aboard the TRMM satellite were used instead of those from GOES platform because the former have a resolution of 2.4 km while the latter are at 4.0 km resolution. The original set of 1487 pairs of gauge rainfall estimates and IR cloud-top temperatures were collected during the month of June to September 2000, which is a period usually

dominated by convective rainfall systems for this study site at Florida (USA). The 1487 pairs of data were manually screened until only 273 pairs were retained such that for the data retained, we can correctly match higher gauged rainfall rate with colder IR cloud top temperature within a 2 km x 2 km grid area surrounding each rain gauge. This screening is intended to reduce errors associated with geolocation due to errors in geo-referencing of satellite IR data to ground locations, and non-uniformity of rainfall rate under the raining cloud where colder cloud-top temperatures might not be associated with high rainfall rate. This dataset was used to derive the power-law regression curve expressed as

$$R = 1.522E + 12 \exp\left(\frac{-1}{207.67} [TB_{IR} + 60.96]^{1.5235}\right) - 0.338 \quad (2.1)$$

where R is the rainfall rate in mm per hour and TB_{IR} is the IR cloud-top TB in Kelvin. The above regression fit had a coefficient of determination (R^2) of 0.98 and a modeling efficiency (E_f) of 0.95 between observed and estimated rainfall rates (Figure 2.3). An independent dataset consisting of 150 pairs of gauge rainfall rate and IR cloud-top temperature collected during the month of June to September 2001 and screened in the same manner as above was used to validate the derived power-law regression. In this validation case between observed and estimated rainfall rates the R^2 was 0.93 and an E_f of 0.89, which is very encouraging.

2.4.2 Rain/No-Rain Discrimination

In general, approximately 90% of the rain from clouds is produced by only 50% of the raining cloud area (Vicente et al., 1998). This implies that a major challenge in estimating rainfall using IR measurements is to distinguish raining from non-raining clouds. A cloud system is more active and produces highest rainfall when the cloud-tops are colder, overshooting, and expanding (Griffith et al., 1978; Hong et al., 2004). To remove non-raining clouds, an empirical procedure termed as SLOPE is developed in this study. The proposed technique is compared by the HESSIAN method proposed by Vicente et al. (1998).

2.4.2.1 Slope Technique (ST)

In a 3x3 pixels moving window, a slope (S) parameter of the center pixel is computed based on the cloud-top temperature (T) as

$$S = T_{(i,j)} - T_{mean} \quad (2.2)$$

where $T_{(i,j)}$ is the IR TB of the center pixel and T_{mean} is the average temperature of the 8 pixels surrounding the current pixel calculated as

$$T_{mean} = \{T_{(i-1,j+1)} + T_{(i-1,j)} + T_{(i-1,j-1)} + T_{(i,j+1)} + T_{(i,j-1)} + T_{(i+1,j+1)} + T_{(i+1,j)} + T_{(i+1,j-1)}\} / 8.0 \quad (2.3)$$

An empirically determined cut-off cloud-top temperature gradient of 1^0 Kelvin is suggested for screening rain/no-rain pixels. Thus, all pixels having S less or equal to -1^0 Kelvin (i.e., $S \leq -1$) are classified as raining cloud pixels. This screening of non-raining clouds is used for all clouds having cloud-top temperatures lower than the IR threshold temperature of 243^0 K discussed in Section 2.4.2.3. In the slope technique, the temperature of the analysis (center) pixel does not necessarily need to be an absolute minimum as compared to the surrounding pixels.

2.4.2.2 Hessian Technique (HT)

Vicente et al. (1998) suggested a technique for identifying rain/no-rain pixels that involves analysis of the first and second derivatives of cloud-top temperature in a given IR image, which is referred herein as the Hessian technique (HT). It is also implemented in a moving window of 3x3 pixels centered on the pixel $P_o = (x_o, y_o)$. If the cloud-top surface is defined by $T = T(x, y)$, with T being the cloud-top temperature as a function of x and y coordinates, the second derivatives of T on the pixel P_o are given as

$$T''_{x|x=x_o} = \partial^2 T(x, y) / \partial x^2 ; T''_{y|y=y_o} = \partial^2 T(x, y) / \partial y^2 ;$$

$$T''_{x|x=x_o, y|y=y_o} = \partial^2 T(x, y) / \partial x \partial y \quad (2.4)$$

and the Hessian (H) is given as

$$H = T''_{x|x=x_0} T''_{y|y=y_0} - (T''_{x|x=x_0, y|y=y_0})^2 \quad (2.5)$$

The pixel P_0 is characterized as follows: if $H > 0$ and $T''_{x|x=x_0} < 0 \rightarrow$ maximum; if $H > 0$ and $T''_{x|x=x_0} > 0 \rightarrow$ minimum; if $H < 0 \rightarrow$ no maximum, no minimum; and if $H = 0 \rightarrow$ not known.

The plan is to identify pixels that represent local temperature minimum and assume these pixels indicate active clouds with rainfall underneath them. In a closed 3x3 pixels window, the HT involves searching if the IR cloud-top temperature of the analysis pixel (P_0) is the absolute minimum as compared to the surrounding pixels (Weir et al., 2006) in which case it is considered to be a raining pixel.

2.4.2.3 IR Threshold Temperature

A minimum IR threshold TB above that no rain could occur was established from the $R-TB_{IR}$ power-law relationship (Eq. 2.1) based on a selected minimum detectable rainfall rate (where values from 0.0 mm/hr to 1 mm/hr were tested). From Eq. 2.1, a rainfall rate of 0.0mm/hr is equivalent to 243°K and an IR cloud-top temperature of 239°K produces 0.25mm/hr. The IR threshold of 243°K was selected because it allows estimation of zero rainfall. Therefore the results presented here are based on the minimum detectable rainfall rate of 0.0mm/hr where the corresponding IR threshold temperature of 243°K was employed as a global rain/no-rain discriminator. In effect, the above rain/no-rain discrimination techniques help to estimate the spatial variability of rainfall at pixel scale.

2.4.3 Microwave (MW) Adjustment of IR-Rainfall Rate

Besides condensation and growth of particle sizes, rainfall generation involves variety of physical processes that varies with season, location, and storm types. This poses a limitation in accuracy when rainfall is retrieved from a single relation between IR cloud-top temperature and surface rainfall rate (Hong et al., 2004). On

the other hand, the use of a single-function seems to be more appealing and practical instead of deriving a different function/curve for each situation. For improving the single-function approach to estimate rainfall from satellite data, we can rely on the temporal adjustment of the $R-TB_{IR}$ estimates from other sources of rainfall observations such as surface radar/gauge measurements or low-orbiting satellite microwave rainfall estimates, or rely on spatial/temporal accumulations of rainfall to lower resolutions such as monthly time step and $2.5^\circ \times 2.5^\circ$ (e.g., Xu et al., 1999). Nevertheless, because of the lack of sufficient ground rainfall observations, our ability to employ surface radar/gauge measurements is usually limited for most parts of the earth. Fortunately, microwave observations from polar-orbiting satellites can be used instead, although their poor temporal resolution (one or two overpasses per day) provides only instantaneous snapshots of precipitation.

Rainfall rate estimated using the $R-TB_{IR}$ power-law curve derived in this study can be adjusted by satellite microwave rainfall estimates in every 5x5 pixel area treated independently and having its own mean rainfall adjustment factor. The MW adjustment factor is given by the ratio of the mean of MW and IR rainfall rates in every 5x5 pixel area, and then the MW factor is multiplied with the IR rainfall estimates at each individual pixel to adjust IR rainfall estimates. To avoid the adjustment factor being zero when MW rainfall rate is zero, or becoming too big when IR rainfall rate is too small, the range of MW adjustment factor was limited to 0.5 and 2 inclusive. Xu et al. (1999) employed a MW adjustment factor range of 0.2 to 2 inclusive, in estimating satellite rainfall using IR and microwave TB on monthly time step and a spatial resolution of $2.5^\circ \times 2.5^\circ$. A power-law regression curve between MW TB and gauge surface rainfall rate was derived as

$$R = -0.8290E - 04TB_8^{2.5915} + 0.6693TB_9^{0.9963} \quad (2.6)$$

where R is the rainfall rate in mm/hour, TB_8 and TB_9 are microwave TBs in Kelvin for channels 8 and 9 respectively. For calibration, 141 data pairs from the summer of 2000 were used and the R^2 obtained was 0.85, while the E_f was 0.72. Validation was done using 110 data pairs from the summer of 2001, and the resulting R^2 was

0.78 and E_f was 0.60. The performance of Eq. 2.6 is slightly poorer than that of Eq. 2.1 because, in this case the MW-gauge data were considered coincident if they were within a time difference of less than 10 minutes and within a 4 km x 4 km pixel surrounding a particular rain gauge instead of 2 km x 2 km because of the poorer resolution of MW data (i.e., 5.1 km as compared to 2.4 km for VIRS IR data) from TRMM Microwave Imager (TMI). Using MW TBs statistics for no-rainfall events, the rain threshold for TB_8 and TB_9 were determined to be 278.42°K and 263.78°K respectively, which are within the range suggested by Chen and Li (2000, 2002). This means that a pixel with a TB greater than its rain threshold is classified as no-rain scene, because the channels at 85.5 GHz (i.e., TB_8 and TB_9) detect rainfall by scattering mechanism and hence rain pixels are colder than no-rain pixels.

2.4.4 Spatial Smoothing/Filtering

Spatial smoothing of the estimated satellite rainfall rates were assessed because satellite infrared (IR) radiances from cloud tops have only a weak, indirect relationship with surface rainfall, and coupled with non-uniform rainfall rate under the raining cloud, colder cloud-top temperatures might not be associated with higher rainfall rate. The spatial filtering can remove spike or impulsive noise in the satellite rainfall estimates and hence improve the satellite-to-radar rainfall comparison. Three spatial filtering techniques using a sliding-window described below were tested. Figure 2.4 illustrates this sliding-window approach and is similar to the one used in Section 2.4.2 above. Consider the 5×7 data array on the left-hand side (Figure 2.4). A 3×3 kernel is convoluted with the 3×3 data array beneath it, and the result of the convolution is placed at the central pixel (checkered box) location in the new filtered image (shaded on the right-hand-side array). This operation is repeated by sliding the window, first from left to right and then from top to bottom, to create the new filtered image. The border pixels are kept unaltered. An effective 35 x 20 pixels window at 4 km resolution covering PRB and its vicinity was used, where with border pixels included the window was 37 x 22 pixels. The sliding-

window technique can be written as $\tilde{F}A = B$, where \tilde{F} signifies the filtering operation on the original array A , giving the new filtered array B .

2.4.4.1 Quad-Smoothing (QS)

In this method the 3×3 window is again split into 4 quads (see illustration in Figure 2.5). The arithmetic average of each quad is performed and is denoted by \bar{Q}_i for the i^{th} quad. The average of the central pixel value (number 5) with the four quad averages is substituted as the smoothed estimate of pixel 5 (Datta et al., 2003). This method is referred to as QS in the rest of the chapter, and is equivalent to using a weighted average with the 3×3 kernel.

2.4.4.2 Median Filtering (MF)

Smoothing using median filtering (MF) is also tried. In MF, accumulations in the 3×3 window are first sorted, and then the median of those nine observations is substituted for the central pixel value. Suppose we have a 3×3 data array, such as

$$\begin{bmatrix} 7 & 18 & 2 \\ 9 & 3 & 25 \\ 17 & 10 & 15 \end{bmatrix}$$

If we sort these nine values, we will have the set $\{2, 3, 7, 9, 10, 15, 17, 18, 25\}$. The median value of this array is 10, which is substituted for the central pixel. This is a nonlinear filtering technique (Jain, 1989) used mainly to remove any noisy pixel that shows a spike in the scene.

2.4.4.3 Trimming Filter (TF)

In this method, the two lowest and two highest values from the sorted set of nine observations are removed first, and then the average of the five central values is substituted for the central pixel value. This is a hybrid filter known as an α -trimmed

mean filter (Efford, 2000). In the current case, $\alpha = 2$. If we consider the same matrix as in MF, then by trimming the two lowest and two highest values of the sorted set we will have the central subset {7, 9, 10, 15, 17}. The average of this subset is 11.6, which is substituted for the center pixel value.

2.4.5 Rainfall Rate Computation

The single image rainfall rates are calculated for each GOES IR image available every 1-hour in this study. The average hourly rainfall rate is computed on a pixel-by-pixel basis using a statistical tri-mean (Wilks, 1995) of three consecutive images. The tri-mean is a weighted average in which the median of the three values receives twice the weight, so that for every pixel the hourly rainfall rate is given as

$$Rain_h (mm/hr) = (Rain_{h-1} + 2Rain_h + Rain_{h+1}) / 4 \quad (2.7)$$

The accumulated rainfall rate for periods longer than 1-hour (e.g., daily) is computed by summing the rainfall rates for all 1-hour collocated pixels in the desired period.

2.5 Assessment of IMRA Rainfall Estimates

The performance of the IMRA technique presented here is based on four months of data, June-July 2002 and August-September 2003. Although both data sets represent summer period which is normally dominated by convective rainfall systems, the summer in 2002 had a relatively light rainfall as compared to the summer in 2003 (see Figure 2.6), and hence the two sets of data were deemed suitable for testing the performance of IMRA for estimating relatively light and heavy rainfall. An effective 35 x 20 pixels window at 4 km pixel resolution covering Peace River Basin and its vicinity was used, where with border pixels included the window was 37 x 22 pixels. Hourly satellite rainfall rates were computed using IMRA with (a) threshold only, (b) threshold plus slope, (c) threshold plus hessian, (d) threshold plus slope or hessian and Spatial filter, and (e) threshold plus slope or hessian and Microwave (MW) adjustment factors. This procedure of sequential addition of

correction factors was employed in order to assess the influence of each factor on the derived rainfall rate.

The statistical criteria used to validate the IMRA satellite rainfall estimates are the mean, bias, root-mean-square error (RMSE), and correlation coefficient. Contingency tables index (False Alarm Ratio (FAR), Probability of Detection (POD), and error (ERR)) and rain area are used to evaluate the IMRA rainfall estimates qualitatively, particularly its rain/no-rain discrimination component. FAR is the number of points incorrectly classified as rain (false alarms) divided by the sum of the points correctly classified as rain (rain hits) and the false alarms; POD is the number of rain hits divided by the sum of points incorrectly classified as no rain (rain misses) and the rain hits; and ERR is the sum of the rain misses and false alarms divided by the total number of points under consideration. IMRA rainfall estimates are validated on hourly and daily basis for different spatial scales (4 km, 12 km, and 20 km). Two rainfall observation datasets were used in this validation: high-temporal-and-spatial resolution NCEP stage IV gauge-adjusted radar rainfall data and high-quality daily point rain gauge data. The former products were chosen as the primary ground-truth for comparing with IMRA rainfall estimates because they are available at similar spatial resolution (i.e., 4 km x 4 km) as the GOES IR rainfall data. For the case of point scale comparison and hydrologic simulations, the point gauge rainfall were also used at daily time step. The daily gauge rainfall data were considered as independent, because the stage III (from which stage IV is derived) estimates incorporate the 1-hour gauge observations to adjust the radar derived amounts (Fulton et al., 1998). However, the 24-h gauge observations used here are reported solely on a daily basis and hence are not available for processing the hourly stage III/IV data.

2.5.1 Spatial Evaluation of Rainfall Estimates

The results presented here are based on statistics derived from the entire respective time series including the cases with zero rainfall (i.e., unconditional time series).

The unconditional time series allows for equal sample sizes for various spatial scales and rainfall estimation techniques tested in this study.

2.5.1.1 Effect of Cloud-Top-Temperature Gradient Factor

Tables 2.1 and 2.2 show the evaluation results of hourly IMRA rainfall estimates at three spatial scales using the three rain/no-rain pixels screening techniques (i.e., Threshold, Slope, and Hessian) for 2002 and 2003 datasets respectively. Although the Threshold only outperformed the other cases in terms of POD for all three-pixel sizes, it had the worst performance in terms of other statistical measures particularly the mean rainfall rate, bias, and RMSE. Examination of last two rows of Tables 2.1 and 2.2 shows that for Threshold only, the best POD was accompanied by worst FAR and ERR because it produced more number of rain pixels as compared to the observed radar rain pixels. This is because the Threshold (i.e., all pixels with IR TB less or equal to 243°K was considered to be raining) is a crude rain/no-rain discriminator.

The introduction of Slope technique (ST) or Hessian technique (HT) for screening rain/no-rain pixels lowered the POD and slightly increased the correlation (particularly the ST case; i.e., Threshold + Slope) but significantly improved the other statistical measures, specifically the mean, bias, and RMSE (Tables 2.1 and 2.2). The trend of IMRA performance on daily basis (Tables 2.3 and 2.4) was more or less similar to the one described for the hourly case, but in this case ST gives a much better results than the other techniques. The better performance provided by ST as compared to HT is due to the fact that HT is a stricter gradient index (it searches for the absolute minimum IR TB pixel) and hence it will tend to remove (i.e., assign zero rainfall) the pixels covered by the stratiform component (which has less spatial temperature gradient) of the convective systems that is normally associated with the mature to dissipating stages of the convective systems (Schumacher and Houze, 2003). For instance, ST provided a better POD, mean rainfall, correlation, and almost identical FAR results to that of HT. However, HT

has better RMSE and ERR statistics than ST (Tables 2.1 to 2.4) because it has a tendency to underestimate rainfall area (i.e., rain pixels) with significant underestimation being associated with light rainfall due to weak IR temperature gradient, which directly leads to smaller RMSE and ERR values. This can be seen in Tables 2.1 to 2.4 where the rain area (i.e., raining pixels) for the Hessian case was relatively smaller than the Slope case.

The 1-hour measure scores were much lower than those of 24-hour precipitation estimates indicating that the IMRA had less skill over 1-hour than over 24-hour periods (see Tables 2.1 to 2.4). The skill measures that showed the greatest improvement from hourly to daily rainfall rates were POD and FAR. Tables 2.1 to 2.4 also show that overall the skill scores improved when IMRA estimates were performed on a lower spatial resolution grid, such as 20 km x 20 km as opposed to the native (4 km x 4 km) grid. Apparently by averaging the time and spatial scales, we expect better agreements between observed and satellite data retrieved rainfall fields. The estimates show a good fit at a resolution of 12km and lower particularly in terms of mean rainfall, correlation, RMSE, and POD. Generally the ST (i.e., Threshold + Slope) outperformed both the HT (i.e., Threshold + Hessian) and Threshold only, on both hourly and daily basis, by producing rainfall estimates that are more comparable to the observed (i.e., gauge-adjusted radar rainfall data). Since the performance of the Threshold only was clearly poorer as compared to the other two techniques particularly in terms of the quantitative measures (i.e., mean rainfall, bias, RMSE) with exception of correlation coefficient, it will not be discussed any further in this section.

2.5.1.2 Effect of Spatial Smoothing/Filtering

In an attempt to further improve the IMRA rainfall estimates, three spatial smoothing/filtering techniques were tested, namely, quad smoothing (QS), median filter (MF), and trimming filter (TF). Due to the large quantity of information, the results of this analysis are not presented here. Among the three spatial smoothing

techniques, the MF (i.e., Threshold + Slope/Hessian + MF) tended to reduce both the rain area and mean rainfall as compared to Threshold + Slope/Hessian. On the other hand, QS and TF generally tended to increase the rain area substantially in comparison to Threshold + Slope/Hessian, with QS rain area being larger than that of TF, while maintaining and dampening the pixel's mean rainfall estimates respectively. Therefore, in general the spatial smoothing/filtering techniques were not effective in improving the rainfall estimates from Threshold + Slope/Hessian techniques.

2.5.1.3 Effect of Microwave (MW) Adjustment Factor

Finally, the application of the microwave (MW) adjustment factor generally led to underestimation of observed rainfall and hence resulted in poorer statistics such as mean rainfall, bias, RMSE, and correlation coefficient (compare Table 2.5 with Tables 2.3 and 2.4). This can be partly associated with the poor sampling frequency of the microwave data (once or twice per day) as compared to the hourly IR data, and partly due to the possibility of diurnal characteristics of the rainfall system over the study site. To investigate the diurnal effect, the basin mean areal precipitation (MAP) derived from the gauge-adjusted radar rainfall data were averaged over 24 hours for the 31-day period of August 2003. The resulting 24-h time series strongly shows a diurnal trend in the observed rainfall system (Figure 2.7), where despite the hourly variability in the values, there is a persistent similarity in timing of the daily maximums and minimums of rainfall occurrence where most of the rainfall started at late evening (around 17:00 hours) to mid-night. The observed mean rainfall amounts were lowest at around 8:00 hours (morning) and increased into the evening, peaking near 21:00 hours. This means that if the low-orbit satellite measuring the MW data is consistently making over-passes through this region (Florida, USA) during the morning and/or early afternoon times, it will be missing the rainfall events and hence the resulting observed underestimation of the MW adjusted IR rainfall estimates. It is plausible that the diurnal trend had an impact in the MW adjusted IR rainfall estimates. However, the forcing of this diurnal trend is

not immediately apparent. The timing of the maximum and minimum rainfall occurrences do not coincide with that expected if rainfall were forced by the solar cycle. Under those circumstances, the maximum should occur during late afternoon, when convection is more likely to occur.

These results and others (e.g., Arkin and Xie, 1994; Miller et al., 2001) show that, there is no strong evidence that combined techniques (i.e., IR-microwave techniques) will necessarily give better performance than IR-only techniques. Besides the diurnal effect explained above, another possible explanation is that it is difficult to estimate accurately the high spatial and temporal variability of the precipitation field at hourly or daily time step with the microwave data characterized by coarser spatial and temporal resolutions. Generally MW data are better for monthly time step or longer and lower spatial resolutions such as $2.5^{\circ} \times 2.5^{\circ}$ (Xu et al., 1999).

2.5.2 Point Scale Evaluation of Rainfall Estimates

2.5.2.1 Cumulative Traces of Rainfall Rates

The performance of IMRA was also considered at point scale (i.e., at rain gauge locations) on a daily basis. Since the trend of the plots was the same, the results for only one rain gauge location (i.e., Arcadia, see Figure 2.1 for its location) are presented. The cumulative rainfall plots comparing gauge, radar, and GOES satellite rainfall estimates using different IMRA components (i.e., Threshold, Slope, and Hessian) for 2002 and 2003 datasets are shown in Figures 2.8 and 2.9 respectively. It can be clearly seen that the use of 243°K threshold only for discriminating rain/no-rain pixels provides IMRA estimates that significantly overestimate the gauge and radar rainfall for both 2002 and 2003 datasets (Figures 2.8a and 2.9a).

For the 2002 dataset, the introduction of Slope technique (ST) in addition to Threshold for rain/no-rain discrimination resulted in an IMRA cumulative rainfall

plot that follows the radar trace closely, although it slightly underestimated the gauge measurements (Figure 2.8b). On the other hand, the Hessian technique (HT) of rainfall area delineation resulted into IMRA estimates significantly underestimating both the gauge and radar measurements almost throughout the 2-months (i.e., 61 days) (Figure 2.8c). The introduction of ST for the 2003 dataset resulted into three plots (i.e., gauge, radar, IMRA estimates) collapsing together in good agreement (Figure 2.9b). The Hessian estimates for 2003 dataset resulted in a significantly good agreement with gauge and radar measurements as compared to the 2002 dataset (Figure 2.9c).

From Figures 2.8 and 2.9, it seems that the Slope Technique generally outperformed both Hessian and Threshold techniques. ST performance for the 2002 case was more or less equal to that of 2003 case, while the HT performed much better in 2003 than in 2002 datasets. This can be attributed to the fact that, the 2002 dataset composed of relatively light rainfall while the 2003 period had relatively heavy rainfall (Figure 2.6). It is likely that heavier precipitation amounts were associated with deep convection while the light precipitation amounts were produced by shallow warm-top clouds (i.e., stratiform systems). Tables 2.1 and 2.2 show the number of raining pixels reported by the hourly gauge-adjusted radar rainfall data (observed data) for the two months each in 2002 and 2003 datasets, which were 137,802 and 93,744 pixels respectively at the native (i.e., 4 km) pixel resolution. It can be seen that the raining pixels for the 2002 case was about 1 ½ times that of 2003, while the observed mean rainfall for 2003 was slightly more than that of 2002 (see Table 2.1 and 2.2). On daily basis (Tables 2.3 and 2.4), it is clear that the 2002 observed dataset reported more rain area (but less mean rainfall) while the 2003 case has less rain area (but more mean rainfall) at all spatial scales tested. These facts and the time series plots of daily point gauged data in Figure 2.6 show that the magnitudes of rainfall rate for 2002 was generally less than that of 2003. This means that the 2002 datasets were dominated by a persistent wide spread rainfall systems while the 2003 were dominated by localized intense

thunderstorms which are typical characteristics of stratiform (warm-cloud) and convective (cold-cloud) rainfall systems, respectively (Schumacher and Houze, 2003). Thus, since HT is a stricter gradient index (where a rain pixel needs to be an absolute minimum IR TB as compared to the surrounding pixels) than ST (where rain pixels do not necessarily have to be absolute minima IR TB) it will tend to remove (assign zero rainfall) more pixels covered by the stratiform rainfall systems because they have less spatial temperature gradient. Also, HT was specifically developed for delineating heavy convective precipitation systems characterized by high cloud-top temperature gradient for flood forecasting (Vicente et al., 1998; Rozumalski, 2000). Hence, this can explain the observed underestimation of rainfall depth and rain area by HT as compared to ST for the 2002 dataset dominated by stratiform rainfall systems.

2.5.2.2 Daily Comparison of Rainfall Rates at Grid Points

The scatter plots of the daily estimates by IMRA Slope (ST) and Hessian (HT) versus gauge-adjusted radar rainfall estimates for both 2002 and 2003 datasets are displayed in Figures 2.10 and 2.11 for the case of 20 km and 100 km resolution grids, respectively. When compared with HT, the ST demonstrates better agreement with the radar rainfall data. The HT shows a general tendency to underestimate the observed rainfall at 20 km resolution grid for both 2002 and 2003 datasets (Figure 2.10). At 100 km resolution and hence a smaller sample size, it can be clearly seen that the distributions of satellite rainfall estimates for convective rainfall (Figures 2.11c and 2.11d) more closely correlate with radar data than that of stratiform rainfall (Figures 2.11a and 2.11b) because satellite data have difficulty estimating warm cloud stratiform rainfall systems. Also, the underestimation effect of HT is significantly reduced at 100 km resolution, particularly in the 2003 dataset (Figure 2.11d) because of the large averaging area.

2.5.2.3 Histograms of Rainfall Rates

The frequency distribution of rainfall rates estimated by satellite data and the gauge-adjusted radar data on daily basis at both 20 km and 100 km resolution grids are depicted in Figures 2.12 and 2.13 for 2002 and 2003 datasets, respectively. The HT derived satellite measurements significantly overestimated the frequency of rainfall rate within 0.0-2.0 mmh⁻¹ at 20 km resolution grid for both 2002 and 2003 datasets. As mentioned earlier, this is because HT is a stricter gradient index than the ST and hence have difficulty estimating small rainfall rates that are normally associated with warm-clouds (i.e., stratiform clouds) which resulted in many zero rainfall rates derived from satellite data and hence the overestimation of rainfall occurrences within 0.0-2.0 mmh⁻¹ range (Figures 2.12a and 2.13a). For the 100 km resolution grids the overestimation of small rainfall rates occurrences by HT is significantly reduced because of the large averaging area (Figures 2.12b and 2.13b). Note that although both ST and HT share similar frequency distributions, generally ST demonstrates better agreement with the gauge-adjusted radar rainfall data (Figures 2.12 and 2.13).

2.5.3 Hydrologic Simulation

Several studies have been carried out to investigate the potential of applying satellite rainfall estimates in hydrologic modeling. Hardy et al. (1989) used daily satellite rainfall as input to a conceptual rainfall-rainfall model for daily flow prediction in two sub-catchments of the Senegal River Basin. They reported that the flow predictions were at least as good when satellite rainfall estimates were used instead of conventional raingauge data. In another study for Tano River in West Africa, Papadakis et al. (1993) found that the model simulations of monthly runoff compared equally well between observations from the satellite and that of raingauges. Tsintikidis et al. (1999) conducted a similar analysis for the Nile River Basin using a conceptual semi-distributed model with daily time step and 1⁰ x 1⁰ discretization. In their case a minor improvement was found using the remotely

sensed rainfall and they recommended its use as input in hydrologic models. Andersen et al. (2002) used rainfall estimates from METEOSAT satellite data as input to a distributed, physics-based hydrologic model applied to three subcatchments in the Senegal River Basin. They reported similar model performances when the gauge and satellite rainfall data were used for simulation of observed streamflow hydrographs. In all these studies either a bi-spectral technique of Tsonis et al. (1996) or the cold cloud duration (CCD) technique of Arkin and Meisner (1987) was used to derive the satellite rainfall estimates. Tsintikidis et al. (1999) recommended the modification of the bi-spectral technique (i.e., into a univariate frequency analysis method where only IR is used) to enable it to resolve a nighttime rainfall. This is because using the VISIBLE channel hinders the estimation of rainfall during the night because visible satellite images will not be available. Andersen et al. (2002) pointed out that CCD technique relies heavily on statistical relations and it is questionable to which degree it captures the physical processes. Furthermore, the calibration of infrared and visible satellite images was done using raingauge data at daily time step, which meant poor time coincidence between the daily surface rainfall and hourly satellite images. All these factors can potentially lead to less accurate satellite-derived rainfall estimates.

An assessment of suitability of IMRA rainfall estimates derived from satellite infrared (IR) images for hydrologic studies is carried out at daily time step. The use of IR images alone allows the estimation of rainfall at day and night which potentially leads to more accurate daily satellite rainfall estimates as compared to the combined use of IR and visible (not available during the night) images. Also, IMRA derives rainfall from IR images by employing the physical processes of the cloud-top structure as described in section 2.4. Due to a lack of detailed input data, the Sacramento soil moisture accounting (SAC-SMA) model is used to generate streamflow because it needs only rainfall and potential evapotranspiration as input data, as well as streamflow data for model calibration. The results are compared with streamflow estimated using raingauge and gauge-adjusted radar rainfall data.

2.5.3.1 Sacramento Soil Moisture Accounting (SAC-SMA) Model

SAC-SMA is a conceptual rainfall-runoff model of the complex natural processes associated with the generation of surface and sub-surface runoff in natural catchments with spatially lumped parameters (Burnash et al., 1973; Burnash, 1995). The model divides the soil column into an upper and a lower zone, each having “free” and “tension” water storages (see Figure 2.14). The upper zone represents the upper soil storage (in the top 10-20 cm of the soil depth), while the lower zone represents the bulk of the soil moisture and, in some cases, groundwater storage. Tension water is assumed closely bound to the soil particles and is removed only by evapotranspiration. Free water is free to move horizontally and vertically through the soil column, and can be depleted as a channel inflow, non-channel groundwater flow and as percolation from the upper zone to the lower zone. Percolation controls the movement of water throughout the soil profile, and also depends on the degree of saturation in both the upper and lower zones. Parameters of the model include: capacities of five soil compartments; drainage rates from the free water zones; fraction of impervious areas; percolation parameters; and baseflow parameters.

SAC-SMA is generally applied to river basins ranging from 300 km² to 5000 km² (Finnerty et al., 1997), and is normally run at 6-hour or daily time step. It uses mean areal precipitation (MAP) and mean areal potential evapotranspiration (MAPE) demand as inputs to produce streamflow at the catchment outlet. The SAC-SMA model parameters are manually and automatically calibrated with the objective of optimizing the match between simulated and the observed discharge data.

In this study, SAC-SMA was applied at both basin and sub-basin scales in daily time step. Since the size of the Peace River Basin (PRB) at Arcadia streamflow

gauging station used here is 5416 km², which translates to around 0.74⁰ x 0.74⁰ (i.e., 74 km x 74 km) single grid size, it is within the recommended range of basin sizes for applying the SAC-SMA model. The potential evapotranspiration data were estimated using a simple Hargreaves model (Wu, 1997) that requires only two climatic parameters, temperature and incident radiation as follows;

$$ET_0 = 0.0135(T + 17.78)R_s \left(\frac{238.8}{595.5 - 0.055T} \right) \quad (2.8)$$

where ET_0 is the potential evapotranspiration (mm/day), T the mean temperature (⁰C), and R_s the incident solar radiation (MJ/m²/day). The temperature data were available on daily basis while the solar radiation data were available on monthly averages and hence the radiation values were assumed constant for all days of a particular month. Wu (1997) showed that the simple Hargreaves model performed comparably with the complicated Penman model, which requires many climate data such as air temperature, relative humidity, wind, saturation vapor pressure, net radiation, roughness height, atmospheric pressure, and air density.

During the calibration of SAC-SMA, the input data used were daily gauge MAP, MAPE, and observed streamflow at Arcadia gauging station, which is a non-tidal station (see Figure 2.1). The gauge MAP was computed using four rain gauges located above the Arcadia basin outflow namely Bartow, Fort Green, Wauchula, and Arcadia rain gauge stations (see Figure 2.1). Three years of data (1997-1999) were used for calibrating SAC-SMA. This period was selected because it composed a wide range of daily streamflow magnitudes recorded at Arcadia gauging station. Two sets of data were employed in the validation of SAC-SMA, which composed of three years (1982-1984) and four years (1971-1974) of data for validations 1 and 2 respectively. The calibration and validation results are shown in Figure 2.15. The statistics of the simulated streamflow during calibration and validation of the SAC-SMA model are shown in Table 2.6. All calibration and validation statistics are comparable and encouraging. Finnerty et al. (1997) showed that SAC-SMA's parameters are inherently tied to the space-time scale, terrain, geographic location,

and gauge network from which they are calibrated. Optimally, a lumped basin that is disaggregated into sub-basins should be recalibrated to reflect the model's response to a different space scale. Obled et al. (1994) followed this procedure when they modeled a basin in a lumped fashion and then in a semi-distributed manner with 9 sub-basins. Since there is no streamflow gauging station above the Arcadia station (Figure 2.1) for re-calibrating the model at sub-basin scale, the calibrated SAC-SMA model parameters at a lumped basin scale were applied to evaluate the suitability of satellite rainfall estimates at both basin and sub-basin scales to see if the spatial distribution of precipitation play a part in basin-scale hydrologic modeling. A Muskingum routing scheme was used to route the streamflow from different sub-basins to the basin outlet, and its parameters were determined by trial and error.

2.5.3.2 Using IMRA Rainfall Estimates in Hydrologic Modeling

The streamflow simulation results based on IMRA precipitation estimates derived with Slope and Hessian techniques with and without microwave adjustment are presented in Figure 2.16. In this figure and the rest of the figures in this section, the first 61 days (i.e., 1 – 61) represent the period from June 1 – July 31, 2002 and the remaining 61 days (i.e., 62 – 122) represent the period from August 1 – September 30, 2003. In each case described here, the two datasets were combined to form a time series with 122 data points for use in the hydrologic simulation. It can be seen that the use of satellite rainfall derived by Slope technique (ST) for streamflow prediction produced a hydrograph that agrees closely with the observed in both 2002 and 2003 periods (Figure 2.16a). On the other hand, the use of Hessian technique (HT) for rain/no-rain discrimination resulted in significant underestimation of observed streamflow for 2002 period while in 2003 period there is a better agreement with the observed hydrograph (Figure 2.16b). There was no obvious improvement by introducing the microwave (MW) adjustment because it led to a general underestimation of observed streamflow in both ST and HT (Figure 2.16). The 2002 period experienced more underestimation than 2003 period because

the former was dominated by relatively light rainfall which is potentially associated with warm-clouds that are difficult to detect by high frequency microwave channels used here (i.e., 85.5 GHz) since they measure rainfall through scattering mechanism by the ice and rain particles and hence smaller particles will scatter less MW energy and vice versa (Chen and Li, 2002). These observations are consistent with those in sections 2.5.1.1 to 2.5.1.3 of IMRA rainfall estimates evaluation.

For comparison with the gauge and radar simulated streamflow hydrographs, the satellite rainfall estimates during the 2002 period were derived using a Slope technique and those of 2003 period were derived using both the Slope and Hessian techniques (Figure 2.17). In Figures 2.17a and 2.17b the streamflow simulation was based on a lumped basin while the results in Figure 2.17c are based on the basin divided into 4 sub-basins (see Figure 2.1) where the streamflow from different sub-basins was routed to the basin outlet through a Muskingum routing scheme. However as stated earlier, due to a lack of observed streamflow data at interior sub-basins for recalibrating the model at each sub-basin, the lumped basin parameters were also used in the sub-basin case. It can be seen that, at a lumped basin scale the radar hydrographs (Figure 2.17a) are marginally better than satellite and gauge hydrographs (Figure 2.17 and Table 2.7). However, at a sub-basin scale, the satellite hydrographs (i.e., Slope/Hessian) outperformed that of gauge and was very close to radar results (Figure 2.17c and Table 2.7) reflecting the potential of satellite precipitation estimates over gauge measurements in hydrologic modeling. However, the satellite precipitation scenarios shows some deviations from the rain gauge and radar scenarios, e.g., the overestimation of the peak at around day 73 and the underestimation and miss timing of the trough at around days 91 to 98. Also, the performance of Slope technique in 2003 (i.e., day 62 to 122) was slightly poor as compared to Hessian, which resulted to the deviation observed at around day 73 (Figures 2.17b and 2.17c). But, generally the deviations are modest and the few cases of over/under-estimation with the satellite precipitation seem to be balanced by the improved simulations in other periods, for instance the last peak at around

day 101 which was underestimated by both gauge and radar rainfall data (Figures 2.17b and 2.17c).

Generally, ST produced better satellite rainfall estimates than HT for the case of stratiform rainfall (i.e., 2002 dataset), while the HT performed slightly better than ST in the case of convective rainfall (i.e., 2003 dataset). Independent qualitative and quantitative analysis of the HT (Rozumalski, 2000) has demonstrated that in contrast to the reasonable performance of HT for well-defined and short duration convective systems, poor results are common for stratiform cloud systems. The intense convective systems are the ones for which the Hessian technique was originally developed, and hence the technique is expected to perform better during these events, although overestimation of daily rainfall accumulations was reported (Vicente et al., 1998; Rozumalski, 2000). These observations are consistent with the results obtained in this study (Figure 2.16b).

Improved simulation at sub-basin scale seems to depend partly on the spatial distribution of precipitation input, and partly on the process relations, grid scale, and the calibration of hydrologic model parameters (Andersen et al., 2002). It seems that the model performance is marginally improved by providing spatially more refined precipitation data. If the hydrologic model parameters can be recalibrated at sub-basin scales, we anticipate the possibility of further improving basin-scale hydrologic modeling from the satellite-based IMRA rainfall estimates obtained in this study. Also, Guetter et al. (1996) and Tsintikidis et al. (1999) found that the response of a hydrologic model depends substantially on the source of precipitation forcing (i.e., raingauges or satellite platforms). That is, using satellite rainfall data requires re-calibration of hydrologic models with satellite rainfall data. Hence, the observed slightly better performance of gauge precipitation as compared to satellite precipitation (e.g., Slope technique) in streamflow prediction can be attributed to the fact that the SAC-SMA model parameters used for both scenarios were derived using gauge precipitation data.

2.6 Summary and Conclusions

An Infrared-Microwave Rainfall Algorithm (IMRA) for estimating rainfall at high spatial and temporal scales from TRMM and GOES satellite data is developed and validated. It is designed to require less input information, be less dependent on rain gauge data, utilize infrared (IR) brightness temperatures (TBs) as the main satellite input information, and use the Slope technique (ST) and Hessian technique (HT) to determine the IR image cloud-top temperature gradient for discriminating rain/no-rain pixels, in addition to the 243°K IR threshold temperature. The IMRA allows for the adjustment of the derived IR-rainfall estimates using microwave (MW) TBs information and spatial filtering/smoothing techniques. The evaluation of IMRA rainfall estimates was based on four months of data: June-July 2002 (with relatively light rainfall) and August-September 2003 (with relatively heavy rainfall), with the intention of testing the performance of IMRA for estimating relatively light and heavy rainfall. Further analysis of these datasets showed that, the 2002 dataset were dominated by stratiform rainfall while those of 2003 were dominated by convective rainfall.

The IMRA rainfall estimates were validated on hourly and daily basis for different spatial scales (4 km, 12 km, 20 km, and 100 km). Two observed rainfall datasets were used in this validation: high temporal and spatial resolutions, NCEP stage IV gauge-adjusted radar rainfall data and high-quality daily point rain gauge data. The hourly NCEP stage IV radar products were chosen as the primary ground-truth precipitation for comparison with the IMRA rainfall estimates because they are available at similar spatial resolution (i.e., 4 km x 4 km) as the GOES IR brightness temperatures used herein for satellite rainfall estimation. The IMRA rainfall estimates were assessed with respect to the corresponding gauged and radar rainfall data, and the streamflow simulated by SAC-SMA driven by these rainfall data. The conclusions of the study are summarized below:

- The Slope technique (ST) provides good satellite rainfall estimates for both stratiform and convective systems (i.e., 2002 and 2003 datasets respectively), while the Hessian technique only provides good estimates for convective systems.
- At daily time step, there was no improvement in satellite rainfall estimates by introducing the microwave (MW) adjustment factor. Instead, it led to a general underestimation in both ST and HT cases.
- The modest correlation between satellite rainfall estimates and gauge-adjusted radar rainfall data at various spatial/pixel scales tested suggests that satellite data have difficulty identifying the proper locations of observed raining pixels.
- In hydrologic simulation, streamflow prediction at basin-scale based on satellite data outperformed that of gauge and was very close to radar streamflow estimates, reflecting the potential of satellite precipitation estimates in hydrologic modeling. Precipitation input at sub-basin scales (e.g., 4 sub-basins) consistently produce more accurate streamflow hydrographs marginally than basin-scale input for all input data types.
- For future work, it is recommended that IMRA satellite rainfall estimates should be applied at sub-basin scale with model parameters also re-calibrated at sub-basin scale, in river basin(s) of various climatic/geographical conditions, and the development of techniques for identification of rainfall type in real-time using satellite data.

References

- Adler, R. F., and Negri, A. J. (1988), A satellite infrared technique to estimate tropical convective and stratiform rainfall. *J. of Applied Meteorology*, 27, 30-51.
- Adler, R. F., Negri, A. J., Keehn, P. R., and Hakkarinen, I. M. (1993), Estimation of monthly rainfall over Japan and surrounding waters from a combination of low-orbit microwave and geostationary IR data. *J. of Applied Meteo.*, 32, 335-356.
- Andersen, J., Dybkjaer, G., Jensen, K. H., Refsgaard, J. C., and Rasmussen, K. (2002), Use of remotely sensed precipitation and leaf area index in a distributed hydrological model. *J. of Hydrology*, 264, 34-50.
- Arkin, P. A., and Meisner, B. (1987), The relationship between large-scale convective rainfall and cold cloud over the Western Hemisphere during 1982-1984. *Monthly Weather Review*, 115, 51-74.
- Arkin, P. A., and Xie, P. (1994), The Global Precipitation Climatology Project: First Algorithm Intercomparison Project. *Bul. American Meteoro. Soc.*, 75, 401-418.
- Burnash, R. J. C. (1995), The NWS River Forecast System – catchment modeling. In: Singh V. P. (Ed.), *Computer Models of Watershed Hydrology*. 311-366.
- Burnash, R. J. C., Ferral, R. L., McGuire, R. A. (1973), *A generalized streamflow simulation system – conceptual modeling for digital computers*. U.S. Department of Commerce, National Weather Service and State of California, Department of Water Resources.
- Chen, W. -J., and Li, C. -C. (2000), Oceanic rain rate retrievals using TRMM Microwave Imager multi-channel brightness temperatures during the 1998 SCSMEX. *Terrestrial, Atmospheric and Oceanic Sciences*, 11, 765-788.
- Chen, W. -J., and Li, C. -C. (2002), Rain retrievals using Tropical Rainfall Measuring Mission and Geostationary Meteorological Satellite 5 data obtained during the SCSMEX. *Int. J. of Remote Sensing*, 23(12), 2425-2448.
- Datta, D., Jones, W. L., Roy, B., and Tokay, A. (2003), Spatial variability of surface rainfall as observed from TRMM field campaign data. *J. of App. Meteo.*, 42, 598-610.

- Efford, N. (2000), *Digital Image Processing: A Practical introduction using Java*. Addison-Wesley, 340 pp.
- Finnerty, B. D., Smith, M. B., Seo, D. J., Koren, V., and Moglen, G. E. (1997), Space-time scale sensitivity of the Sacramento model to radar-gage precipitation inputs. *J. of Hydrology*, 203, 21-38.
- Fulton, R. A., Breidenbach, J. P., Seo, D. -J., Miller, D. A., and O'Bannon, T. (1998), The WSR-88D rainfall algorithm. *Weather and Forecasting*, 13, 377-395.
- Gagin, A., Rosenfeld, D. and Lopez, R. E. (1985), The relationship between height and precipitation characteristics of summertime convective cells in South Florida. *J. of Atmospheric Sciences*, 42, 84-94.
- Griffith, C. G., Woodley, W. L., Grube, P. G., Martin, D. W., Stout, J., and Sikdar, D. N. (1978), Rain estimates from geosynchronous satellite imagery: Visible and infrared studies. *Monthly Weather Review*, 106, 1153-1171.
- Guetter, A. K., Georgakakos, K. P., Tsonis, A. A. (1996), Hydrologic applications of satellite data 2. Flow simulation and soil water estimates. *J. Geophys. Res.*, 101, 26527-26538.
- Hardy, S., Dugdale, G., Milford, J. R., and Sutcliffe, J. V. (1989), The use of satellite derived rainfall estimates as inputs to flow prediction in the River Senegal. New directions for surface water modeling. *Proceedings of the Baltimore Symp.*, # 181 in IAHS publications.
- Hong, Y., Hsu, K., Sorooshian, S., and Gao, X. (2004), Precipitation Estimation from Remotely Sensed Imagery using an Artificial Neural Network Cloud Classification System. *J. of App. Meteo.*, 43, 1834-1852.
- Jain, A. K., (1989), *Fundamentals of Digital Image Processing*. Prentice Hall, 350 pp.
- Klazura, G. E., and Imy, D. A. (1993), A description of the set of analysis products available from the NEXRAD WSR-88D system. *Bull. Amer. Meteo. Soc.*, 74, 1293-1311.
- Marzano, F. S., Palmacci, M., Cimini, D., Giuliani, G., and Turk, F. J. (2004), Multivariate statistical integration of satellite infrared and microwave radiometric

- measurements for rainfall retrieval at the geostationary scale. *IEEE Transactions on Geoscience and Remote Sensing*, 42(5), 1018-1032.
- Miller, S. W., Arkin, P. A., and Joyce, R. (2001), A combined microwave/infrared rain rate algorithm. *Int. J. Remote Sensing*, 22, 3285-3307.
- Obled, C. H., Wendling, J., and Beven, K. (1994), The sensitivity of hydrological models to spatial rainfall patterns: an evaluation using observed data. *J. of Hydrology*, 158, 305-333.
- Papadakis, I., Napiorkowski, J., and Schultz, G. A. (1993), Monthly runoff generation by nonlinear model using multispectral and multitemporal satellite imagery. *Adv. Space Res.*, 13, 5-12.
- Rozumalski, R. A., (2000), A quantitative assessment of NESDIS Auto-Estimator. *Weather and Forecasting*, 15, 397-415.
- Schumacher, C., and Houze, R. A. (2003), Stratiform rain in the tropics as seen by the TRMM Precipitation Radar. *J. of Climate*, 16, 1739-1756.
- Todd, M. C., Barrett, E. C., Beaumont, M. J., and Bellerby, T. J. (1999), Estimation of daily rainfall over upper Nile river basin using continuously calibrated satellite infrared technique. *Meteorological Applications*, 6, 201-210.
- Tsintikidis, D., Georgakakos, K. P., Artan, G. A., and Tsonis, A. A. (1999), A feasibility study on mean areal rainfall estimation and hydrological response in the Blue Nile region using METEOSAT images. *J. of Hydrology*, 221, 97-116.
- Vicente, G. A., Scofield, R. A., and Menzel, W. P. (1998), The operational GOES infrared rainfall estimation technique. *Bull. Amer. Meteo. Soc.*, 79 (9), 1883-1898.
- Weir, M. D., Hass, J, and Giordano, F. R. (2006), *Thomas' Calculus: Early Transcendentals, 11th Ed.* Addison Wesley, 1015 pp.
- Wilks, D. S. (1995), *Statistical Methods in the Atmospheric Sciences*. Academic Press, 467 pp.
- Wu, P. (1997), A Simple Evapotranspiration Model for Hawaii: The Hargreaves Model. Online at <http://www.ctahr.hawaii.edu/oc/freepubs/pdf/EN-106.pdf>

Xu, L., Gao, X., Sorooshian, S., Arkin, P. A., and Imam, B. (1999), A microwave infrared threshold technique to improve GOES Precipitation Index. *J. of App. Meteo.*, 38, 569-579.

Table 2.1 Comparison of rainfall rate statistics for IMRA (Threshold, Slope, & Hessian) at three pixel sizes for June 1- July 31, 2002 dataset in HOURLY basis. Bold-faced values show the best statistics.

Version	Threshold			Threshold + Hessian			Threshold + Slope		
	4km	12km	20km	4km	12km	20km	4km	12km	20km
Grid size	4km	12km	20km	4km	12km	20km	4km	12km	20km
Sample size	1024800	122976	40992	1024800	122976	40992	1024800	122976	40992
Correlation	0.09	0.15	0.17	0.02	0.09	0.14	0.05	0.14	0.18
GOES Mean	1.40	1.41	1.40	0.06	0.06	0.06	0.38	0.38	0.38
Radar Mean	0.22	0.33	0.33	0.22	0.33	0.33	0.22	0.33	0.33
Bias	5.33	3.22	3.22	-0.73	-0.82	-0.82	0.72	0.14	0.14
RMSE	28.28	16.36	15.95	16.39	3.56	2.70	20.88	5.16	4.18
FAR	0.68	0.58	0.52	0.67	0.57	0.49	0.67	0.57	0.51
POD	0.54	0.56	0.59	0.01	0.20	0.35	0.13	0.53	0.58
ERR	0.16	0.17	0.16	0.00	0.05	0.09	0.03	0.15	0.16
GOES rain pixels	251828	35266	13009	51244	11858	7489	55224	32771	12751
Radar rain pixels	137802	26334	10694	137802	26334	10694	137802	26334	10694

Table 2.2 Comparison of rainfall rate statistics for IMRA (Threshold, Slope, & Hessian) at three pixel sizes for August 1-September 30, 2003 dataset in HOURLY basis. Bold-faced values show the best statistics.

Version	Threshold			Threshold + Hessian			Threshold + Slope		
	4km	12km	20km	4km	12km	20km	4km	12km	20km
Grid size	4km	12km	20km	4km	12km	20km	4km	12km	20km
Sample size	1024800	122976	40992	1024800	122976	40992	1024800	122976	40992
Correlation	0.16	0.22	0.25	0.04	0.11	0.18	0.10	0.18	0.24
GOES Mean	1.68	1.68	1.68	0.03	0.05	0.05	0.30	0.36	0.36
Radar Mean	0.15	0.39	0.39	0.15	0.39	0.39	0.15	0.39	0.39
Bias	10.24	3.29	3.30	0.99	-0.86	-0.86	1.03	-0.09	-0.09
RMSE	40.47	14.99	14.61	21.47	4.68	3.93	15.67	5.11	4.17
FAR	0.75	0.63	0.56	0.76	0.61	0.53	0.69	0.63	0.56
POD	0.71	0.70	0.71	0.13	0.22	0.42	0.32	0.63	0.69
ERR	0.19	0.19	0.18	0.04	0.05	0.09	0.07	0.17	0.17
GOES rain pixels	267023	36065	13073	53083	10926	7234	98430	32505	12697
Radar rain pixels	93744	19026	8094	93744	19026	8094	93744	19026	8094

Table 2.3 Comparison of rainfall rate statistics for IMRA (Threshold, Slope, & Hessian) at three pixel sizes for June 1- July 31, 2002 dataset in DAILY basis. Bold-faced values show the best statistics.

Version	Threshold			Threshold + Hessian			Threshold + Slope		
	4km	12km	20km	4km	12km	20km	4km	12km	20km
Grid size	4km	12km	20km	4km	12km	20km	4km	12km	20km
Sample size	42700	5124	1708	42700	5124	1708	42700	5124	1708
Correlation	0.11	0.13	0.14	0.03	0.10	0.14	0.10	0.15	0.19
GOES Mean	33.58	33.85	33.58	1.41	1.41	1.41	9.11	9.12	9.11
Radar Mean	7.96	8.01	7.96	7.96	8.01	7.96	7.96	8.01	7.96
Bias	3.22	3.22	3.22	-0.82	-0.82	-0.82	0.14	0.14	0.14
RMSE	6.82	6.73	6.64	1.89	1.57	1.47	2.56	1.89	1.69
FAR	0.23	0.13	0.10	0.19	0.11	0.08	0.21	0.12	0.10
POD	0.91	0.93	0.93	0.14	0.62	0.83	0.76	0.92	0.93
ERR	0.19	0.11	0.09	0.02	0.02	0.06	0.06	0.11	0.09
GOES rain pixels	36043	4556	1563	5476	2990	1370	29373	4508	1559
Radar rain pixels	30516	4302	1518	30516	4302	1518	30516	4302	1518

Table 2.4 Comparison of rainfall rate statistics for IMRA (Threshold, Slope, & Hessian) at three pixel sizes for August 1-September 30, 2003 dataset in DAILY basis. Bold-faced values show the best statistics.

Version	Threshold			Threshold + Hessian			Threshold + Slope		
	4km	12km	20km	4km	12km	20km	4km	12km	20km
Grid size	4km	12km	20km	4km	12km	20km	4km	12km	20km
Sample size	42700	5124	1708	42700	5124	1708	42700	5124	1708
Correlation	0.29	0.32	0.35	0.08	0.20	0.30	0.18	0.29	0.35
GOES Mean	40.22	40.23	40.22	1.29	1.29	1.29	8.53	8.53	8.53
Radar Mean	9.34	9.37	9.34	9.34	9.37	9.34	9.34	9.37	9.34
Bias	3.30	3.29	3.30	-0.86	-0.86	-0.86	-0.09	-0.09	-0.09
RMSE	7.58	7.48	7.42	1.93	1.65	1.53	2.17	1.59	1.39
FAR	0.25	0.13	0.08	0.21	0.10	0.07	0.24	0.13	0.09
POD	0.91	0.91	0.91	0.13	0.58	0.80	0.75	0.90	0.91
ERR	0.20	0.10	0.07	0.02	0.05	0.05	0.15	0.10	0.07
GOES rain pixels	33557	4183	1424	4637	2620	1236	27004	4147	1421
Radar rain pixels	27468	4027	1432	27468	4027	1432	27468	4027	1432

Table 2.5 Rainfall rate statistics for IMRA Slope with MW adjustment (i.e., Threshold + Slope + MW) at three pixel sizes for both 2002 and 2003 dataset in DAILY basis.

Data source	2002			2003		
	4km	12km	20km	4km	12km	20km
Grid size	42700	5124	1708	42700	5124	1708
Sample size	42700	5124	1708	42700	5124	1708
Correlation	0.09	0.13	0.16	0.17	0.26	0.31
GOES Mean	6.31	6.32	6.31	7.13	7.15	7.13
Radar Mean	7.96	8.01	7.96	9.34	9.37	9.34
Bias	-0.21	-0.21	-0.21	-0.24	-0.24	-0.24
RMSE	2.25	1.72	1.58	2.30	1.71	1.53
FAR	0.21	0.12	0.09	0.24	0.13	0.08
POD	0.72	0.91	0.93	0.74	0.90	0.91
ERR	0.15	0.11	0.09	0.15	0.10	0.07
GOES rain pixels	29227	4489	1551	26898	4138	1416
Radar rain pixels	30516	4302	1518	27468	4027	1432

Table 2.6 Statistics of the simulated streamflow hydrographs by SAC-SMA model using gauge rainfall data during calibration and validation periods for the lumped basin approach.

Mode	Date	R² (%)	E_f (%)	Bias (%)	RMSE (%)
Calibration	Jan 1, 1997-Dec 31, 1999	89.98	79.11	-12.88	73.96
Validation1	Jan 1, 1982-Dec 31, 1984	89.02	77.79	-14.29	67.32
Validation2	Jan 1, 1971-Dec 31, 1974	90.84	78.41	-20.04	72.73

Table 2.7 Statistics of simulated hydrographs by SAC-SMA using gauge, radar, and satellite rainfall data during application period. Slope/Hessian means IMRA-Slope was used in 2002 (i.e., day 1-61) and IMRA-Hessian was used in 2003 (i.e., day 62-122) for satellite rainfall estimation.

Data source	Coefficient of determination, R² (%)	Efficiency, E_r (%)	Bias (%)	RMSE (%)
Lumped Basin				
Gauge	87.55	68.20	-17.59	34.18
Radar	88.84	73.21	-12.10	31.37
Slope	82.93	65.28	-10.16	37.23
Slope/Hessian	85.69	68.03	-4.30	34.27
Semi-distributed (4 sub-basins)				
Radar	89.13	74.15	-13.93	30.82
Slope	85.85	69.80	-0.27	32.46
Slope/Hessian	88.25	73.27	+3.27	31.36

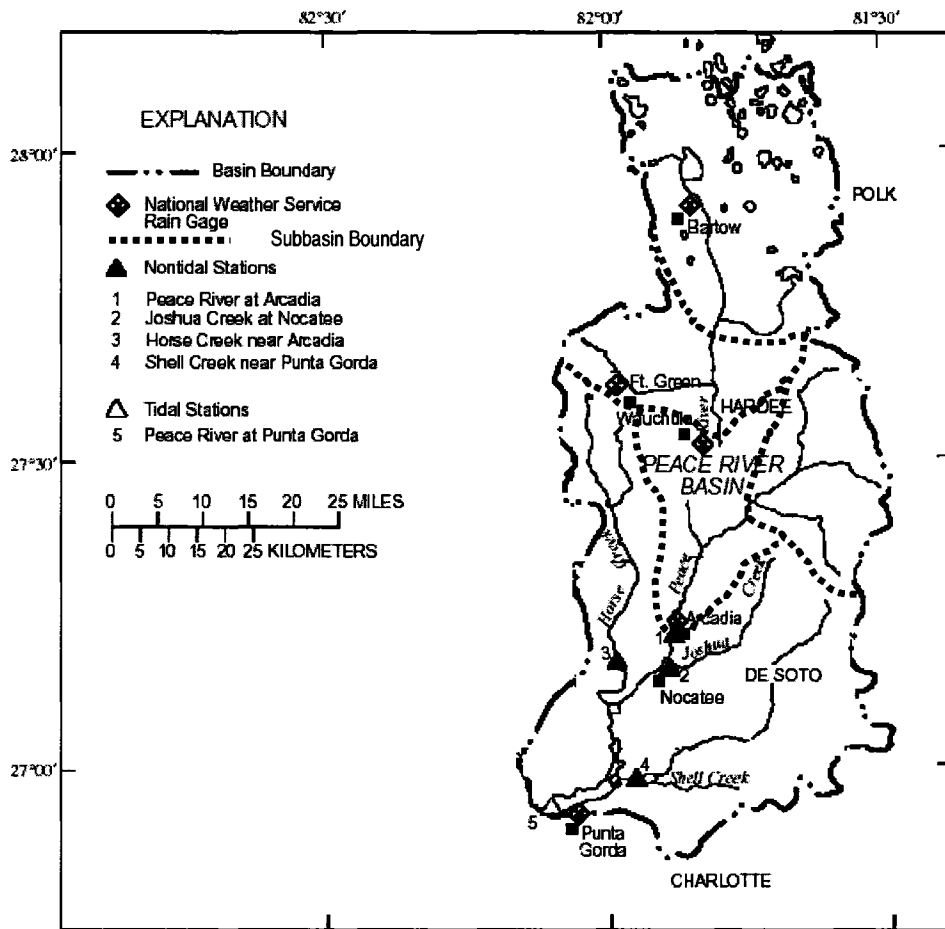


Figure 2.1 Map of Peace River Basin (Source: U.S. Geological Survey).

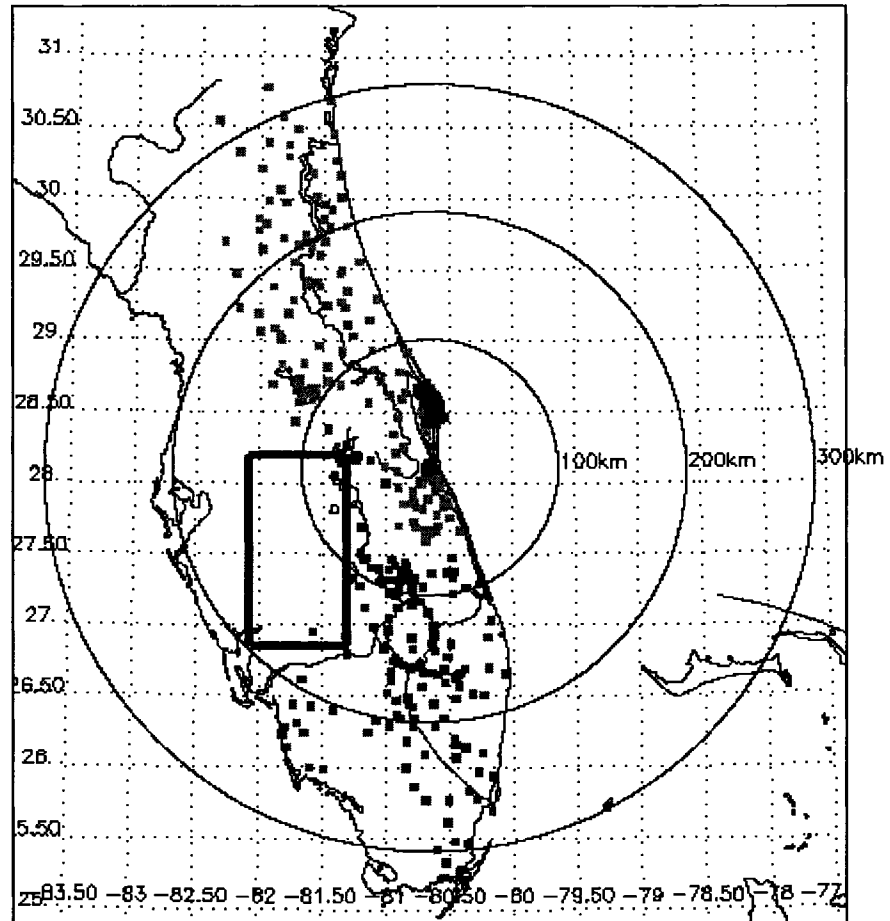


Figure 2.2 Map showing the Florida TRMM satellite ground-validation site. Rain gauge sites are shown in square dots, and the rectangular box indicates the location of Peace River Basin.

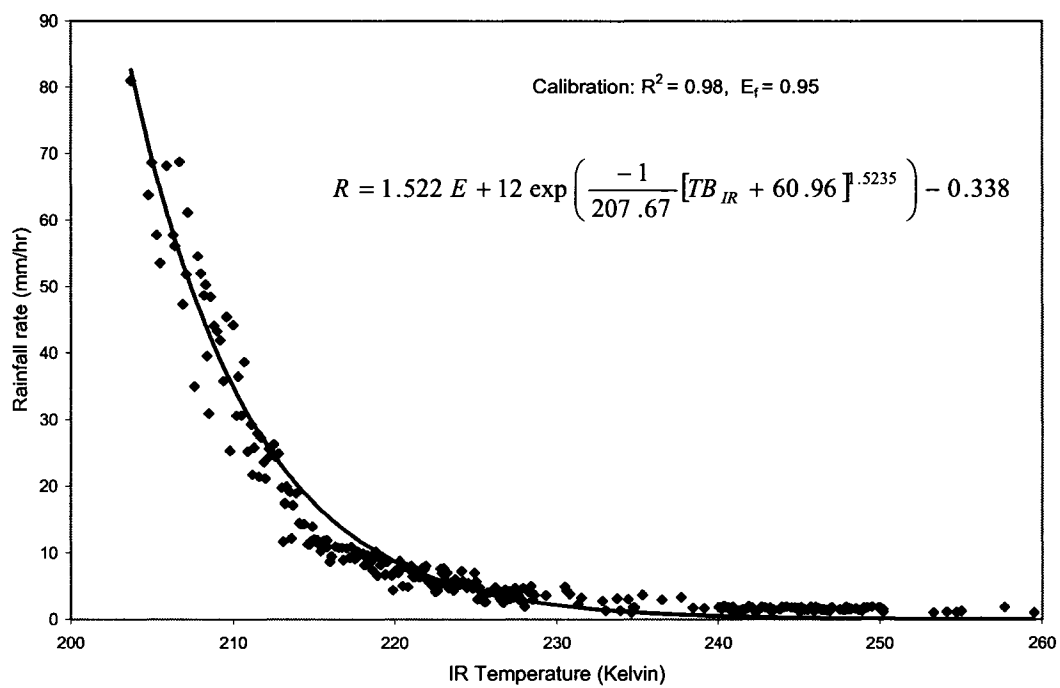


Figure 2.3 Collocated IR-Gauge rainfall data used in derivation of $R-TB_{IR}$ power law relation (shown in solid line and equation) that is used for computing IMRA rainfall estimates.

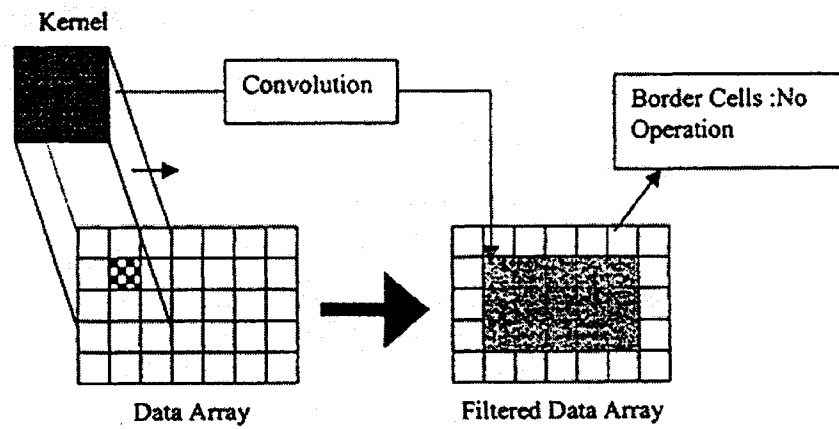


Figure 2.4 Illustration of sliding window technique (Source: Datta et al., 2003).

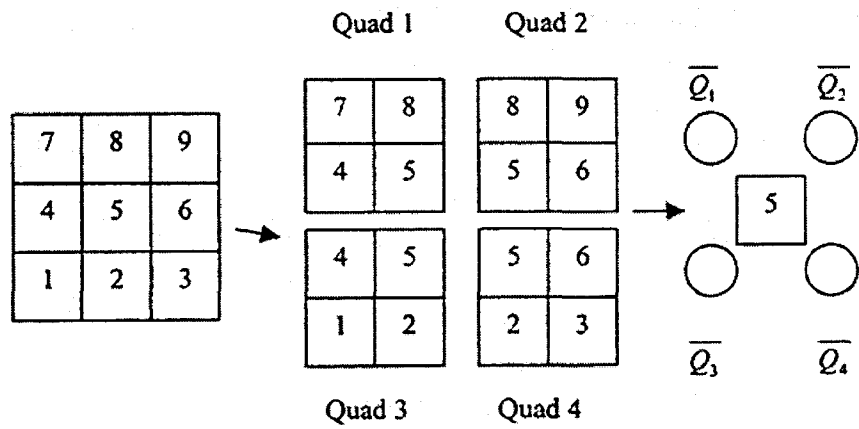


Figure 2.5 Illustration of Quad smoothing technique (Source: Datta et al., 2003).

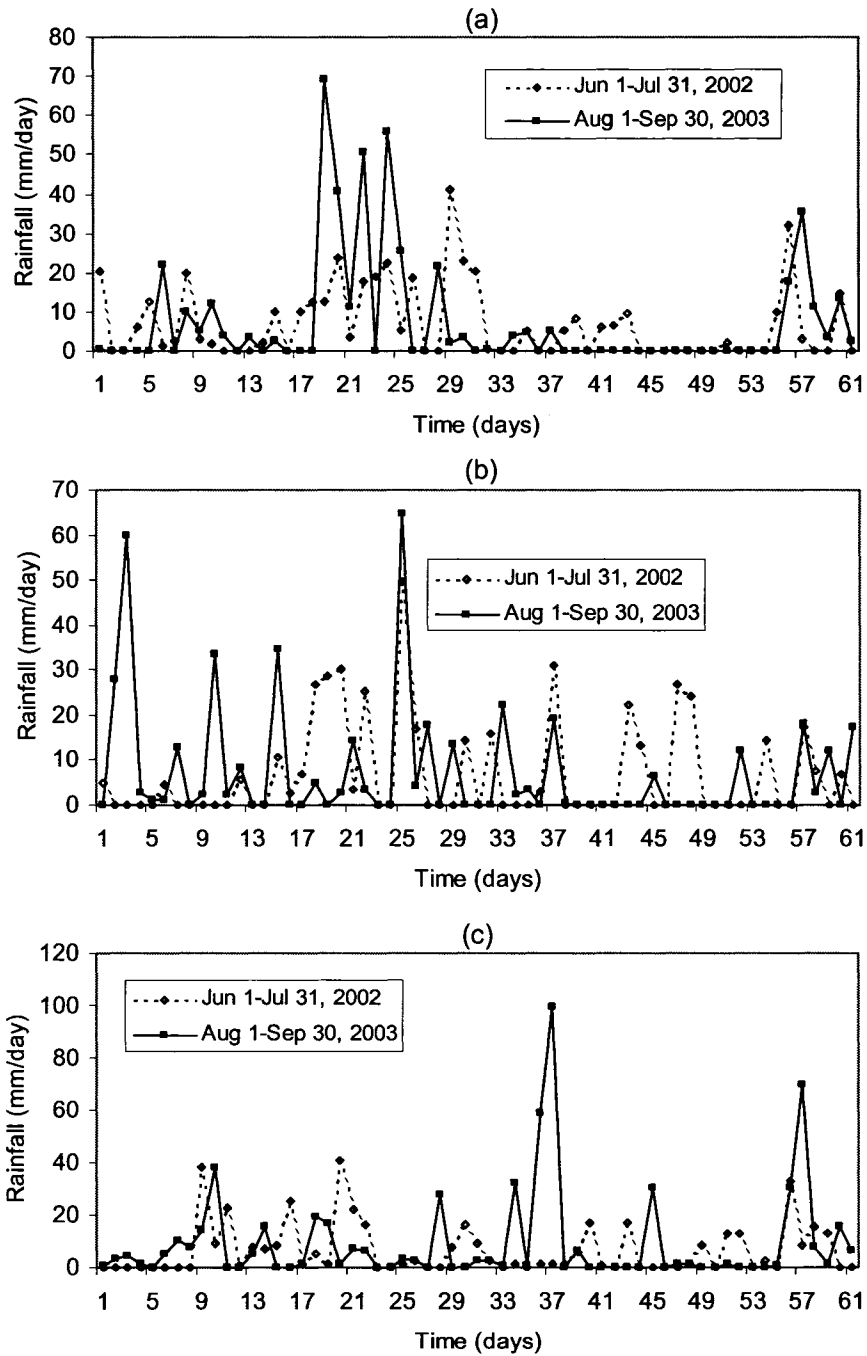


Figure 2.6 Daily time series of point gauge rainfall data showing relatively light (2002) and heavy (2003) rainfall rate at three different stations: (a) Bartow, (b) Wauchula, and (c) Punta Gorda.

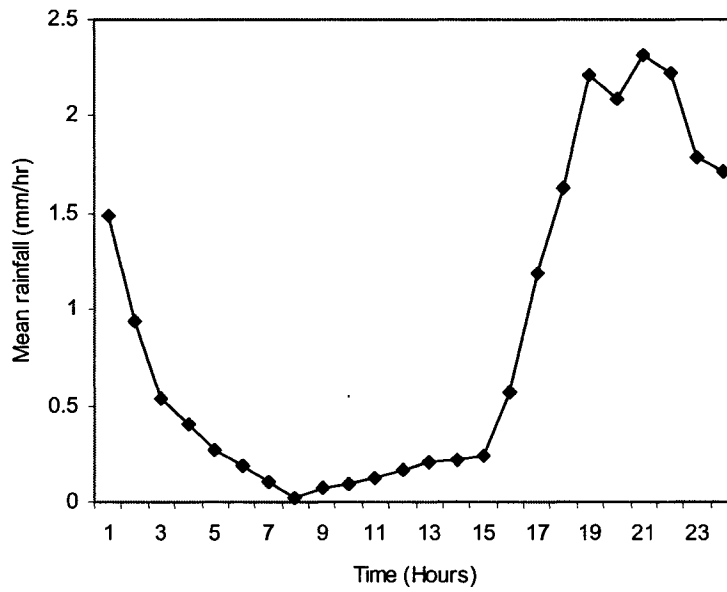


Figure 2.7 Time series of hourly mean precipitation over Peace River Basin derived from the gauge-adjusted radar rainfall data for a 31-day period of August 2003. Diurnal characteristic of the observed rainfall data is evident.

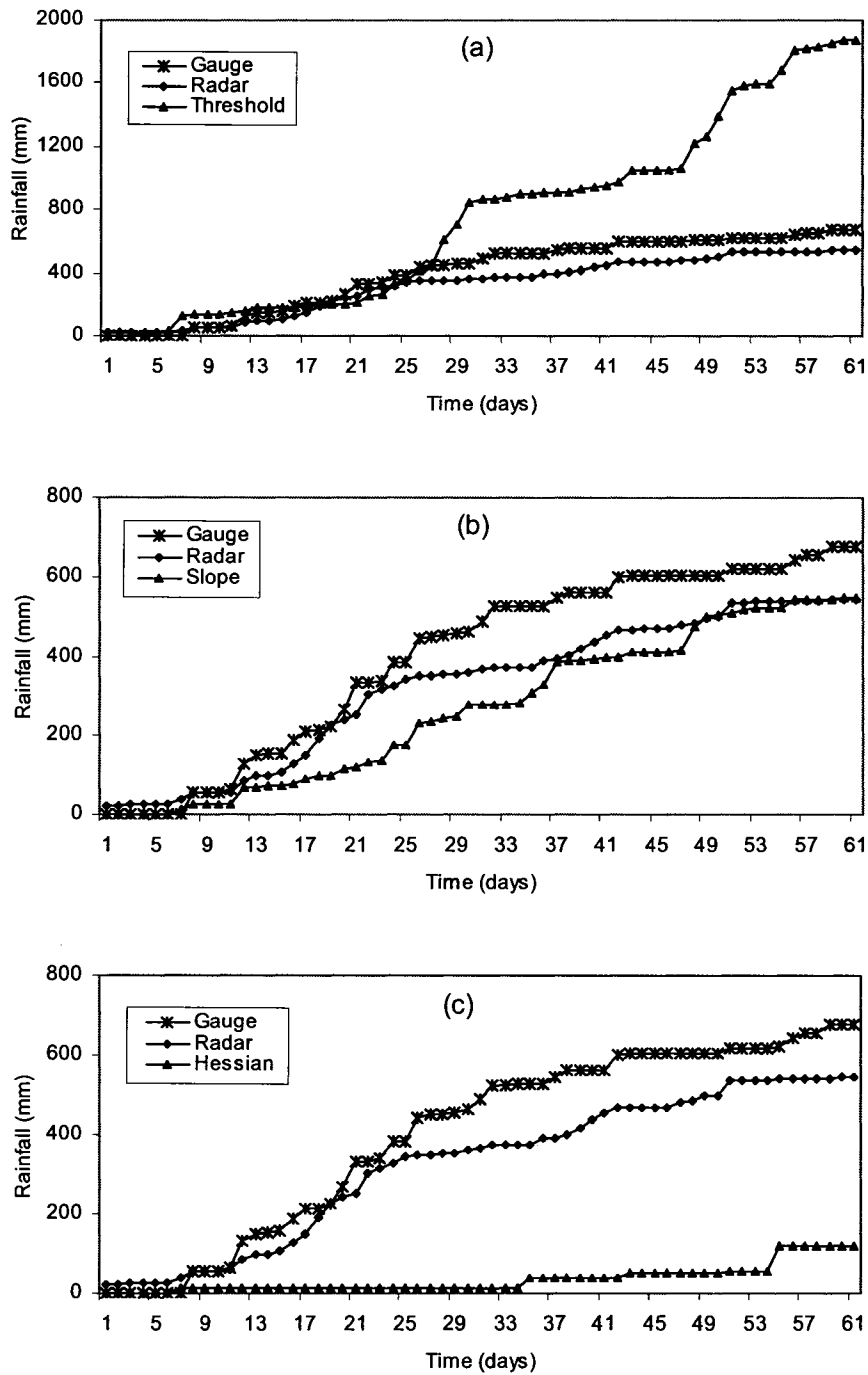


Figure 2.8 Comparison of daily cumulative satellite rainfall for 2002 dataset at Arcadia station derived by three IMRA techniques with respect to gauge and radar data.

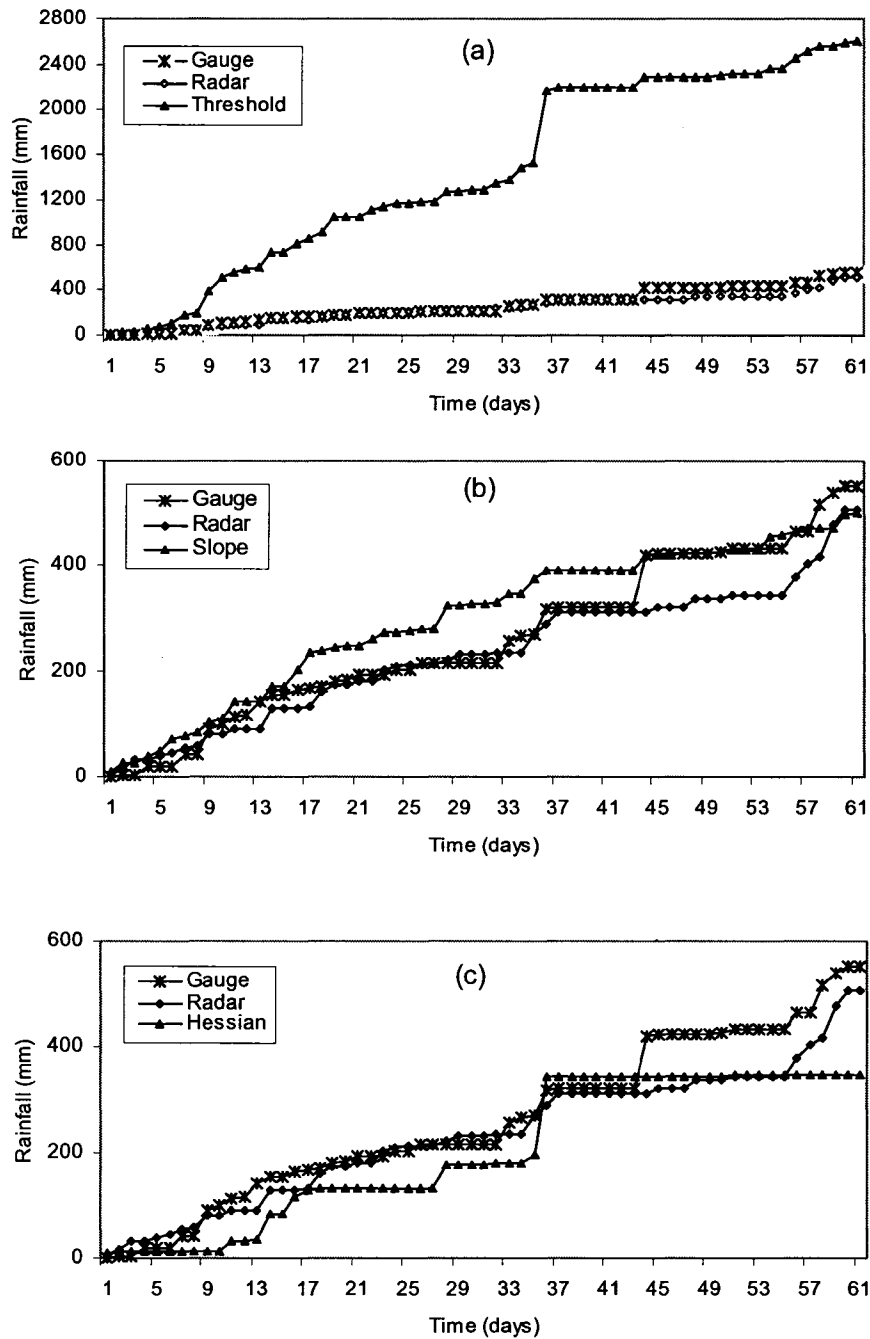


Figure 2.9 Comparison of daily cumulative satellite rainfall for 2003 dataset at Arcadia station derived by three IMRA techniques with respect to gauge and radar data.

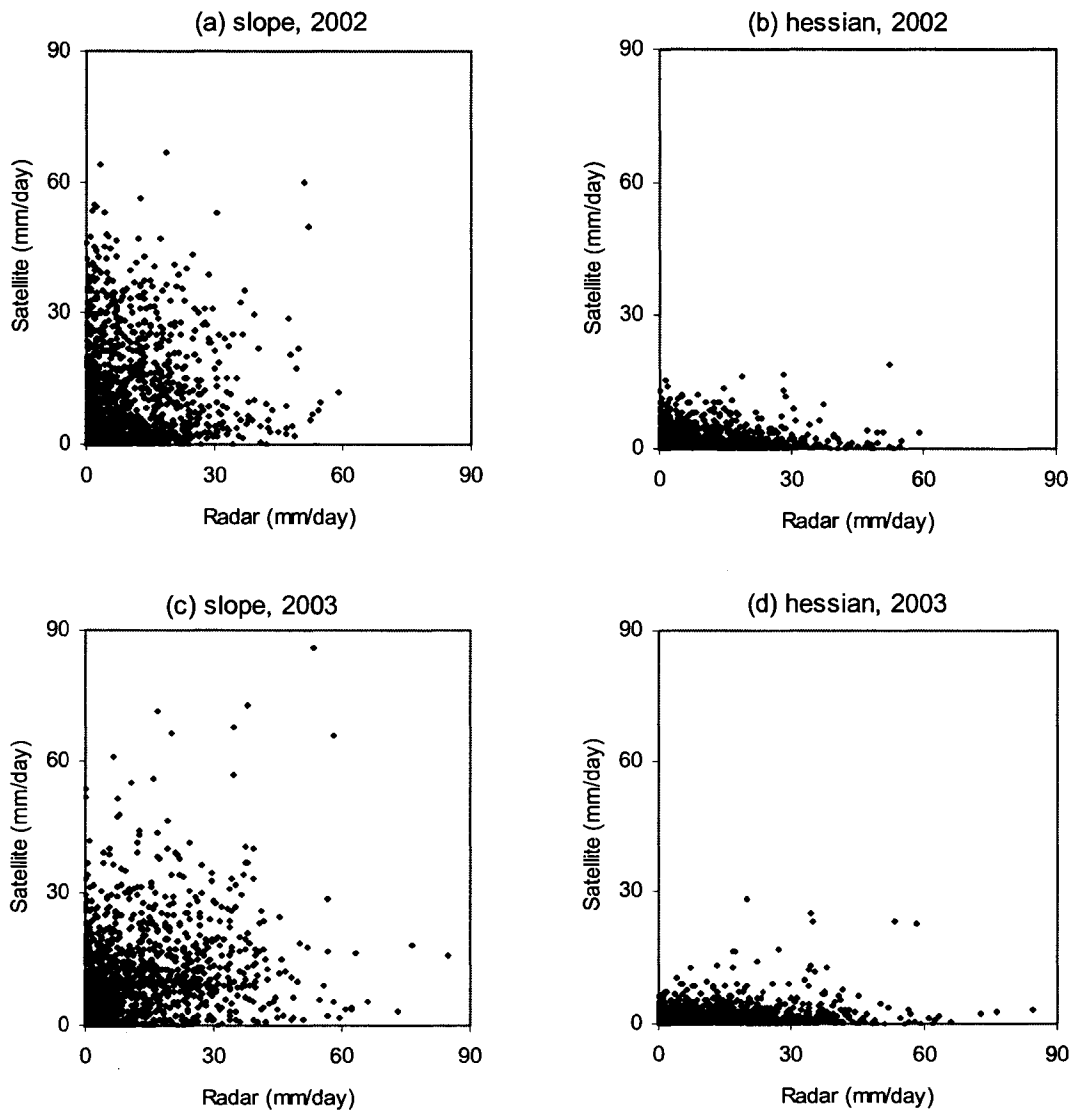


Figure 2.10 Comparison of daily rainfall rates from radar and satellite (derived by IMRA slope and hessian) for both 2002 and 2003 datasets at grid points with 20 km pixel resolution.

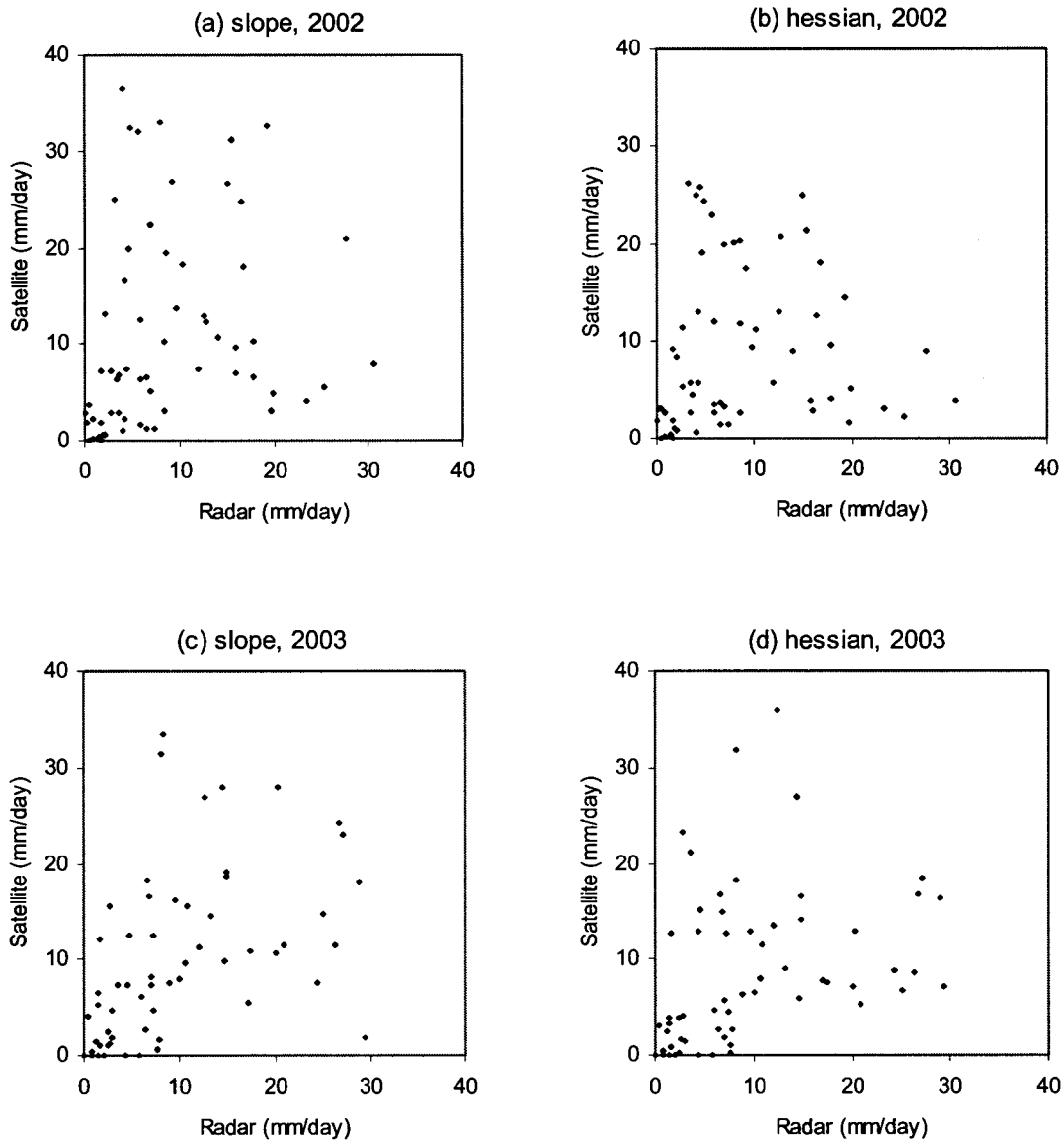


Figure 2.11 Comparison of daily rainfall rates from radar and satellite (derived by IMRA slope and hessian) for both 2002 and 2003 datasets at grid points with 100 km pixel resolution.

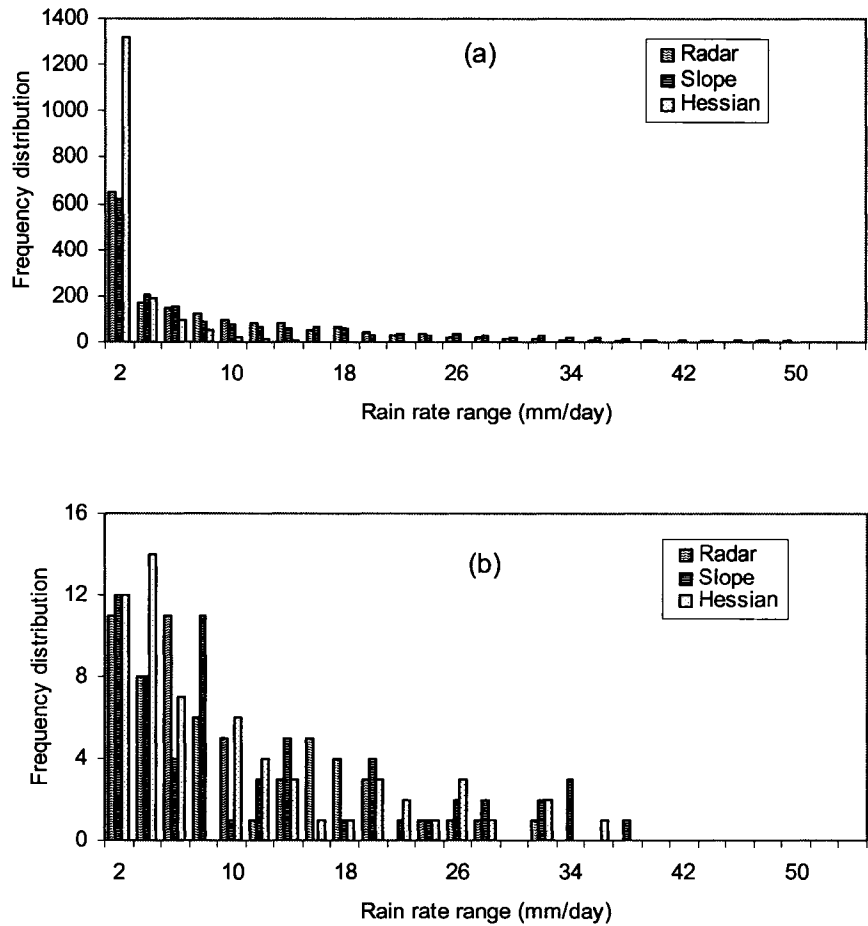


Figure 2.12 Frequency distribution of daily rainfall rate from gauge-adjusted radar and satellite estimates (from IMRA slope and hessian) for 2002 dataset at (a) 20 km grid resolution, and (b) 100 km grid resolution.

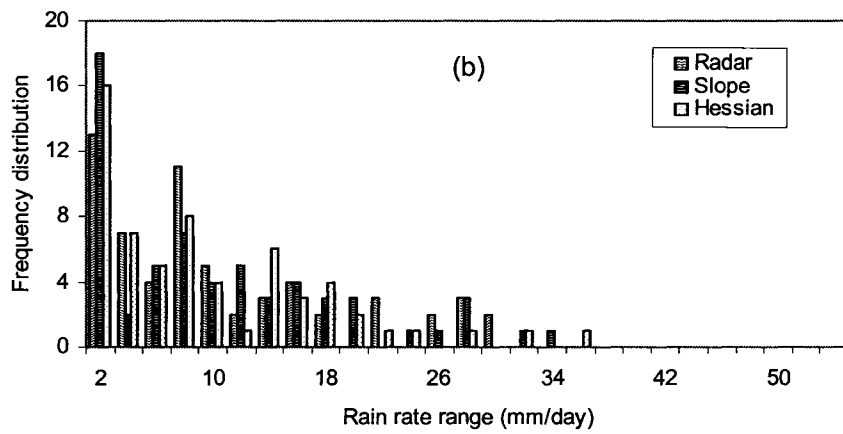
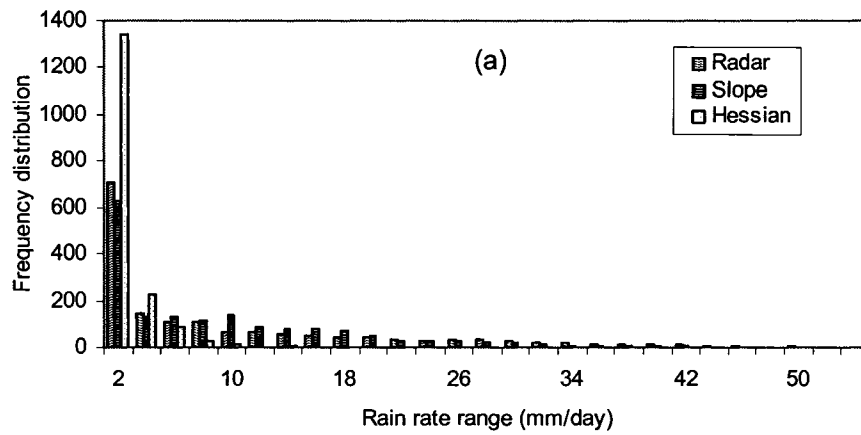


Figure 2.13 Frequency distribution of daily rainfall rate from gauge-adjusted radar and satellite estimates (from IMRA slope and hessian) for 2003 dataset at (a) 20 km grid resolution, and (b) 100 km grid resolution.

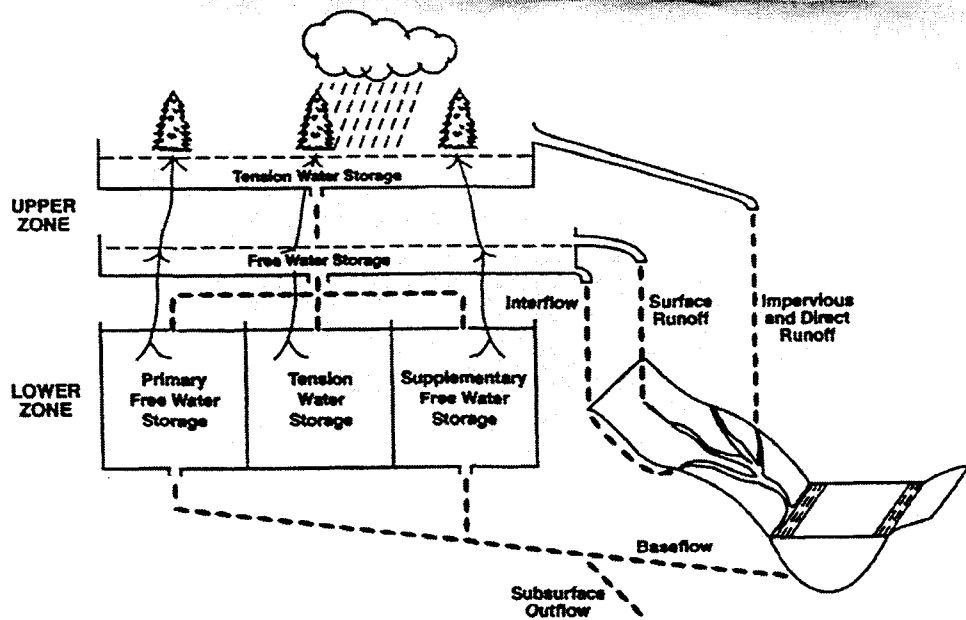


Figure 2.14 Conceptualization of the SAC-SMA model illustrating the soil moisture storages, runoff components, and land surface – atmosphere exchanges (Source: Finnerty et al., 1997).

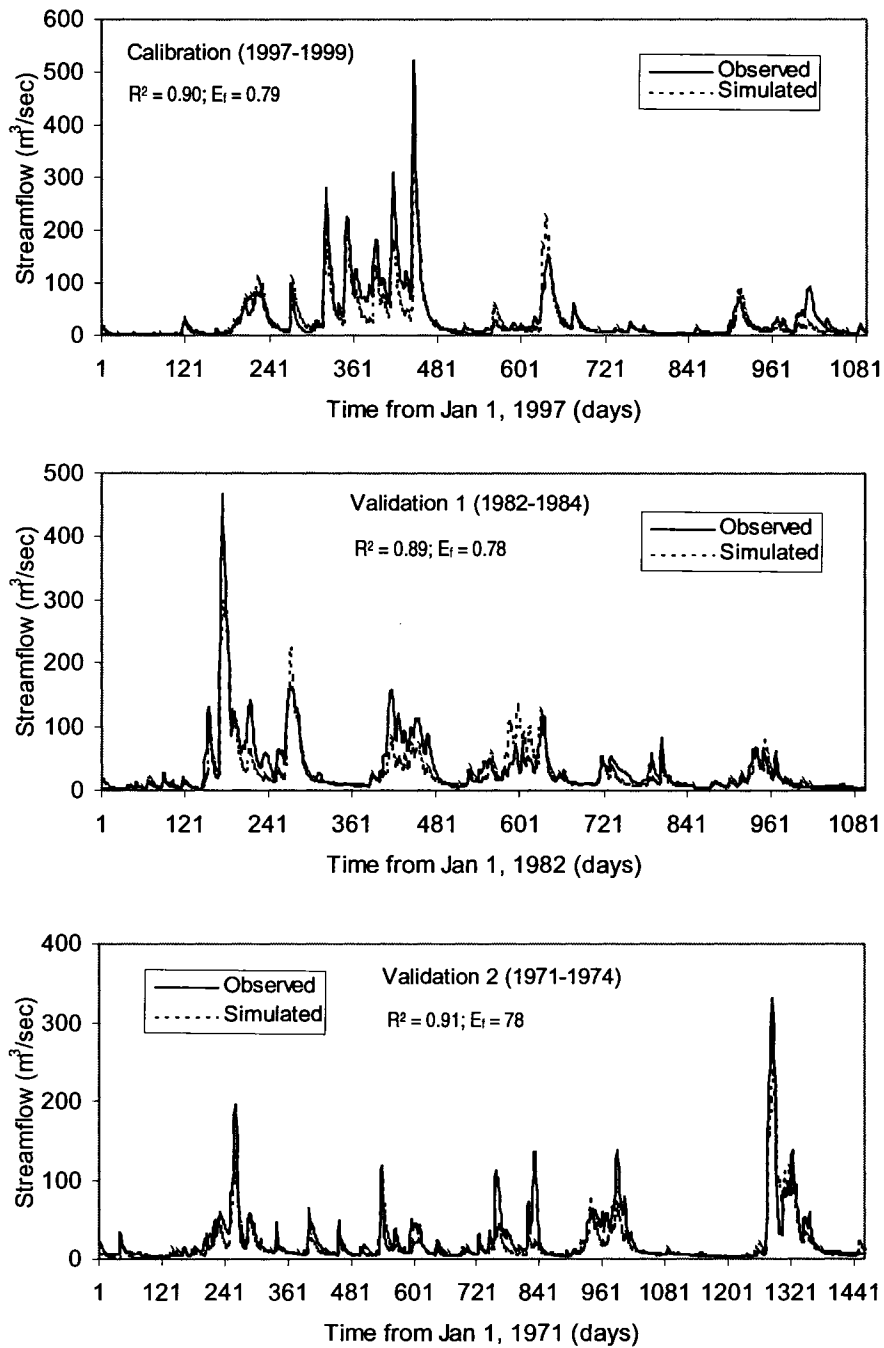


Figure 2.15 Comparison of observed and predicted streamflow hydrographs by SAC-SMA model forced with gauge rainfall data during calibration and validation periods.

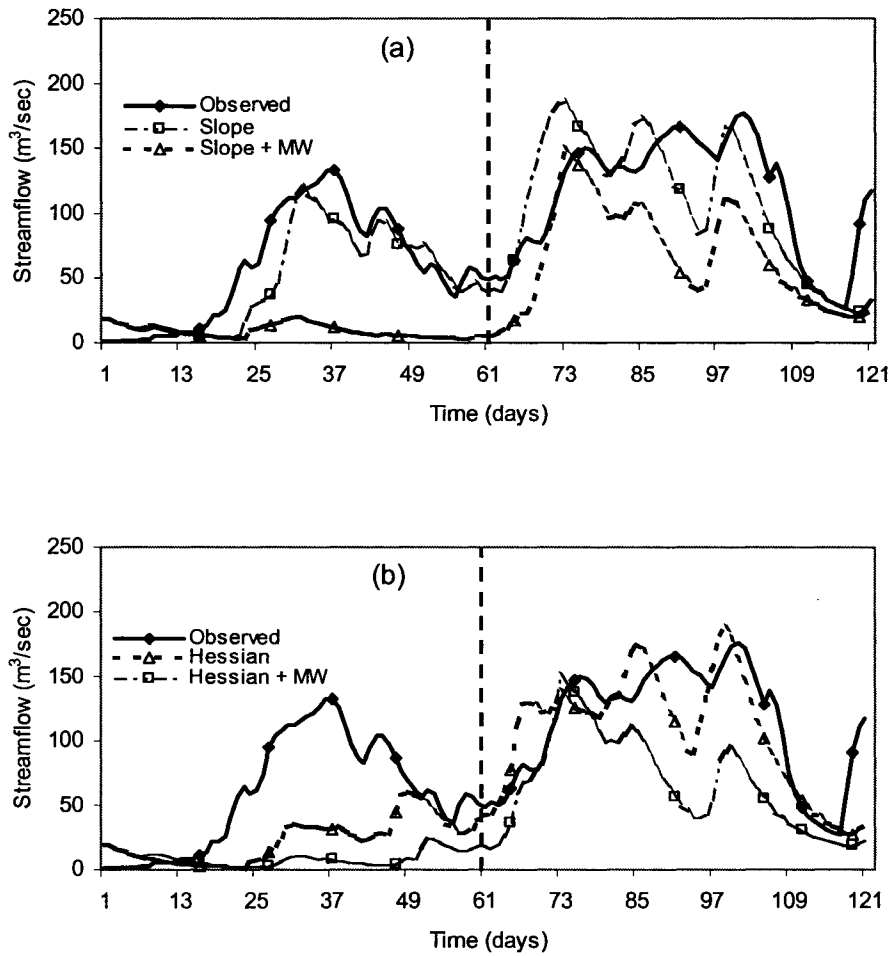


Figure 2.16 Observed and predicted streamflow hydrographs by SAC-SMA model forced with satellite rainfall estimates derived by IMRA (a) Slope and (b) Hessian with and without microwave (MW) adjustment: Left of vertical dashed line represents 2002 data (i.e., day 1-61) and the right side is for 2003 data (i.e., day 62-122).

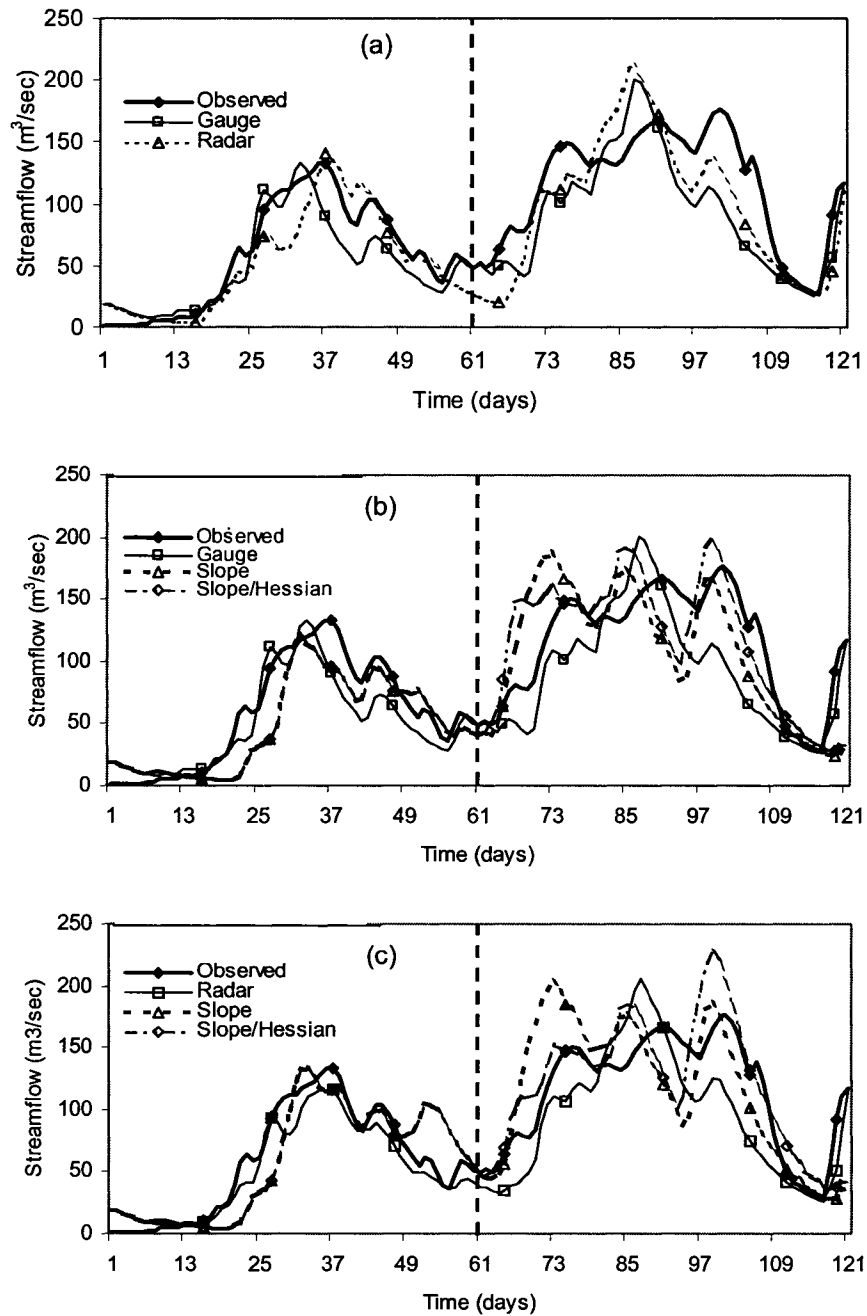


Figure 2.17 Observed and predicted streamflow hydrographs from gauge, radar, and satellite rainfall estimates for lumped basin [(a) & (b)] and 4 sub-basins case [(c)]. Note: Slope/Hessian \rightarrow Slope is used in 2002 (i.e., day 1-61) and Hessian is used in 2003 (i.e., day 62-122).

Chapter 3

Merging of Operational WSR-88D Radar Precipitation Data with Raingauge Measurements using Wavelet Analysis

3.1 Introduction

As the primary input for modeling basin hydrologic processes, it is essential that we use representative precipitation data. Since precipitation is characterized by high spatial and temporal variability, the traditional point measurements by raingauges may fail to capture the precipitation spatial distribution even at high-density raingauge networks (Datta et al., 2003). On the other hand, weather radars such as the Next generation weather radar (NEXRAD) (previously known as Weather Surveillance Radar-1988 Doppler (WSR-88D)) provide precipitation data at much better spatial and temporal sampling frequencies than raingauges (Klazura and Imy, 1993). A quantitative estimate of rainfall from radar data usually uses a power law Z - R relationship (e.g., $Z = AR^b$) between the radar reflectivity Z and the rain rate R measured at the surface (Atlas et al., 1997; Steiner et al., 1999; Datta et al., 2003). It is logical to adjust the radar-derived precipitation estimates with surface raingauges

data because, operational radar rainfall estimates rarely match the amounts recorded by raingauges due to various factors (Fulton et al., 1998; Steiner et al., 1999).

There are several sampling and scaling issues involved in adjusting radar precipitation with respect to raingauge measurements because the spatial and temporal resolution of radar and gauge differ widely. A gauged rainfall is a point measurement accumulated continuously over a sampling area of the order of 1m^2 only, while radar samples the three-dimensional rainfall field over an area of about $1\text{-}2\text{ km}^2$ and at high temporal frequencies (5-6 min). Given that rain rate can vary by a factor of say, 10 within a 2-km distance or 10-minute period (Joss and Waldvogel, 1990), such large differences in sampling areas between radar and gauge pose a major limitation for direct adjustment and comparison (Ciach and Krajewski, 1999; Datta et al., 2003). Also, there are various data quality issues for both gauge and radar observations. For raingauges, sources of errors (Legates and DeLiberty, 1993; Groisman and Legates, 1994) are such as false, multiple, or undetected tips at low rain rate associated with tipping-bucket gauges; undercatch problems because of wind effect (Neff, 1997); biological detritus and mineral particulate accumulation such as dust, blown grass and leaves, dead insects, and bird droppings, which may either clog the funnel focusing the rain catch into the tipping bucket or affect the tipping mechanism itself (Steiner et al., 1999); and mechanical and/or electrical failure of the gauge and data-logging system in the field. Despite of these problems, raingauge data are still used to evaluate and/or adjust radar rainfall (Story, 1996; Fulton et al., 1998).

For radar, data uncertainties arise from different sources, such as beam blockage caused by topography; attenuation by atmospheric gases and raindrops; effects of ground clutter and anomalous propagation; uncertainties in reflectivity measurement caused by radar hardware calibration and stability issues; inappropriate Z-R relationships; data processing problems (e.g., mosaicking errors); and radar range effects. Several studies have been conducted in an effort to quantify the effect of these uncertainties on precipitation estimates from WSR-88D or other radars using raingauges. Baeck and Smith (1998) compared WSR-88D Stage I radar rainfall with raingauge data; they reported that range-dependent biases affected the hourly radar rainfall estimates. While overestimation of precipitation occurred in the intermediate ranges, significant underestimation was reported at ranges beyond 100 km and within 40 km of the radar. Although the bias-corrected stage III WSR-88D data could be expected to compare better with the raingauge data, Anagnostou et al. (1998) reported significant variations in the mean-field bias (MFB) of radar estimates, e.g., the MFB of warm seasons was significantly less than that of cold seasons. Smith et al. (1996) and Young et al. (1999) found systematic differences between two different radars for the same area, indicating problems in radar calibration at individual radar sites. Such biases in WSR-88D estimates can adversely affect the Stage III products (Young et al., 2000).

Lott and Sittel (1996) reported a radar underestimation of precipitation up to a factor of 2 to 3 at 80% of the raingauge locations; Under abnormal humidity and temperature gradient, the radar beam bends toward the ground resulting in variable ground-clutter returns (Sharp, 1997) which contaminates the radar scene with a strong echo similar to severe weather called the anomalous propagation (AP). Sometimes birds, insects, and even dusts create false echoes. Westrick et al. (1999) and Young et al. (1999) reported degradation of WSR-88D precipitation estimates due to partial or complete beam blockage in mountainous terrain. Steiner et al. (1999) noted that even in flat terrain and under normal atmospheric conditions,

because of earth's curvature the center of the radar beam become increasingly aboveground with increasing distance from the radar site, and radar irradiates a sample volume that also increases with increasing distance due to radar beam geometry. These two factors coupled with the high spatial and temporal variability of precipitation could potentially lead to overshooting of cloud tops at long ranges, inhomogeneous beam-filling problems, observations of the ice layer above the 0°C level rather than the rain below, and intersection with the melting layer of clouds causing bright band signatures.

The variation in Z-R relationships is also a possible source of errors (Pessoa et al., 1993; Brandes et al., 1999; Steiner et al., 1999), and is attributed to variations in rainfall drop size distribution that may vary significantly from storm to storm and even within storms (Fulton et al., 1998; Steiner et al., 1999). Steiner et al. (1999) indicated that a standard choice of $Z = AR^b$ with A and b values being 300 and 1.4 respectively is a good approximate relationship. They also demonstrated the potential range of "A values" used to accommodate the variability of the raindrop size distributions for a given storm, and significant changes in the raindrop spectra during the storm that resulted into apparent shifts of the Z-R relation.

The vertical variability of reflectivity affects the quality of WSR-88D rainfall estimates by inducing range-dependent errors (Joss and Lee, 1995; Vignal and Krajewski, 2001). For convective storms, updrafts and downdrafts and raindrop sorting due to wind shear may play a significant role in creating a non-uniform vertical structure of radar echoes, while phase change of hydrometeors (i.e., from solid to liquid) is among the sources of vertical variability of reflectivity for stratiform storms (Borga et al., 1997). For the case of severe thunderstorms, radar signals may be contaminated by graupel or hail resulting in increased radar reflectivity, while a considerable attenuation in the radar signal may be associated with high precipitation intensities (Vignal and Krajewski, 2001).

There are discrepancies attributed to errors caused by averaging overlapping radar bins to produce WSR-88 stage III data; rainfall estimates near any radar site may be compromised when averaged with data from distant radar sites because the radar beam spreads out vertically and horizontally as it gets further from the radar antenna, making an accurate analysis of radar returns becoming more difficult as the range increases, particularly during cold seasons when shallow stratiform rainfall dominates (Sharp, 1997; Pereira et al., 1998; Young et al., 1999). Jayakrishnan et al. (2004) assessed the WSR-88D stage III precipitation data over the Texas-Gulf basin for 1995-1999 using 24-hour accumulations; they reported that WSR-88D radar underestimated the five-year precipitation at vast majority of the 545 raingages used in their study, and recommended that the quality of radar rainfall estimates over the study area should be assessed using raingauge measurements and necessary improvement be made before their application in hydrologic studies. Stellman et al. (2001) reported a 50% underestimation of gauge mean areal precipitation (GMAP) by WSR-88D stage III data during the cold seasons in Georgia watersheds, while a slight overestimation of GMAP was noted during the warm seasons.

The above findings on various sources of errors associated with WSR-88D precipitation estimates show the need to adjust radar rainfall using raingauge data. We evaluated the quality of stage III WSR-88D precipitation data over the Blue River Basin (BRB) of Oklahoma (USA) by storm events using hourly raingauge data of 6 Oklahoma Mesonet stations for a seven-year period; second we developed a wavelet-based technique for merging gauge and radar-derived precipitation. The

improvement achieved was assessed by comparing observed with the simulated hydrographs of the Distributed Physically-based Hydrologic Model using Remote Sensing (DPHM-RS) (Biftu and Gan, 2004).

3.2 Processing of WSR-88D Precipitation Data

The operational WSR-88D precipitation data is produced in a three-stage process (Fulton et al., 1998). The original radar reflectivities are measured by volume scans over a fixed polar grid with a radial resolution of one degree in azimuth by 1 km in range. Stage I involves producing the Hourly Digital Precipitation (HDP) from individual WSR-88Ds at a spatial resolution of about 4 km x 4 km, on a polar stereographic projection called the Hydrologic Rainfall Analysis Project (HRAP) grid (Reed and Maidment, 1999). Then, depending on the prevailing weather condition, a convective Z-R (i.e., $Z=300R^{1.4}$) or a tropical Z-R relationship (i.e., $Z=250R^{1.2}$) is used to convert the radar measured reflectivity into a radar rainfall rate, which are averaged over the HRAP grids under the individual radar umbrella, as the stage I product.

In Stage II, the mean field bias (MFB), average difference (i.e., bias) between radar estimates at gauge locations and the corresponding gauge rainfall depths is estimated for individual radars using non-zero gauge-radar pairs (minimum of three) at the gauge's nine surrounding HRAP cells. These MFB factors are meant to compensate for non-representative Z-R relationships of individual storms (Story, 1996; Steiner et al., 1999). Hourly WSR-88D precipitation data are adjusted using the computed MFB factor for the respective hour over the entire radar coverage area until a new set of gauge-radar pairs is obtained. In the absence of at least three gauge-radar pairs for a given hour, the previous hour MFB is applied to the whole coverage. If radar data shows rainfall over a gauge that reports zero, the respective HRAP bin will be assigned a zero. On the other hand, if a gauge reports rainfall for a given hour while the radar data are missing, a maximum value at the gauge's site

is assigned to all HRAP cells falling under the gauge's radius of influence, which is typically 2 to 3 HRAP bins.

In stage III, any erroneous gauge or radar data due to anomalous propagation, ground clutter, or bright banding is removed, followed by averaging of the individual stage II products from the respective overlapping WSR-88Ds within the area of coverage into a single map of hourly, operational WSR-88D stage III rainfall product. This process is called mosaicking, and it is meant to compensate for the under or over-estimation of precipitation by a particular radar using better estimates of data from overlapping radars (Story, 1996). However, some studies have reported this simple averaging of overlapping radar precipitation values to be the source of radar's underestimation of rainfall especially during the cold season normally dominated by stratiform storms (e.g., Pereira et al. 1998, Stellman et al. 2001). Klazura and Imy (1993), Smith et al. (1996), and Fulton et al. (1998) provide more details on the WSR-88D products and processing algorithms.

3.3 Study Site and Data Processing

3.3.1 Blue River Basin (BRB)

The BRB, located in South Central Oklahoma (USA) (Figure 3.1a), was selected as the study site mainly because BRB is not regulated and both the operational WSR-88D stage III rainfall data and the Oklahoma Mesonet data, which is a real-time environmental monitoring network, are readily available. This region is dominated by frontal precipitation associated with large, synoptic scale low-pressure systems during fall and winter, with intense convective activity during spring and early summer. Rainfall is uniformly distributed throughout the year with a slight maximum during the spring. The average annual precipitation ranges from about 400mm in the extreme western panhandle to 1420mm in the southeastern corner of the State (Frederick et al., 1977). The basin, 1233 km² in area, has a relatively flat terrain with elevation ranging from 153 to 350m above mean sea level, and the

major soil groups are clay and loam mixed with sand or silt. Woody Savannah is the dominant vegetation occupying almost 80% of basin.

The basin is divided into 7 sub-basins (Fig. 1b) according to the digital elevation map (DEM) data, with the original 30-m cell re-sampled to 100-m in size, and stream network. DEM data was also used to derive the slope, flow direction, flow accumulation, mean elevation, and topographic soil index at 100m square resolutions. Soil properties such as the saturated hydraulic conductivity, pore size index, suction head at saturation, and saturation water content were derived from the soil texture data (1-km resolution) and soil properties table of Rawls and Brankensiek (1985). The land use/cover data were derived from the vegetation data (1-Km resolution) of NASA LDAS (Land Data Assimilation Systems) and the leaf area index (LAI) was derived from the monthly Greenness Fraction data (~12-Km resolution) of NOAA-AVHRR data.

3.3.2 Rainfall and Streamflow Data

The 1994-2000 WSR-88D stage III radar rainfall data at 1-hour and 4x4 km resolution were obtained from the National Weather Service (NWS) through the Distributed Model Intercomparison Project (DMIP). The BRB is within the Arkansas-Red Basin River Forecast Center (ABRFC) and five WSR-88Ds located in Oklahoma, Texas, and Arkansas provided the coverage (Figure 3.1a). The hourly gauge rainfall data were processed from 6 Oklahoma Mesonet stations located around the basin (see Fig. 3.1b), and that uses tipping bucket gauges to measure rainfall accumulation at 5-min intervals. The final data are accumulated to hourly time step. The average distance between the raingauge stations is about 30 km.

The hourly observed streamflow data at the basin outlet (Fig. 3.1b), obtained from the U.S. Geological Survey, have been quality controlled (but no interpolation) by the NWS Hydrologic Laboratory based on a manual and subjective process

accomplished through visual inspection of observed hydrographs. The streamflow data used in this study had no missing data gaps.

3.3.3 Data Processing

The WSR-88D stage III precipitation data from DMIP were provided for the entire ABRFC region. Using GIS Arc/Info, each hourly rainfall map was clipped to a 32 x 32 pixels window at 4 km x 4 km pixel resolution covering the BRB and its proximity. Then using GIS ArcView, the raingauge locations were overlaid on the radar grid map to determine the radar grid points closest to each of the six raingauges. The corresponding grid point hourly WSR-88D stage III precipitation data for each raingauge location were extracted from the grip map, and together with the hourly raingauge data they formed a database for accuracy assessment of WSR-88D stage III precipitation data. A total of 89 storms were selected from 1994 to 2000 to assess the accuracy of WSR-88D data (Table 3.1). To ensure that the selected storms covered the entire BRB and to avoid smaller storms that are prone to measurement errors by both radar and gauges (Groisman and Legates, 1994; Smith et al., 1996), the selection criteria required that at least three consecutive hours of rainfall were recorded at each raingauge location, and the corresponding total storm depth was at least 10 mm. The number of selected storms per year ranged from 9 to 15 while the storm durations ranged from 3 to 43 hours (see Table 3.1). During 1994-2000, the total storm depth at individual raingauge ranged from 10 mm to about 160 mm while the storm average depth over the six raingauges varied from about 13 mm to 86 mm.

3.4 Accuracy of WSR-88D Stage III Precipitation Data

The accuracy of WSR-88D rainfall data was assessed on a storm-by-storm and annual basis with respect to gauged data for the 1994-2000 period. The Oklahoma Mesonet stations are a real-time environmental monitoring network equipped with sound instruments and trained personnel and hence are deemed to provide reliable

gauged rainfall data. However, at times the quality of raingauge data can still be poor even in an experimental watershed (Steiner et al., 1999). The following statistics were employed: (a) Total precipitation difference (mm) = Radar total – Raingauge total, with the total storm depth taken as the average over the six raingauge locations for individual storms analysis (Table 3.1), (b) Bias (%) = a % ratio of total precipitation difference to raingauge total, (c) Efficiency coefficient (E_f) of Nash and Sutcliffe (1970), and (d) Root Mean Square Error (RMSE).

The radar-gauge data comparison shows that, the average raingauge storm depth was larger than the average WSR-88D stage III rainfall amount at the gauge locations in 92% of the storms in 1994, and 83%, 67%, 67%, 33%, 44%, and 46% of the storms for 1995 to 2000, respectively. In other words, for years greater than 50%, radar estimated the total storm depths proportionally less than gauged rainfall data (Table 3.1). Generally there is an improvement in the performance of the WSR-88D over the years, with the underestimation of radar rainfall for 1998-2000 being significantly lower than that of 1994-1997. The significant reduction in radar underestimation errors is attributed to the on-going improvements being made to the WSR-88D precipitation processing algorithms by the NWS (Jayakrishnan et al., 2004).

A closer look at Table 3.1 shows that, the number of storms underestimated by radar for the cold season (September to February) normally dominated by stratiform storms was generally larger than the number of storms underestimated during the warm season (March to August) normally dominated by convective storms. The number of storms underestimated by radar for the cold season (warm season) was 100% (83%), 100% (78%), 67% (67%), 73% (50%), 27% (50%), 67% (33%), and 25% (80%) for the years 1994 to 2000, respectively. This shows that, with the exception of 1998 and 2000, the radar's underestimation of stratiform storms was larger than or equal to the corresponding underestimation of convective storms during the 7-year period, and is consistent with the findings of Stellman et al. (2001)

who also reported that radar underestimated stratiform storms but slightly overestimated convective storms.

We further compared the radar-gauge data for the largest (1994) and the smallest (1998) year of radar's underestimation of gauged measurements. In this case, all storms in a given year were combined to produce an hourly time series, and the total number of hours were 231 and 213 for 1994 and 1998 respectively. The results in Table 3.2 indicate that in 1994, raingauges 1 and 6 represented the largest radar's underestimation with a bias of -13.89% and -14.26% and an efficiency coefficient (E_f) of 0.82 and 0.58 respectively. Although the bias was more or less equal, there was a substantial difference in the E_f values. Similar results are seen for 1998 at raingauges 2 and 6 when radar overestimated the precipitation (Table 3.2). Jayakrishnan et al. (2004) noted that such differences in the two statistics are attributed to fact that, in estimating bias over the entire period (e.g., 1 year herein) over-estimated storm depths average out the under-estimated storm depths, while E_f considers goodness-of-fit on a data point by data point basis. The scatterplots in Figures 3.2 and 3.3 shows that poor E_f is associated with poor correlation between radar and gauge rainfall measurement regardless of the size of estimated bias and vice versa. The average bias for the six raingauges for 1994 and 1998 are -8.29% and 4.83%, respectively, which suggests that the radar's underestimation of rainfall is more critical than its overestimation (Stellman et al., 2001). Such large differences between both rainfall data sources imply significant differences in results if these data were separately applied to basin-scale hydrologic studies.

3.5 Merging Radar and Gauged Rainfall Data

Because operational radar rainfall data have uncertainties, and the major concern is the underestimation of rainfall, Pereira et al. (1998), Stellman et al. (2001), and Jayakrishnan et al. (2004) proposed to quantify and correct the uncertainties associated with the radar-derived precipitation data before applying them in

hydrologic studies. The correction of radar-derived rainfall can be categorized into two basic approaches (Sokol, 2003): The first is based on the identification and correction of vertical profiles of reflectivity (VPR). By assuming a spatial uniformity of the VPR, the data within few tens of kilometers from the radar position are utilized and the derived VPR is applied to correct data from longer ranges (e.g., Borga et al., 1997). The second approach is based on gauge-to-radar statistical adjustment techniques to adjust radar-derived rainfall to the quantitative level of gauge measurements. The second approach may either use gauged precipitation to derive the model parameters used to correct the radar data (e.g., Gabella and Amitai, 2000), or merge both data sets at each application (e.g., Pereira et al., 1998). The raingauge adjustment methods attempt to deal with the primary sources of radar errors in a single process, but mostly suffer from the limited spatial representation of gauge measurements because the number of raingauges available is limited and they only provide point measurements.

Pereira et al. (1998) developed a Statistical Objective Analysis (SOA) scheme for improving WSR-88D stage III rainfall data, which will be compared with the proposed wavelet analysis in merging gauge and radar-derived precipitation. From what we know, this is one of the first attempts using wavelet analysis in merging radar and gauged rainfall data. It exploits the strength of radar data that captures the spatial variability of rainfall and the strength of raingauges that generally measure accurate mean rainfall depths. The two merging techniques are herein described:

3.5.1 Statistical Objective Analysis (SOA) Scheme

SOA, proposed by Pereira et al. (1998) to merge radar and raingauge rainfall data, is based on one of the best techniques for interpolating precipitation data, Gandin's (1963) optimal interpolation (Tabios and Salas, 1985). The merged rainfall data at a particular grid point is computed as a linear combination of radar and raingauge rainfall data from three nearby raingauge stations (i.e., $N = 3$) as,

$$R_m(x_p, y_p) = R_r(x_p, y_p) + \sum_{n=1}^N w_{pn} [R_g(x_n, y_n) - R_r(x_n, y_n)] \quad (3.1)$$

where $R_m(x_p, y_p)$ is the merged rainfall (mm) at grid point p , $R_r(x_p, y_p)$ is radar estimated rainfall (mm) at grid point p , $R_r(x_n, y_n)$ is radar estimated rainfall (mm) with its grid point closest to raingauge station n , $R_g(x_n, y_n)$ is gauge rainfall measurement (mm) at station n , w_{pn} is a posteriori weight, N is the number of raingauges, and (x, y) are the coordinates (km). The second term on the RHS of Eq. 3.1 is meant to correct for the under-estimation of rainfall depth by radar data, $R_r(x_p, y_p)$, with respect to gauge measurements.

The key idea behind SOA is the derivation of optimal weights (w_{pn}) using an inter-site correlation function. In this study, three such functions, namely, reciprocal, exponential, and polynomial (Table 3.3) were fitted to the inter-site correlation coefficients computed between radar grid points from the 1994-1997 radar rainfall data. The three calibrated correlation functions were then validated with the inter-site correlation coefficients computed from the 1998-2000 radar rainfall data. Figure 3.4 shows that the polynomial function produced a better fit (higher efficiency (E_f)) than the exponential and reciprocal functions. Thus, the polynomial spatial correlation function was used in computing the weights w_{pn} .

3.5.2 Wavelet Scheme

In this scheme, for each hourly time step: (a) the two rainfall data sets (radar and gauge) are re-sampled to a similar spatial resolution, i.e., the six stations' gauged data (see Figure 3.1b) were interpolated to radar's grid points; (b) a forward wavelet transform is employed to decompose the original data set into subsets of coarser resolutions creating one average and three gradients data sets for each data source at

each scale; (c) a merging rule is applied to select which decomposed data sets to merge; and (d) an inverse wavelet transform is applied to the selected fields to generate the final product (see Figure 3.5).

3.5.2.1 Wavelet Analysis

A continuous process, $R(x)$, can be decomposed to a coarser scale λ by applying two filters, the scaling $\phi_{\lambda,u}(x)$ and the wavelet $\psi_{\lambda,u}(x)$ functions for “averaging” and “differencing” respectively, where u is a location parameter. Filters $\phi_{\lambda,u}(x)$ and $\psi_{\lambda,u}(x)$ are complementary to each other, implying that whatever information is lost by applying $\phi_{\lambda,u}(x)$ on the process is re-captured by applying $\psi_{\lambda,u}(x)$ on the same process at the same scale. Discrete Wavelet Transforms (DWTs) are usually employed in implementing the wavelet transform on sampled processes, such as rainfall. DWTs are obtained by discretizing the scale parameters in dyadic form, $\lambda = 2^m$ (i.e., 2^{-m} samples per unit length) and location parameters as multiples of the sampling intervals $u = n2^m$ (convenient for orthogonal wavelets). The parameters m and n are related to scale and location, respectively.

A separable, two-dimensional, multi-resolution framework (Mallat, 1989) can be used to extend the formulation to a two dimensional process, $R(x, y)$, where the scaling function is $\Phi(x, y) = \phi(x)\phi(y)$ and the three wavelet functions are $\Psi^1(x, y) = \phi(x)\psi(y)$, $\Psi^2(x, y) = \psi(x)\phi(y)$, and $\Psi^3(x, y) = \psi(x)\psi(y)$. Therefore, the discrete local average at scale m and location (n, k) is represented as

$$\bar{R}_{n,k}^m = \left\langle R, \Phi_{m,n,k} \right\rangle_{(n,k) \in Z^2} = \frac{1}{2} \sum_{i,j \in Z} R_{i,j} F_{\phi(i-2n)} F_{\phi(j-2k)} \quad (3.2)$$

and the corresponding three wavelet coefficients at the same scale and location are expressed as

$$R'_{n,k}{}^{m,1} = \left\{ \left\langle R, \Psi^1_{m,n,k} \right\rangle_{(n,k) \in Z^2} \right\} = \frac{1}{2} \sum_{i,j \in Z} R_{i,j} F_{\phi(i-2n)} F_{\psi(j-2k)} \quad (3.3)$$

$$R'_{n,k}{}^{m,2} = \left\{ \left\langle R, \Psi^2_{m,n,k} \right\rangle_{(n,k) \in Z^2} \right\} = \frac{1}{2} \sum_{i,j \in Z} R_{i,j} F_{\psi(i-2n)} F_{\phi(j-2k)} \quad (3.4)$$

$$R'_{n,k}{}^{m,3} = \left\{ \left\langle R, \Psi^3_{m,n,k} \right\rangle_{(n,k) \in Z^2} \right\} = \frac{1}{2} \sum_{i,j \in Z} R_{i,j} F_{\psi(i-2n)} F_{\psi(j-2k)} \quad (3.5)$$

where $\langle p, q \rangle$ and Z denote the inner product and set of integer numbers respectively. The three wavelet coefficients provide the directional information about the rainfall storm in horizontal (x), vertical (y), and diagonal directions, respectively. The formula used to reconstruct the original process $R(x, y) (\equiv R \equiv R_{i,j})$ from the decomposed fields is,

$$R_{i,j} = \frac{1}{2} \left(\sum_{n,k \in Z} \bar{R}_{n,k}^m \tilde{F}_{\phi(2n-i)} \tilde{F}_{\phi(2k-j)} + \sum_{n,k \in Z} R'_{n,k}{}^{m,1} \tilde{F}_{\phi(2n-i)} \tilde{F}_{\psi(2k-j)} \right. \\ \left. + \sum_{n,k \in Z} R'_{n,k}{}^{m,2} \tilde{F}_{\psi(2n-i)} \tilde{F}_{\phi(2k-j)} + \sum_{n,k \in Z} R'_{n,k}{}^{m,3} \tilde{F}_{\psi(2n-i)} \tilde{F}_{\psi(2k-j)} \right) \quad (3.6)$$

where \tilde{F}_{ϕ} and \tilde{F}_{ψ} are inverse of F_{ϕ} and F_{ψ} respectively.

3.5.2.2 Intuitive Description of Mallat Algorithm

Let $\bar{R}_m(i, j)$ be a discrete local average value at scale m and location (i, j) of the two-dimensional spatially continuous process, $R(x, y)$. For instance, if the relative scale m corresponds to the radar rainfall data resolution (4 x 4 km), $m + 1$ relates to the next higher physical scale (8 x 8 km) with spatial position indices defined by (n, k) (see Figure 3.6). Note that the number of grid points is reduced by a factor of 2 in each direction at the next scale, and that the increase in physical scale is dyadic for convenience in implementing the discrete multi-resolution algorithm.

Applying the 2-D orthogonal filters (Φ, Ψ^1, Ψ^2 , and Ψ^3) to the discrete field $\bar{R}_m(i, j)$ produces an average field $\bar{R}_{m+1}(n, k)$ and three directional “gradient” fields $\{R'_{m+1,i}(n, k)\}_{i=1,2,3}$, at the next higher scale ($m+1$). In the next scale ($m+2$), the previous scale’s average field is further decomposed into an average and three directional gradient fields, and so on. If Haar wavelet is chosen for decomposition (e.g., Kumar and Foufoula-Georgiou, 1993), the average process at scale $m+1$ is represented as

$$\bar{R}_{m+1}(n, k) = \frac{1}{4} [\bar{R}_m(i, j) + \bar{R}_m(i+1, j) + \bar{R}_m(i, j+1) + \bar{R}_m(i+1, j+1)] \quad (3.7)$$

and the corresponding three gradient components as

$$\begin{aligned} R'_{m+1,1}(n, k) &= \frac{1}{4} \left[\{\bar{R}_m(i, j) + \bar{R}_m(i, j+1)\} - \{\bar{R}_m(i+1, j) + \bar{R}_m(i+1, j+1)\} \right] \\ R'_{m+1,2}(n, k) &= \frac{1}{4} \left[\{\bar{R}_m(i, j) + \bar{R}_m(i+1, j)\} - \{\bar{R}_m(i, j+1) + \bar{R}_m(i+1, j+1)\} \right] \\ R'_{m+1,3}(n, k) &= \frac{1}{4} \left[\{\bar{R}_m(i, j) + \bar{R}_m(i+1, j+1)\} - \{\bar{R}_m(i, j+1) + \bar{R}_m(i+1, j)\} \right] \end{aligned} \quad (3.8)$$

$\bar{R}_{m+1}(n, k)$ is the 2-D average of the rainfall process from the previous scale, where $\{R'_{m+1,i}\}_{i=1,2,3}$ represent gradients of the previous-scale average process. Therefore, these rainfall gradients can be easily interpreted as discrete representations of $\partial \bar{R}_m(i, j) / \partial x$, $\partial \bar{R}_m(i, j) / \partial y$, and $\partial^2 \bar{R}_m(i, j) / \partial x \partial y$, and hence, they correspond to a scheme widely used for defining gradients of 2-D processes (Perica and Foufoula-Georgiou, 1996). Because of its simplicity and the appealing physical interpretation of the wavelet coefficients as directional gradients of the rainfall fields, the Haar wavelet was selected as the analyzing wavelet in this study. Further, Haar wavelets provide an adequate description of the spatial behavior of rainfall fields (Kumar and Foufoula-Georgiou, 1993; Perica and Foufoula-Georgiou, 1996).

3.5.2.3 Interpolation of Raingauge Data

Implementing the wavelet scheme requires that the rainfall fields from radar and gauge be at similar spatial and temporal resolution. But, the gauge-measured precipitation exists as point measurements. Thus, gridded rainfall fields for gauges must be inferred from neighboring stations through an interpolation technique. Possible techniques used for this purpose range from statistical methods (e.g., Tabios and Salas 1985, Pereira et al. 1998), distance weighting (Stellman et al., 2001), to multiple linear regressions (e.g., Marquinez et al., 2003; Sokol, 2003). The interpolation technique selected herein is based on the Statistical Objective Analysis (SOA) scheme of Pereira et al. (1998) described in Section 3.5.1. The interpolation process is accomplished in 3 steps: (a) A first pass of the Barnes analysis scheme (Kochi et al., 1983) is used to create a first-guess interpolated field $G_b(x_p, y_p)$ using all available rain gauge stations (in this case 6 stations, i.e. $K = 6$) as follows,

$$G_b(x_p, y_p) = \frac{\sum_{k=1}^K G_o(x_k, y_k) * w_{pk}}{\sum_{k=1}^K w_{pk}} \quad (3.9)$$

where the weights (w_{pk}) are computed as $w_{pk} = e^{-d_{pk}^2/k_o}$ in which d_{pk} is the distance between k^{th} raingauge station and p^{th} grid point (km), k_o is the distance constant equal to 1924.72 km² for Mesonet stations (Pereira et al., 1996), and $G_o(x_k, y_k)$ is the original gauge rainfall measurement at station k ; (b) A back interpolation pass of Barnes scheme is used to back interpolate the four grid points of the first-guess field [$G_b(x_p, y_p)$] surrounding the k^{th} gauge station (Figure 3.6), giving its predicted values, $G_p(x_k, y_k)$ as,

$$G_p(x_k, y_k) = c_1 G_b(i, j) + c_2 G_b(i+1, j) + c_3 G_b(i+1, j+1) + c_4 G_b(i, j+1) \quad (3.10)$$

where c_1 , c_2 , c_3 , and c_4 are the weights computed from the ratio of distances between the k^{th} gauge station and the four surrounding grid points (see Figure 3.6). (c) The “error” between the original gauge data value $G_o(x_k, y_k)$ and its predicted value $G_p(x_k, y_k)$ is used in the final pass to correct the first-guess field $G_b(x_p, y_p)$ through SOA to produce the final interpolated field, $G_f(x_p, y_p)$, as the average rainfall for a particular pixel,

$$G_f(x_p, y_p) = G_b(x_p, y_p) + \sum_{n=1}^N w_{pn} [G_o(x_n, y_n) - G_p(x_n, y_n)] \quad (3.11)$$

using only three rain gauge stations (i.e., $N = 3$) which are closest to the p^{th} analysis grid point.

3.5.2.4 Data Merging Rule

To reconstruct a rainfall field to the original scale an inverse wavelet transform is applied. The rule adopted herein is to pick decomposed radar or raingauge fields (average and gradient), whichever is large, for merging. The radar and raingauge rainfall data were decomposed to only 4 dyadic scales (i.e., $m = 4$ in sections 3.5.2.1 and 3.5.2.2 above), because of size limitation of the 32 x32 pixels window selected. To illustrate the merging rule, the decomposed fields from the first scale (level) of decomposition for storm # 13 of 1994 storms (see Table 3.1) are used.

Figures 3.7b to 3.7d show that the gradient fields from radar data were always larger than that from gauges (i.e., $|r\{R'_{1,i}\}_{i=1,2,3}| > |g\{R'_{1,i}\}_{i=1,2,3}|$), because radars have more sampling points than gauges and hence they tend to capture well the rainfall spatial gradient. Absolute values were used in the comparison because rainfall gradients can be positive or negative. A perusal of Figures 3.7b to 3.7d reveals that the three gradient fields have different characteristics such that the magnitude of the diagonal field is relatively “mild” as compared to the horizontal (x) and vertical (y)

directional fields, as was similarly observed by Kumar and Foufoula-Georgiou (1993).

On the other hand, other than a few cases, decomposed average rainfall from radar was mostly lower than that from gauges (i.e., $r\bar{R}_1 < g\bar{R}_1$) (see Figure 3.7a) partly because rainfall data measured by radar for shallow stratiform storms could suffer from underestimation caused by cloud overshooting problem, e.g., only a small % of the radar beam is filled by the cloud and thus the overall returned power is not representative of the intensity of scattering in the filled region. However, because radar has the ability to capture intense localized storms that can be missed by few raingauges, we see the presence of some isolated large values in radar field ($r\bar{R}_1$) as compared to gauge field ($g\bar{R}_1$) (Figure 3.7a).

3.6 Analysis of Rainfall Data Merging Results

Six storms (Table 3.4) have been selected from 89 storms identified in the period 1994 to 2000. The selection criteria required that the storm should be underestimated by radar at all six raingauges because as shown in Section 4 that radar precipitation underestimation is more critical than overestimation, and the storm duration should be at least 10 hours. Table 3.4 shows the total storm depths based on raingauge data and the difference between total storm depths measured by radar and that by raingauge. The merged WSR-88D radar and raingauge data of the wavelet scheme was compared with that of the SOA scheme in a 32x32 pixels window at 4 x 4 km pixel resolution covering the Blue river basin and its vicinity. The corresponding simulated streamflow hydrographs were also compared with the observed.

3.6.1 Original versus Merged Rainfall Data

The rainfall spatial pattern (contour maps) and the corresponding statistical measures (Table 3.5) based on 32x32 pixels window (i.e., minimum, maximum, spatial mean and standard deviation) were used to assess the quality of merged data. The contour maps for the two largest and longest storms of the six (i.e., storms # 13 and #9) are shown in Figures 3.8 and 3.9, respectively. These two storms were selected partly because they represent the largest underestimations of radar mean rainfall as compared to raingauge measurements.

The contrasting capability of radar and raingauge in measuring rainfall is evident in the contour plots (see Figures 3.8 and 3.9). Visual inspection of these contour plots, mean and standard deviation (Table 3.5) show that radar grossly underestimated the rainfall depth, but the spatial distribution of its rainfall field is much better than the sparsely spaced raingauges. Comparing the merged rainfall data by the wavelet with that of SOA shows that both schemes provide significant improvement over the spatial distributions of gauged rainfall field. Nevertheless, wavelet is better than SOA because besides providing a spatial distribution closer to that of radar as shown by spatial standard deviation (Table 3.5), it also adequately corrected the mean depth of the original radar data, albeit in some cases there is a slight overestimation over the gauge's mean depth. SOA could only partially correct the underestimation of mean depth by the radar data. The slight overestimation of gauge's mean by the wavelet can be partly due to locations of intense rainfall rates where the gradient derived from radar data by wavelet tend to be large. Therefore combining the gradient with the mean rainfall could result in an overestimation of the mean rainfall depths (Table 3.5).

The complementary capabilities of radar and raingauge are generally better exploited by wavelet than SOA because: (a) a multi-resolution analysis employed by wavelet (i.e., four scales herein) considers a wider range of rainfall fields as compared to a simple linear relationship employed by SOA using only three nearby

raingauge stations in the merging process (see Eq. 3.1), (b) the wavelet extracts individual rainfall gradients for merging with the mean rainfall while SOA uses only the weighted difference between radar and gauged data to merge with the radar data, and (c) wavelet can better represent localized features of the rainfall process (Perica and Foufoula-Georgiou, 1996).

At point scale, e.g., at the six raingauge locations, the cumulative rainfall plots for each storm at the raingauge location where there was a significant radar underestimation of gauge rainfall data (see Table 3.4) are shown in Figure 3.10. It can be seen clearly that the radar underestimated the storm almost throughout the storm duration in comparison to gauge measurement for all six cases. As the cumulative rainfall plot of the wavelet scheme tried to follow both the gauge and radar traces closely, it resulted in a wavelet total rainfall amounts falling almost in between that of gauge and radar. Conversely, the SOA traces are biased towards the gauge measurements almost throughout the storm for all storms analyzed, resulting in almost identical storm totals with the gauges (Figure 3.10). At a point scale, SOA is biased towards gauge measurements because SOA uses three nearby raingauge stations in the merging process, which means that raingauge locations that were the closest to the radar grid points were used in this analysis and hence they had more influence to the merged results through SOA; this is not the case for the wavelet scheme because it operates in grid format using a multi-resolution analysis. Although SOA's total rainfall is always larger than that of wavelet at a point scale, at the basin scale it is the reverse (Table 3.5). In general wavelet is more superior to SOA as will be further demonstrated in Section 3.6.2.

3.6.2 Hydrologic Simulation

There are contradictory views regarding the potential impact of radar rainfall errors in hydrologic modeling. For instance, Numec (1985) argued that errors in precipitation input to a rainfall-runoff model would result in significant errors in estimated runoff. Wyss et al. (1990) suggested that runoff prediction errors due to

radar rainfall errors are less significant than errors due to rainfall-runoff transformation or modeling errors. Winchell et al. (1998) stated that there is not yet a consensus on the effects of radar data uncertainty on hydrologic modeling, nor has the topic received adequate attention, e.g., most of the research on radar rainfall uncertainty has been to compare radar with their raingauge counterparts without analyzing their influence on basin-scale hydrologic simulations (e.g., Smith et al., 1996; Stellman et al., 2001; Jayakrishnan et al., 2004). Borga (2002) reported that, albeit there are problems separating uncertainty in radar rainfall data from modeling errors, hydrologic modeling remains a viable approach to assessing the suitability of radar over gauge rainfall data in basin hydrologic studies. Applying a lumped conceptual hydrologic model to the Brue catchment, he found that adjusted radar rainfall improved modeling results significantly as compared to unadjusted radar estimates. Furthermore, meaningful hydrologic predictions might still be elusive unless uncertainties of radar-derived precipitation can be quantified and corrected for (Jayakrishnan et al., 2004).

The quality of both the merged rainfall data by wavelet and SOA schemes was assessed in terms of hydrologic simulation by the Distributed Physically based Hydrologic Model using Remote Sensing data (DPHM-RS) (Biftu and Gan, 2001, 2004). Four storms, with their dates extended so as to cover the entire flood wave, were selected for streamflow simulation (Table 3.6). The two 1998 storms, representing winter and summer seasons (i.e., storm # 2 and 6) where there was little or no radar underestimation problem (see Table 3.1), were used for calibration and validation of the DPHM-RS model respectively. The remaining two storms in Table 3.6 where the radar underestimated the raingauge data at all six gauges (see Table 3.4) were used to assess the effect of radar rainfall errors in hydrologic modeling and the improvement gained by merging it with gauged rainfall data. From the DEM data, BRB was divided into 7 sub-basins of comparable sizes (see Figure 3.1b) to ensure more or less similar sub-basin response functions for deriving the surface runoff, so no one sub-basin dominate the overall hydrograph at the basin

outlet. The simulations began with BRB at a “near wet” antecedent moisture condition (AMC), because the events selected were preceded by other storms. Further, this “near wet” AMC will lead to more dynamic responses from BRB to rainstorms than dry AMC that requires much rainfall to soak up the dry soil mantle before surface runoff can expect to occur.

3.6.2.1 DPHM-RS Rainfall-Runoff Model

DPHM-RS is a semi-distributed, physically based, hydrologic model developed by Biftu and Gan (2001; 2004). It is chosen for this study partly because it is designed to exploit the potential of distributed information retrievable from remotely sensed data (e.g., topographical information and land use) in hydrologic modeling, but it avoids the unnecessary computation demand of a fully distributed model by capturing the essential physics of runoff generation at sub-basin (or semi-distributed) scale. DPHM-RS is divided into six components: interception, evapotranspiration (ET), soil moisture, subsurface flow, surface flow, and channel routing.

DPHM-RS accounts for two types of surface runoff generation mechanisms: (1) Hortonian or infiltration-excess, and (2) saturation-excess, for vegetated and bare land separately. In modeling the saturated subsurface flow, the spatial variability of topography; soil properties; and the average water table depth for each sub-basin is parameterized by the topographic soil index ($= \ln(a_i T_e / T_i \tan \beta_i)$), where T_e is the catchment mean saturated transmissivity, T_i , $\tan \beta_i$ and a_i are the local transmissivity, slope and drainage area for pixel i , respectively. Land surface evaporation and canopy transpiration are computed separately. The surface runoff for each sub-basin is based on its average response function derived by the kinematic wave equation. To obtain this response function, a reference excess rainfall of 1.0 cm depth is supplied to all grid cells within each sub-basin for one time step. Then for each grid cell, the kinematic wave function is applied and the

flow is routed from cell to cell based on an eight possible flow directions until the reference rainfall excess for each sub-basin is exhausted. Routing through the drainage network is accomplished by the Muskingum-Cunge routing method.

The input data and calibrated parameters of the DPHM-RS model are summarized in Tables 3.7 and 3.8 respectively. Only three parameters were calibrated (i.e., exponential decrease parameter for the saturated hydraulic conductivity (F), surface and channel Manning roughness (n_m)), and all of them have moderate model sensitivity (see Table 3.8). These three parameters were estimated from land use classes or literature values and refined through calibration. The other parameters were either directly derived from field observation, space platforms data, and literature. During calibration and validation, radar and raingauge rainfall data were used as input in driving the hydrologic model. The simulated hydrographs are shown in Figure 3.11, where the AMC was assumed to be 90% of saturation moisture, which was reasonable given that the selected storm events were preceded by other storms.

3.6.2.2 Effect of Merging Radar and Gauge Rainfall on Streamflow Simulation

In general, the radar-gauge rainfall data comparison carried out in Section 3.4 indicated that radar tend to report more rainfall than gauges for convective storms and less rainfall for stratiform storms, which is also reflected in the hydrographs estimated by DPHM-RS in Figures 3.11b and 3.12a that almost represents pure convective and stratiform storms respectively. Since radars have high spatial resolution and measure rainfall using a large volume sample, they tend to measure more accurately the highly spatially variable convective storms than raingauges. As for stratiform storms, sparsely spaced raingauges can still accurately capture such storms partly because stratiform systems are less spatially variable than convective systems. Given the performance of weather radar tends to deteriorate at ranges far from the radar site (Smith et al., 1996), radars potentially underestimated these

shallow stratiform storms because of radar range effect, cloud overshooting (Sharp, 1997; Pereira et al., 1998; Young et al., 1999) and missing intensive rainfall close to the ground due to low-level growth in an environment of warm rainfall processes (Steiner et al., 1999), a typical characteristic of stratiform systems. These problems are typical for BRB because four out of five WSR-88Ds providing coverage to BRB are located at significant distances away (see Figure 3.1a).

There are exceptions to the above general observations such as gauges reporting more rainfall than radar in a season dominated by convective storms which can be caused by a dominant stratiform component that is normally associated with the mature to dissipating stages of the convective systems (Schumacher and Houze, 2003). Conversely, radar can report more rainfall than gauges in a season dominated by stratiform storms such as the case of Figure 3.11a for two possible reasons: (a) the stratiform storm may be associated with a deep convective system (Schumacher and Houze, 2003) that resulted in more accurate radar rainfall than gauged rainfall data (Figure 3.11a), and (b) the ability of radar to capture intense localized storms that can be missed by the few rain gauges.

The streamflow hydrographs simulated out of merged radar-gauge rainfall data for two events are shown in Figure 3.12. The inability of a few raingauges to capture the spatial variability of rainfall is reflected by the time-to-peak-flow error, which is smaller for radar than raingauge derived streamflow hydrographs (Table 3.9). Hydrographs predicted by Wavelet merged rainfall data are better than that of SOA merged rainfall data, particularly for the event dated December 8-14, 1994 (storm # 13 in Table 3.6) that is possibly a pure stratiform storm (Figure 3.12a). The improvement of Wavelet results over that of raingauge estimated hydrographs is indicated by the reduction of time-to-peak error (see Table 3.9), which was also observed by Krajewski et al. (1991) for spatially more representative rainfall. Further, the time-to-peak error for Wavelet results is more or less equal to that of radar (Table 3.9), which shows the effectiveness of wavelet analysis in extracting

the rainfall gradient of the rainfall process measured by the radar for merging with the mean rainfall of gauge data. However, the Wavelet merging may lead to slight increase in discharge volume (e.g., +16.49% for storm # 13 in Table 3.9) because of the slight increase in the mean rainfall as compared to the original gauge rainfall data (see Table 3.5). As explained in Section 3.6.1, the slight overestimation of mean rainfall by the wavelet can be partly attributed to locations of intense rainfall rates where the gradient derived from radar data by the wavelet tend to be large, and hence its combination with the gauged rainfall could result in the overestimation of the mean rainfall depths. Improving the estimation of both peak-flow magnitude and time-to-peak error is very crucial for operational flood prediction.

3.7 Discussion and Conclusions

The findings of this study and references herein suggests that, the bias correction using raingauge data applied to produce WSR-88D stage III rainfall data sometimes is not adequate. This can be attributed to sparsely spaced point raingauge data being used to correct the bias of radar data map, difficulty in identifying rainfall type resulting into use of a wrong bias adjustment factor, georeferencing errors, and data processing errors such as averaging of overlapping radar data.

Georeferencing errors inherent in WSR-88D stage III radar data are introduced through coordinate transformation of the original radar measurement from polar (1-km x 1-degree resolution) to rectangular HRAP grid with resolution of 4 x 4 km. Errors in georeferencing occur due to the combined effects of scale and shape distortions. Reed and Maidment (1999) and Jayakrishnan et al. (2004) indicated that the effects of scale and shape distortions vary with latitude, and the difference between the actual range of the radar and the mapped range could vary from +1.6 to +3.1 km (in 30-45° N latitude range) and from +0.35 to -3.55 km (in 25-35° N latitude range) depending on radar orientation. Given that the HRAP grid pixel of WSR-88D is approximately 4 km, a mapping error in the order of 2-3 km could

move the location of the actual volume scan of radar to the adjacent HRAP grid pixel and away from the actual collocated raingauge location especially if it is near the edge of the HRAP grid pixel. Furthermore, the maximum georeferencing errors occur at the maximum range of the WSR-88D (230 km) and should reduce as one gets closer to the radar location (Jayakrishnan et al., 2004). Since BRB is located in 33-34° N latitude range and four out of five WSR-88Ds provide coverage to BRB at their maximum ranges (Figure 3.1a), the WSR-88D data of BRB are expected to suffer from georeferencing errors.

Also, it is difficult to regard the difference in radar-gauge comparison as pure radar rainfall estimation error because as point measurements gauged data are not the exact ground truth for the areally-averaged radar rainfall (Ciach and Krajewski, 1999; Di Michele et al., 2001). Based on studies on extreme spatial/temporal rainfall variability (Crane, 1990; Lovejoy and Schertzer, 1990; Over and Gupta, 1994), the large resolution difference between raingauge and radar, as much as 9 orders in area, should lead to significant differences between the two measurements. Therefore, direct comparisons of data from raingauge and radar are problematic. Kitchen and Blackall (1992) showed that the contribution of the raingauge data sampling error to the radar-gauge difference could be as large as 50-80% for instantaneous and hourly rainfalls at a grid size of 3x3 km. Hence, the spatial/temporal rainfall variability could introduce sampling errors in the WSR-88D stage III data during data processing stages that normally employ hourly gauge measurements for adjusting radar bias (see section 3.2), and the subsequent results like those presented in this study where point gauge data are compared with 16-km² areally-averaged radar rainfall data and merged radar-gauge data. Techniques suggested by Ciach and Krajewski (1999) on partitioning the difference between radar and gauge rainfall measurements into the error of area-averaged radar estimates and error due to the difference between the sampling areas of the two instruments, and Di Michele et al. (2001) on derivation of areal reduction factors for

point measurements of storm rainfall from its scaling properties could be adapted to improve the comparison and adjustment results.

Even though a practical approximation, the correlation functions are based on the assumptions of homogeneity and isotropy that strictly speaking cannot be true. Beside the inter-site distance, we would expect the inter-site correlation to also depend on factors such as vegetation cover, wind directions and circulations, and other possible climatic and topographic factors. In merging radar and gauged data, especially that of the wavelet scheme, we demonstrated that despite scaling rainfall depth of radar to that of raingauges, the spatial variability of the original radar data can still be maintained. However, some data noise/errors present in the original radar or raingauge data cannot be filtered by the wavelet or SOA schemes. For example, Pereira et al. (1998) showed that areas with artificially large rainfall gradients coincide with transition zones of overlapping radar surveillance, and is caused by a simple averaging of overlapping radar rainfall data to produce a mosaic of individual radar rainfall fields (see section 3.2). Bands in the x- and y- directions present in the rainfall contour plots in Figures 3.8b to 3.8d likely indicate the presence of such data noise or artifacts because those bands are not present in the rainfall contour map of Figures 3.9b to 3.9d. In view of these limitations, it is natural that assessing the quality of radar rainfall data and its derivatives through hydrologic simulation has its own problems because of the difficulty in separating uncertainties due to radar rainfall measurements, inadequate hydrologic model structure, and other input data problems (Winchell et al., 1998; Borga, 2002).

Despite the aforementioned problems of data and the inadequacy of model structure (simplified version of nature), and others, generally we can still expect gaining insight into the usefulness of radar-gauge merged data over radar or gauge data alone in basin hydrologic studies. The goodness-of-fit between observed and simulated hydrographs, and contour plots of rainfall fields provide some basis to

assess the improvement gained from merging radar and gauged rainfall data by the wavelet and the SOA methods. Below are the conclusions of the study:

- (a) The year-to-year comparison of radar-gauge rainfall data over the 1994-2000 period shows that the WSR-88D radar network underestimated precipitation in 92%, 83%, 67%, 67%, 33%, 44%, and 46% of the storms. This shows a general improvement in the accuracy of the WSR-88D data over the years, with the radar underestimation of rainfall for 1998-2000 being significantly lower than that of 1994-1997. This reduction in radar underestimation errors is due to the on-going improvements in the WSR-88D precipitation processing algorithms by the NWS of USA.
- (b) The WSR-88D underestimation of precipitation was generally more pronounced during the cold season (September to February) normally dominated by stratiform storms as compared to warm season (March to August) normally dominated by convective storms. Over the 7-year period, the number of storms (in %) underestimated by radar during cold season or winter (warm season or summer) were 100% (83%), 100% (78%), 67% (67%), 73% (50%), 27% (50%), 67% (33%), and 25% (80%), respectively.
- (c) The overestimation trend in rainfall observed due to recent modifications of the WSR-88D precipitation processing algorithms is less critical than its underestimation problem. Using all available storms in a year, the results showed that the average estimation bias over the six-raingauge locations for 1994 (largest underestimation) and 1998 (largest overestimation) was - 8.29% and 4.83% respectively, which means that underestimation is almost twice as much as overestimation.
- (d) With respect to gauged data, the wavelet technique is quite consistently better than SOA in predicting the mean field depths. However, wavelet tends to slightly under-estimate while SOA tends to slightly over-estimate

the standard deviation of radar. Though wavelet may have an edge over SOA but more extensive tests are necessary before we can decisively conclude which technique is better in exploiting the complimentary nature of both radar and raingauge.

- (e) The quality of rainfall data was assessed in terms of streamflow hydrographs simulated by the hydrologic model DPHM-RS. The time-to-peak-flow error for radar derived streamflow hydrographs was smaller than that of raingauges, which is mainly caused by the insufficiency of raingauges to capture the spatial variability of rainfall.
- (f) There is a marked improvement in the volume/depth of streamflow hydrographs predicted by wavelet merged input rainfall as compared to that of SOA merged data, and the former data is also better than the raingauge data alone in terms of the reduction of time-to-peak error. Both these results show the effectiveness of wavelet in extracting the rainfall gradient of the rainfall process measured by the radar. The results also indicate that even a raingauge network that is not dense (i.e., 6 gauges in 1233 km² herein) is sufficient to improve the underestimation of radar rainfall data, and the improvement increases with increasing difference between gauged and radar rainfall depths. However, wavelet cannot remove (and sometimes amplifies) the fictitious sharp gradients in radar rainfall, which according to Pereira et al. (1998) are produced by the averaging process in areas of overlapping radar coverage particularly at the fringes of the radar umbrellas.
- (g) The quality assessment of radar rainfall data using raingauges and the subsequent merging of the two is affected by georeferencing errors inherent with WSR-88D stage III data, sampling issues associated with the comparison between areally averaged and point observations and its interpolated derivative. It is recommended that future work should try to quantify the amount of these errors.

References

- Anagnostou, E. N., Krajewski, F. W., Seo, D. J., and Johnson, E. R. (1998), Mean-field rainfall bias studies for WSR-88D. *J. Hydrol. Engng. Am. Soc. Civ. Engrs*, 3 (3), 149-159.
- Atlas, D., Rosenfield, D., and Jameson, A. R. (1997), Evolution of radar rainfall measurements: Steps and mis-steps. *Weather Radar Technology for Water Resources Management*, B. Braga and O. Massambani, Eds., UNESCO, 1-60.
- Baeck, M. L., and Smith, J. A. (1998), Rainfall estimation by the WSR-88D for heavy raining events. *Weather and Forecasting*, 13, 416-436.
- Biftu, G. F., and Gan, T. Y. (2004), Semi-distributed, Hydrologic Modeling of Dry Catchment with Remotely Sensed and Digital Terrain Elevation Data. *Int. J. Remote Sensing*, 25(20), 4351-4379.
- Biftu, G. F., and Gan, T. Y. (2001), Semi-distributed, physically based, hydrologic modeling of the Paddle River Basin, Alberta, using remotely sensed data, *J. of Hydrology*, 244, 137-156.
- Borga, M. (2002), Accuracy of radar rainfall estimates for stream flow simulation. *J. of Hydrology*, 267, 26-39.
- Borga, M., Anagnostou, E. N., and Krajewski, W. (1997), A simulation approach for validation of a bright band correction method. *J. Appl. Meteor.*, 36, 1507-1518.
- Brandes, E. A., Vivekanandan, J., and Wilson, J. W. (1999), A comparison of radar reflectivity estimates of rainfall from collocated radars. *J. of Atmosphere and Oceanic Technology*, 16, 1264-1272.
- Ciach, C. J., and Krajewski, F. W. (1999), On the estimation of radar rainfall error variance, *Adv. Water Resour.*, 22 (6), 585-595.
- Collier, Ch.C. (1996), *Application of weather radar systems*, Praxis Publishing Ltd., ISBN 0-471-96013-6, 360 pp.
- Crane, R. K. (1990), Space-time structure of rain rate field. *J. of Geophysical Research*, 95, 2011-2020.

- Datta, D., Jones, W. L., Roy, B., and Tokay, A. (2003), Spatial variability of surface rainfall as observed from TRMM field campaign data. *J. of Applied Meteorology*, 42, 598-610.
- De Michele, C., Kottegoda, N. T., and Rosso, R. (2001), The derivation of areal reduction factor of storm rainfall from its scaling properties. *Water Resources Research*, 37 (12), 3247-3252.
- Frederick, R. H., Miller, J. F., and Tracey, R. J. (1977), *Five to Sixty Minute Precipitation Frequency for the Eastern and Central U.S.*, NOAA Technical Memorandum NWS Hydro-35, Silver Springs, MD.
- Fulton, R. A., Breidenbach, J. P., Seo, D. -J., Miller, D. A., and O'Bannon, T. (1998), The WSR-88D rainfall algorithm. *Weather and Forecasting*, 13, 377-395.
- Gabella, M., and Amitai, E. (2000), Radar rainfall estimates in an alpine environment using different gage adjustment techniques. *Phy. Chem. Earth (B)*, 25, 927-931.
- Gandin, L. S. (1963), *Objective Analysis of Meteorological Fields*. Translated by R. Harding, Israel Program for Scientific Translation, 242 pp.
- Groisman, P. Y., and Legates, D. R. (1994), The accuracy of United States precipitation data. *Bull. Amer. Meteor. Soc.*, 75, 215-227.
- Jayakrishnan, R., Srinivasan, R., and Arnold, J. G. (2004), Comparison of raingage and WSR-88D stage III precipitation data over the Texas-Gulf basin, *J. of Hydrology*, 292, 135-152.
- Joss, J., and Waldvogel, A. (1990), Precipitation measurements and hydrology, *Radar in Meteorology*, D. Atlas, Ed., Amer. Meteor. Soc., 577-600.
- Joss, J., and Lee, R. (1995), The application of radar-gauge comparisons to operational precipitation profile corrections. *J. of Applied Meteorology*, 34, 2612-2639.
- Kitchen, M., and Blackall, R. M. (1992), Representativeness errors in comparisons between radar and gauge measurements of rainfall. *J. of Hydrology*, 134, 13-33.

- Klazura, G. E., and Imy, D. A. (1993), A description of the set of analysis products available from the NEXRAD WSR-88D system. *Bull. Amer Meteor. Soc*, 74, 1293-1311.
- Koch, S., Desjardins, M., and Kocin, P. (1983), An interactive Barnes objective map analysis scheme for use with satellite and conventional data. *J. of Climate Applied Meteorology*, 22, 1487-1503.
- Krajewski, W. F., Lakshmi, V., Georgakakos, K. P., and Jain, S. C. (1991), A monte-carlo study of rainfall sampling effect on a distributed catchment model. *Water Resources Research*, Vol. 27, No. 1, 119-128.
- Kumar, P., and Foufoula-Georgiou, E. (1993), A multicomponent decomposition of spatial rainfall fields, 1. Segregation of large- and small-scale features using wavelet transforms. *Water Resour. Res.*, 29(8), 2515-2532.
- Legates, D. R., and DeLiberty, T. L. (1993), Measurement biases in the United States rain gauge network. *Water Resour. Bull.*, 29, 855-861.
- Lott, N., and Sittel, M. (1996), A comparison of NEXRAD rainfall estimates with recorded amounts. *National Climatic Data Center*, Technical Report 96-03. Asheville, NC.
- Lovejoy, S., and Schertzer, D. (1990), Fractals, raindrops, and resolution dependence of rain measurements. *J. of Applied Meteorology*, 29, 1167-1170.
- Mallat, S. (1989), A theory for multiresolution signal decomposition: The wavelet representation. *IEEE Trans. Pattern Anal. Mach. Intel.*, 11(7), 674-693.
- Marquinez, J., Lastra, J., and Garcia, P. (2003), Estimation models for precipitation in mountainous regions: the use of GIS and multivariate analysis. *J. of Hydrology*, 270, 1-11.
- Nash, J. E., and Sutcliffe, J. V. (1970), River flow forecasting through conceptual models, 1. A discussion of principles. *J. of Hydrology*, 10, 282-290.
- Neff, E. L. (1997), How much does a rain gauge? *J. of Hydrology*, 35, 213-220.
- Numec, J. (1985), Water resources systems and climate change. In *Facets of Hydrology*, Vol. II, Edited by J.C. Rodda, pp. 131-152, John Wiley, New York.

- Over, T. M., and Gupta, V. K. (1994), Statistical analysis of mesoscale rainfall: dependence of a random cascade generator on large-scale forcing. *J. of Applied Meteorology*, 33, 1526-1542.
- Pereira Fo, A. J., Crawford, K. C., and Hartzell, C. L. (1996), *Statistical objective analysis scheme for improving WSR-88D rainfall estimates*. Bureau of Reclamation, Rep. R-96-08, 2 vols., Denver, CO, 5pp. [Available from the National Technical Information Service, Operations Division, 5285 Port Royal Road, Springfield, VA 22161.
- Pereira Fo, A. J., Crawford, K. C., and Hartzell, C. L. (1998), Improving WSR-88D Hourly Rainfall Estimates. *Weather and Forecasting*, 13, 1016-1028.
- Perica, S., and Foufoula-Georgiou, E. (1996), Linkage of scaling and thermodynamic parameters of rainfall: Results from mid-latitude mesoscale convective systems. *J. Geophys. Res.*, 101(D3), 7431-7448.
- Pessoa, M. L., Bras, R. L., and Williams, E. R. (1993), Use of weather radar for flood forecasting in the Sieve river basin: a sensitivity analysis. *J. of Applied Meteorology*, 32 (3), 462-475.
- Rawls, W. J., and Brakensiek, D. L. (1985), Prediction of Soil water properties for hydrologic modeling. *Water Management in the Eighties*, ASCE, pp. 293-299.
- Reed, S. M. and Maidment, D. R. (1999), Coordinate transformations for using NEXRAD data in GIS-based hydrologic modeling. *J. Hydrol. Eng. Am. Soc. Civ. Engrs*, 4 (2), 174-182.
- Schumacher, C., and Houze, R. A. (2003), Stratiform rain in the tropics as seen by the TRMM Precipitation Radar, *J. of Climate*, 16, 1739-1756.
- Sharp, J. (1997), Clear-air Radar observations and their application in analysis of Sea breezes. Online at http://www.atmos.washington.edu/~justin/radar_project/
- Smith, J. A., Seo, D. J., Baeck, M. L., and Hudlow, M. D. (1996), An intercomparison study of NEXRAD precipitation estimations. *Water Resources Research*, 32(7), 2035-2045.
- Sokol, Z. (2003), Utilization of regression models for rainfall estimates using radar-derived rainfall data and rain gauge data. *J. of Hydrology*, 278, 144-152.

- Steiner, M., Smith, J. A., Burges, S. J., Alonso, C. V., and Darden, R. W. (1999), Effect of bias adjustment and rain gauge data quality control on radar rainfall estimation. *Water Resources Research*, 35 (8), 2487-2503.
- Stellman, K. M., Fuelberg, H. E., Garza, R., and Mullusky, M. (2001), An examination of Radar Rain Gauge-Derived Mean Aerial Precipitation over Georgia Watersheds. *Weather and Forecasting*, 16, 133-144.
- Story, G.J. (1996), The use of the hourly digital precipitation array at the West Gulf River Forecast Center, *Intermountain Advanced WSR-88D Users Workshop*, WSR-88D Operational Support Facility, Norman, OK. http://www.srh.noaa.gov/wgrfc/resources/projects/hdp_paper/default.html.
- Tabios, G. Q., and Salas, J. D. (1985), A comparative analysis of techniques for spatial interpolation of precipitation. *Water Resour. Bulletin*, 21(3), 365-380.
- Vignal, B., and Krajewski, F. W. (2001), Large-sample evaluation of two methods to correct range-dependent error for WSR-88D rainfall estimates. *J. Hydrometeorol.*, 2, 490-504.
- Westrick, K. J., Mass, C. F., and Colle, B. A. (1999), The limitations of the WSR-88D radar network for quantitative precipitation measurement over the coastal western United States. *Bull. Am. Meteorol. Soc.*, 80 (11), 2289-2298.
- Winchell, M., Gupta, H. V., and Sorooshian, S. (1998), On the simulation of infiltration- and saturation- excess runoff using radar-based rainfall estimates: Effects of algorithm uncertainty and pixel aggregation. *Water Resources Research*, 34(10), 2655-2670.
- Wyss, J., Williams, E. R., and Brass, R. L. (1990), Hydrologic modeling of New England river basins using radar rainfall data. *J. Geophys. Res.*, 95(D3), 2143-2152.
- Young, C. B., Nelson, B. R., Bradley, A. A., Smith, J. A., Peters-Lidard, C. D., Kruger, A., and Baeck, M. L. (1999), An evaluation of NEXRAD precipitation estimates in complex terrain. *J. Geophys. Res.*, 104, 19691-19703.

Young, C. B., Bradley, A. A., Krajewski, F. W., and Kruger, A. (2000), Evaluating NEXRAD multisensor precipitation estimates for operational hydrologic forecasting. *J. Hydrometeorol.*, 1 (3), 241-254.

Table 3.1 1994-2000 annual information on the selected 89 storms and the corresponding results of accuracy assessment of WSR-88D stage III precipitation data using raingauge data: Gauge and Radar columns show the average storm depth over the six gauge locations, and N is the number of raingauges with radar underestimation.

Storm #	Date (Time)	Duration [hrs]	Gauge [mm]	Radar [mm]	N	Radar - Gauge [mm]
Year 1994						
1	Feb 28 (1800) - Mar 2 (0700)	38	52.71	51.05	4	-1.66
2	Apr 29 (0700) - Apr 29 (2200)	16	52.11	37.18	5	-14.94
3	May 2 (0900) - May 3 (0100)	17	47.58	43.43	4	-4.15
4	May 26 (0300) - May 26 (0800)	6	47.75	39.31	5	-8.44
5	May 29 (1300) - May 29 (1500)	3	31.03	25.87	6	-5.17
6	Jul 9 (0700) - Jul 9 (2000)	14	44.11	43.14	2	-0.98
7	Aug 7 (1500) - Aug 7 (2300)	9	39.62	47.26	2	7.64
8	Oct 7 (1800) - Oct 8 (0700)	14	37.81	32.79	6	-5.02
9	Nov 5 (0400) - Nov 5 (1400)	8	18.37	15.91	4	-2.46
10	Nov 9 (0900) - Nov 9 (1800)	10	26.55	19.08	6	-7.47
11	Nov 13 (2300) - Nov 15 (1000)	36	67.73	65.82	3	-1.91
12	Nov 20 (0100) - Nov 20 (1700)	17	25.70	24.61	3	-1.09
13	Dec 08 (0800) - Dec 10 (0200)	43	47.88	35.16	6	-12.72

Table 3.1 continued

Storm #	Date (Time)	Duration [hrs]	Gauge [mm]	Radar [mm]	N	Radar - Gauge [mm]
Year 1995						
1	Jan 26 (1400) - Jan 27 (0800)	20	19.24	12.33	6	-6.91
2	Mar 07 (0100) - Mar 7 (1100)	11	18.59	14.66	5	-3.93
3	Mar 13 (0200) - Mar 13 (1900)	18	60.88	60.73	4	-0.14
4	Apr 3 (2100) - Apr 4 (1300)	17	37.82	33.44	5	-4.38
5	Apr 10 (1200) - Apr 11 (0000)	13	33.06	31.30	2	-1.76
6	Apr 19 (1800) - Apr 20 (0000)	7	24.08	16.29	5	-7.80
7	May 1 (0200) - May 1 (0900)	8	27.90	28.01	3	0.11
8	May 8 (0200) - May 8 (1300)	12	55.46	61.41	3	5.95
9	May 24 (0200) - May 24 (0500)	4	14.27	13.79	4	-0.48
10	Jun 10 (1500) - Jun 11 (1400)	24	47.67	46.52	3	-1.14
11	Sep 12 (1000) - Sep 12 (1700)	8	31.41	24.71	5	-6.70
12	Nov 1 (0800) - Nov 1 (1100)	4	21.67	19.92	3	-1.75

Table 3.1 continued

Storm #	Date (Time)	Duration [hrs]	Gauge [mm]	Radar [mm]	N	Radar - Gauge [mm]
Year 1996						
1	Jan 1 (1000) - Jan 2 (0400)	19	21.12	18.62	4	-2.50
2	Mar 18 (0600) - Mar 18 (1700)	12	17.69	13.98	6	-3.72
3	Mar 27 (0700) - Mar 28 (0200)	20	51.90	51.59	5	-0.32
4	Apr 12 (1800) - Apr 13 (0000)	7	31.75	29.98	3	-1.77
5	Apr 22 (0100) - Apr 22 (2300)	23	64.18	68.07	2	3.90
6	Jun 1 (0800) - Jun 1 (1800)	11	72.69	65.81	5	-6.87
7	Aug 27 (0500) - Aug 27 (1500)	11	30.48	31.87	2	1.39
8	Sep 15 (0900) - Sep 15 (1700)	9	44.20	44.49	4	0.29
9	Oct 21 (0300) - Oct 22 (1300)	35	86.44	73.75	5	-12.69
10	Nov 7 (0000) - Nov 7 (1100)	12	63.75	60.92	1	-2.83
11	Nov 24 (0400) - Nov 24 (2000)	17	51.73	47.25	3	-4.48
12	Nov 29 (0400) - Nov 29 (1600)	13	28.70	36.53	1	7.83

Table 3.1 continued

Storm #	Date (Time)	Duration [hrs]	Gauge [mm]	Radar [mm]	N	Radar - Gauge [mm]
Year 1997						
1	Feb 6 (0500) - Feb 6 (2000)	16	18.16	17.74	4	-0.42
2	Feb 7 (0600) - Feb 7 (1800)	13	13.85	13.26	5	-0.59
3	Feb 20 (0000) - Feb 21 (0100)	26	63.80	66.00	0	2.20
4	Feb 25 (2100) - Feb 26 (1600)	20	20.49	22.81	1	2.32
5	Apr 4 (0100) - Apr 5 (0300)	27	37.08	40.68	0	3.59
6	Apr 11 (1000) - Apr 11 (1500)	6	29.89	28.69	3	-1.20
7	Apr 25 (1600) - Apr 25 (2300)	8	22.90	28.20	1	5.30
8	Aug 22 (1300) - Aug 22 (1500)	3	21.97	20.58	5	-1.39
9	Oct 12 (0800) - Oct 13 (0200)	19	42.85	35.16	6	-7.68
10	Oct 23 (1500) - Oct 23 (1800)	4	21.67	20.21	4	-1.46
11	Nov 9 (1300) - Nov 10 (1100)	23	26.67	24.82	2	-1.86
12	Dec 2 (1900) - Dec 3 (0300)	9	19.77	18.50	5	-1.27
13	Dec 7 (2100) - Dec 8 (0300)	7	15.66	15.56	3	-0.11
14	Dec 20 (0900) - Dec 21 (1500)	31	61.89	63.41	1	1.52
15	Dec 23 (1500) - Dec 24 (0200)	12	30.39	30.17	3	-0.23

Table 3.1 continued

Storm #	Date (Time)	Duration [hrs]	Gauge [mm]	Radar [mm]	N	Radar - Gauge [mm]
Year 1998						
1	Jan 4 (0500) - Jan 4 (1900)	15	39.75	44.34	0	4.59
2	Jan 6 (2200) - Jan 8 (0700)	34	35.60	38.92	0	3.32
3	Jan 21 (2300) - Jan 22 (0800)	10	21.59	29.11	2	7.52
4	Jan 26 (0100) - Jan 26 (1400)	14	22.40	22.25	3	-0.14
5	Mar 7 (1300) - Mar 8 (0000)	12	33.53	33.27	3	-0.26
6	Mar 15 (2300) - Mar 16 (1700)	19	42.84	44.21	0	1.37
7	Apr 27 (0000) - Apr 27 (0500)	6	29.89	28.87	2	-1.02
8	Jun 11 (0800) - Jun 11 (1300)	6	25.74	26.95	2	1.21
9	Oct 2 (1200) - Oct 3 (0300)	16	68.62	60.54	3	-8.08
10	Oct 5 (1400) - Oct 6 (1000)	21	32.68	40.35	1	7.67
11	Oct 17 (2100) - Oct 18 (0800)	12	26.75	33.72	2	6.97
12	Nov 1 (1200) - Nov 1 (2000)	9	44.24	45.20	1	0.96
13	Dec 4 (0000) - Dec 4 (1100)	12	40.55	42.36	1	1.86
14	Dec 12 (0000) - Dec 12 (1800)	19	26.29	27.41	3	1.14
15	Dec 18 (2000) - Dec 19 (0300)	8	17.40	16.54	5	-0.86

Table 3.1 continued

Storm #	Date (Time)	Duration [hrs]	Gauge [mm]	Radar [mm]	N	Radar - Gauge [mm]
Year 1999						
1	Jan 29 (0200) - Jan 29 (1700)	16	17.61	18.16	4	0.55
2	Mar 08 (0200) - Mar 8 (1700)	16	29.93	33.34	2	3.41
3	Mar 12 (1100) - Mar 13 (0200)	16	33.99	37.22	1	3.22
4	Mar 27 (1500) - Mar 28 (0900)	19	27.81	26.28	4	-1.53
5	Apr 26 (1400) - Apr 26 (1700)	4	27.81	29.77	3	1.96
6	May 10 (0500) - May 10 (1300)	9	60.96	62.87	3	1.91
7	Jun 24 (2000) - Jun 25 (0100)	6	38.05	26.86	4	-11.20
8	Sep 11 (0500) - Sep 11 (1600)	12	67.23	66.93	4	-0.30
9	Oct 30 (0800) - Oct 31 (1400)	31	45.80	45.16	2	-0.64

Table 3.1 continued

Storm #	Date (Time)	Duration [hrs]	Gauge [mm]	Radar [mm]	N	Radar - Gauge [mm]
Year 2000						
1	Jan 3 (0700) - Jan 3 (1000)	4	13.84	13.34	5	-0.50
2	Jan 8 (0000) - Jan 8 (0900)	10	14.90	15.18	5	0.27
3	Feb 22 (2300) - Feb 23 (0700)	9	28.61	29.02	2	0.41
4	Apr 11 (1600) - Apr 12 (2300)	32	28.41	28.08	4	-0.33
5	May 1 (0300) - May 1 (0700)	5	26.50	24.25	4	-2.25
6	Jun 10 (1400) - Jun 11 (0100)	12	28.83	25.24	2	-3.59
7	Jun 21 (1800) - Jun 22 (0200)	9	18.92	20.97	1	2.04
8	Jul 22 (1100) - Jul 22 (1700)	7	26.41	25.48	3	-0.93
9	Oct 20 (1400) - Oct 21 (0000)	11	23.67	31.68	1	8.01
10	Oct 29 (0400) - Oct 29 (1000)	7	29.72	33.33	2	3.62
11	Nov 5 (2100) - Nov 6 (1200)	16	42.21	42.33	3	0.12
12	Nov 8 (1000) - Nov 8 (1700)	8	22.57	21.37	3	-1.19
13	Nov 23 (0100) - Nov 24 (1900)	43	45.64	47.25	1	1.61

Table 3.2 Radar-gauge comparison statistics for storm events observed in 1994 and 1998, where E_f is the efficiency coefficient and RMSE is the root mean square error.

Year	Statistic	Raingauge station name and number					
		Sulphur (1)	Tishomingo (2)	Madill (3)	Durant (4)	Lane (5)	Centrahoma (6)
1994	Total gauge (mm)	555.76	470.39	674.12	655.33	683.79	599.17
	Radar bias (%)	-13.89	2.87	-7.81	-5.31	-11.36	-14.26
	EE	0.82	0.65	0.77	0.83	0.90	0.58
	RMSE (mm)	3.46	4.01	3.82	3.07	2.49	4.27
1998	Total gauge (mm)	490.73	556.28	457.46	525.78	551.42	576.31
	Radar bias (%)	0.38	11.74	4.31	2.79	2.54	7.32
	EE	0.93	0.21	0.87	0.80	0.84	0.84
	RMSE (mm)	1.61	5.27	2.24	2.64	2.22	2.33

Table 3.3 Fitted spatial correlation models for hourly WSR-88D radar rainfall data.

Model	Estimated Parameters
Reciprocal Model $\rho(d) = \frac{1}{(1 + d/C_o)}$	$C_o = 17.91$
Exponential Model $\rho(d) = \exp\left(-\frac{d}{C_o}\right)$	$C_o = 44.57$
Polynomial Model $\rho(d) = \sum_{i=0}^N a_i d^i$	$N = 9$

Table 3.4 Six storms used for radar-gauge data merging analysis: Total storm depths recorded by gauge and the radar-gauge differences are shown at each individual gauge site.

Year	Storm #	Data Source	Storm Depth (mm) at Raingauge #					
			1	2	3	4	5	6
1994	8	Gauge	30.74	54.10	36.58	27.18	61.22	17.02
		Radar-Gauge	-4.60	-12.52	-6.12	-0.43	-5.36	-1.09
1994	10	Gauge	11.18	30.23	28.70	26.67	30.23	32.26
		Radar-Gauge	-4.20	-13.54	-4.78	-6.20	-4.28	-11.80
1994	13	Gauge	52.84	39.11	40.90	42.92	58.93	52.57
		Radar-Gauge	-21.28	-8.40	-8.45	-10.05	-22.53	-5.62
1995	1	Gauge	14.76	24.38	25.47	17.85	13.30	19.65
		Radar-Gauge	-3.96	-9.19	-12.71	-6.99	-2.33	-6.29
1996	2	Gauge	14.99	18.54	14.73	18.54	19.30	20.06
		Radar-Gauge	-1.31	-12.40	-2.44	-2.47	-1.67	-2.01
1997	9	Gauge	50.55	44.45	32.52	39.12	43.69	46.74
		Radar-Gauge	-17.19	-3.62	-0.08	-10.10	-11.88	-3.22

Table 3.5 Statistical measures of original (raingauge and radar) and merged (SOA and wavelet) rainfall data in a 32 x 32 pixels window at 4 x 4 km pixel resolution.

Year	Storm #	Data Source	Minimum (mm)	Maximum (mm)	Mean (mm)	Standard Deviation (mm)
1994	8	Radar	8.18	62.22	31.53	10.64
		SOA	9.07	65.19	34.69	11.19
		Wavelet	14.29	70.08	38.51	9.26
		Raingage	17.26	61.13	38.06	7.49
1994	10	Radar	1.82	30.86	15.75	5.72
		SOA	3.99	34.77	20.63	6.17
		Wavelet	15.73	41.45	27.61	4.97
		Raingage	11.44	32.21	27.12	3.71
1994	13	Radar	7.13	69.07	31.68	11.27
		SOA	12.64	75.38	39.94	11.29
		Wavelet	27.73	80.44	49.12	10.22
		Raingage	39.13	58.89	48.51	4.30
1995	1	Radar	1.70	29.49	18.50	5.61
		SOA	6.44	33.75	20.01	5.20
		Wavelet	10.05	36.78	25.04	5.41
		Raingage	13.12	32.21	24.89	2.67
1996	2	Radar	5.34	25.31	13.20	3.63
		SOA	8.90	26.00	15.38	2.99
		Wavelet	11.10	28.30	18.01	3.11
		Raingage	14.73	20.04	17.95	1.23
1997	9	Radar	14.88	59.08	34.14	7.54
		SOA	17.29	65.74	39.61	8.20
		Wavelet	25.41	65.97	43.43	7.07
		Raingage	32.53	50.44	42.86	3.39

Table 3.6 Characteristics of the four flood/storm events used in hydrologic simulation: their dates were extended from their respective original selected storms (see Table 3.1) in order to cover the entire flood wave.

Year	Storm #	Date (Time)	Duration [hrs]	Total rainfall depth [mm] ^a		Observed flood peak [m ³ /sec]
1994	13	Dec 8 (0000) - Dec 14 (2300)	168	Radar	34.17	142.35
				SOA	45.24	
				Wavelet	47.99	
				Raingage	48.55	
1995	1	Jan 26 (0000) - Jan 31 (2300)	144	Radar	21.54	44.15
				SOA	26.91	
				Wavelet	27.47	
				Raingage	27.12	
1998	2	Jan 4 (0000) - Jan 11 (2300)	192	Radar	116.70	175.84
				Raingage	114.88	
1998	6	Mar 15 (0000) - Mar 24 (2300)	240	Radar	91.29	202.65
				Raingage	78.30	

^a Total rainfall depth is computed from the Mean Areal Precipitation (MAP) for the entire basin.

Table 3.7 Input data of DPHM-RS rainfall-runoff model.

Data type	Parameters	Source
Topographic	Mean altitude, aspect, flow direction, surface slope, drainage network, and topographic soil index	DEM of USGS National Elevation Dataset (NED)
Land use	Spatial distribution of land use classes, surface albedo, and vegetation index	NOAA-AVHRR satellite data
Soil properties	Spatial distribution of soil types, antecedent moisture content, and soil hydraulic properties	U.S. State Soil Geographic (STATSGO)
Stream flow	Hourly stream flow data at the catchment outlet, channel cross-sections	U.S. Geological Survey (USGS)
Meteorological	Hourly: precipitation, short-wave radiation, air temperature, ground temperature, wind speed, and relative humidity	Oklahoma Mesonet stations and NWS Hydrology Laboratory (NWS-HL)

Note: NWS – National Weather Service; DEM – Digital Elevation Map

Table 3.8 Calibrated parameters of the DPHM-RS model (modified from Biftu and Gan, 2001).

Parameter	Description	Sensitivity	Approach/factor used to estimate parameters
<i>Soil</i>			
F	Exponential decrease parameter for K_s	Moderate	Calibration
K_s	Saturated hydraulic conductivity	Moderate	Soil type
n_m	Manning roughness	Moderate	Calibration
<i>Channel</i>			
\bar{B}	Mean cross-sectional top width	Moderate	Estimated
n_m	Manning roughness	Moderate	Calibration

Table 3.9 Statistics of the simulated hydrographs by DPHM-RS model for the merged and original radar/gage rainfall data.

Year	Event	Data source	% Error in peak discharge	% Error in total discharge volume	Time to peak discharge error ^a	Efficiency (E_f)
DPHM-RS rainfall-runoff model calibration and validation						
1998	2 calibration	Radar	-1.72	-0.75	+25.0	0.92
		Raingauge	+13.90	+5.52	+6.0	0.89
1998	6 validation	Radar	-5.32	-6.48	-25.0	0.87
		Raingauge	-14.07	-18.05	-20.0	0.82
DPHM-RS rainfall-runoff model application						
1994	13	Radar	-36.24	-23.53	+4	0.75
		Raingauge	-10.10	+3.55	+7	0.90
		SOA	-15.99	-0.47	+4	0.91
		Wavelet	-0.66	+16.49	+4	0.91
1995	1	Radar	-49.95	-35.51	-3	0.15
		Raingauge	-8.52	+4.88	-4	0.81
		SOA	-23.48	-13.04	-4	0.77
		Wavelet	-13.44	-3.16	-3	0.91

Negative error denotes underestimation

^a Underestimation of observed peak discharge led to large time to peak error

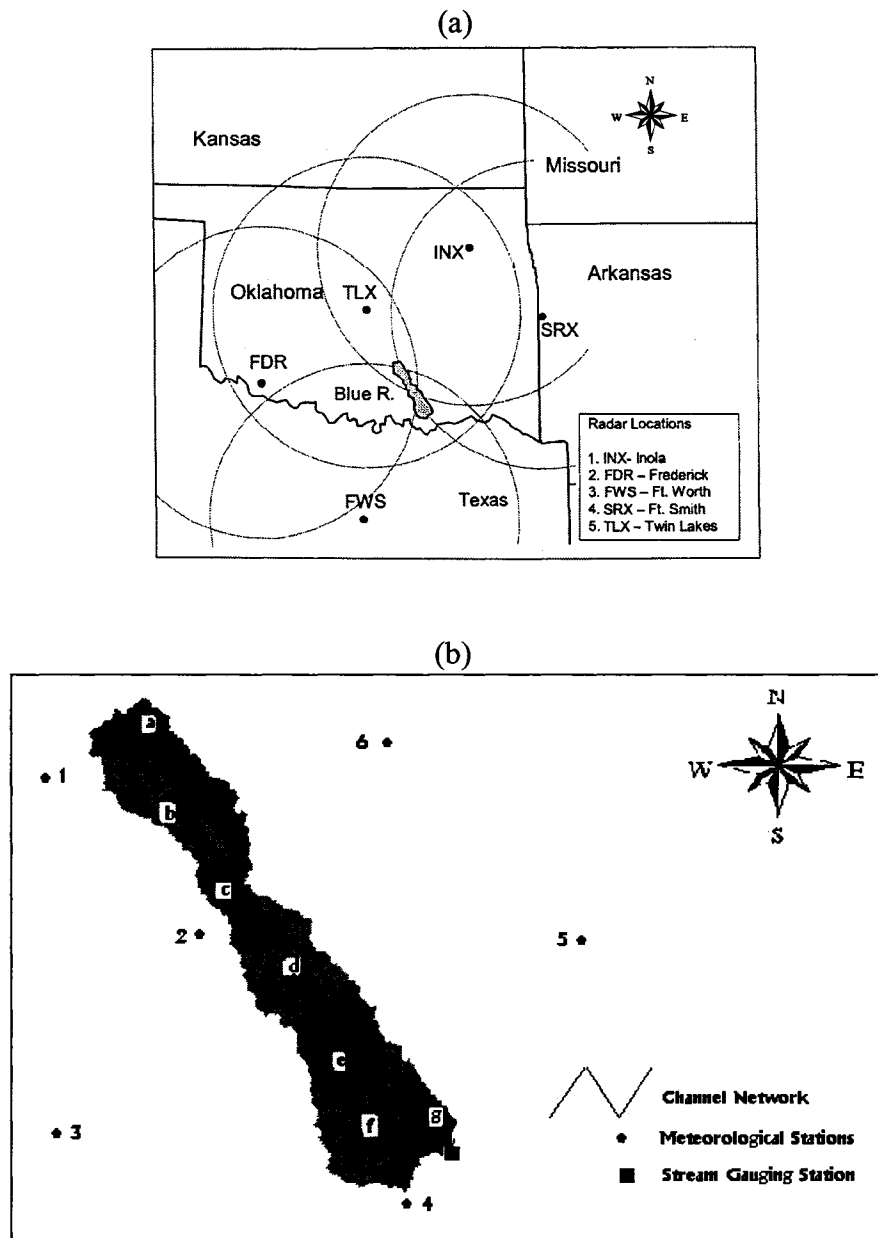


Figure 3.1 Map indicating (a) WSR-88D radar sites providing coverage to Blue River Basin (BRB) of south central Oklahoma (USA): Circles show the radar umbrella with a radius of 230 km, (b) seven sub-basins of BRB derived in this study (label a-g), six Mesonet stations (i.e., raingauge stations) with label 1-6, and a streamflow gauging station.

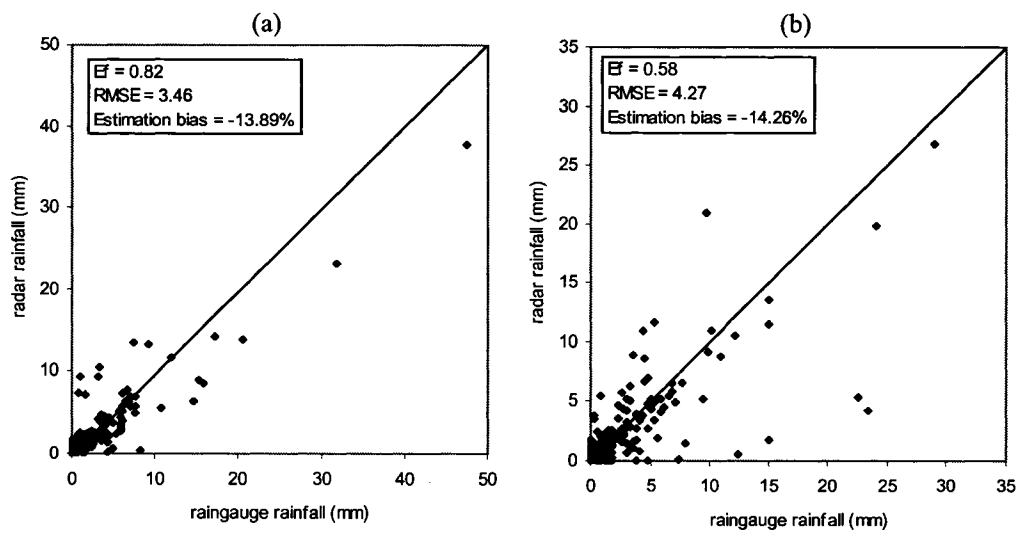


Figure 3.2 Scatterplots of hourly precipitation of radar versus raingauge for all storms selected in 1994 at (a) gauge #1, and (b) gauge #6.

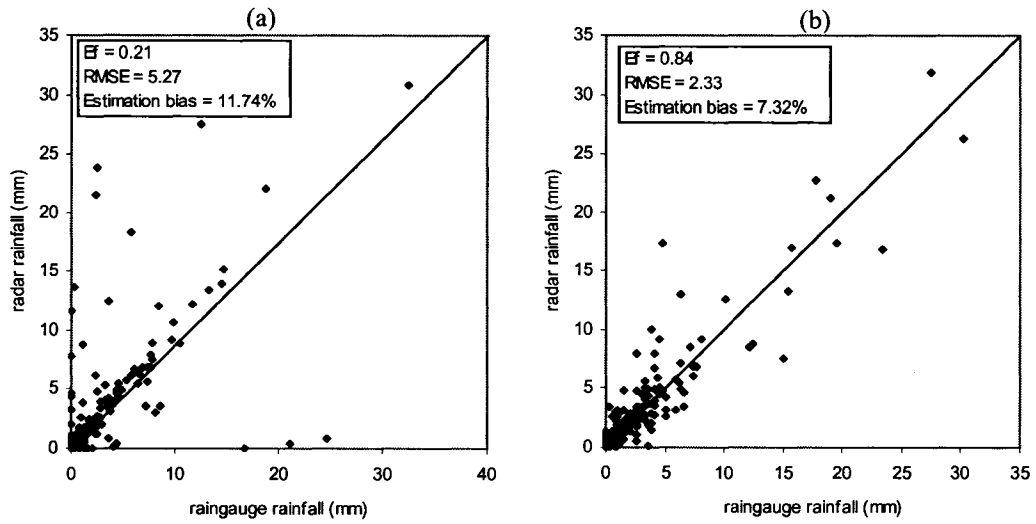


Figure 3.3 Scatterplots of hourly precipitation of radar versus raingauge for all storms selected in 1998 at (a) gauge #2, and (b) gauge #6.

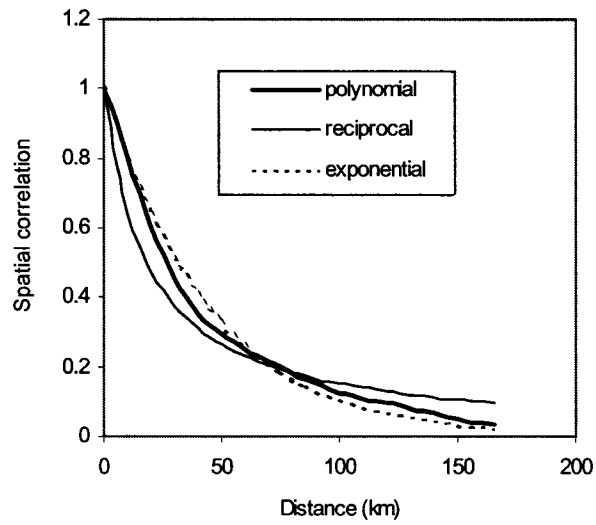


Figure 3.4 Spatial correlation functions fitted to hourly WSR-88D radar rainfall data for the BRB.

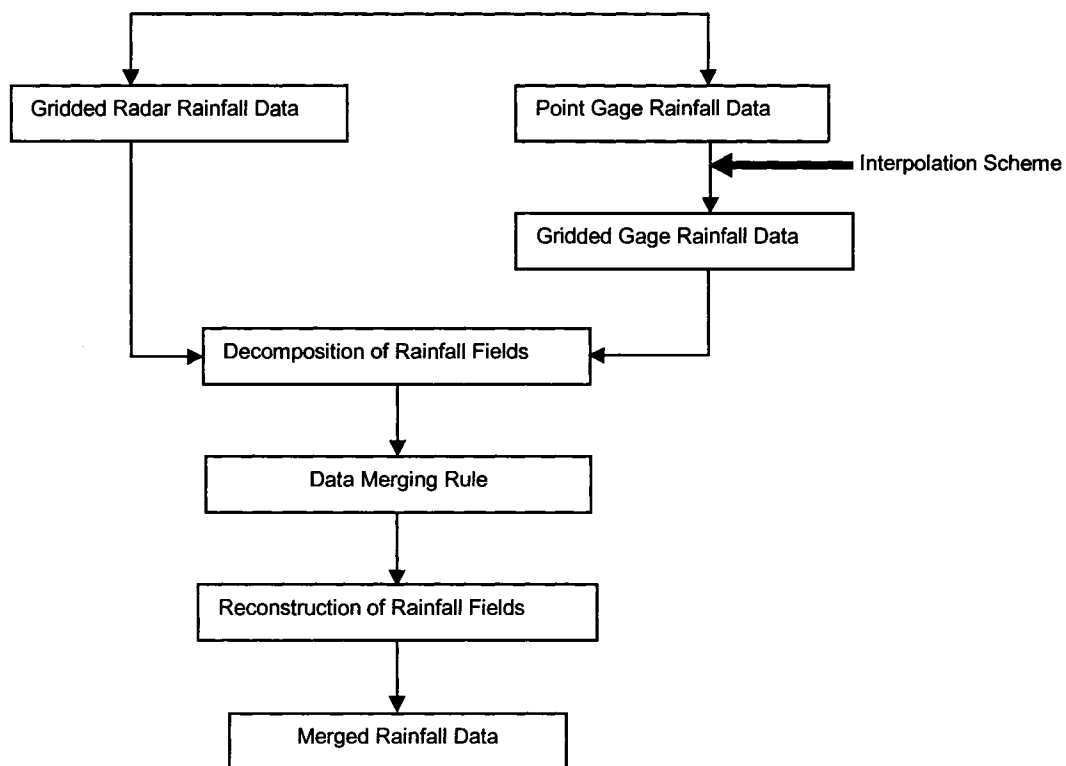


Figure 3.5 Flow chart showing components of the wavelet rainfall data-merging scheme.

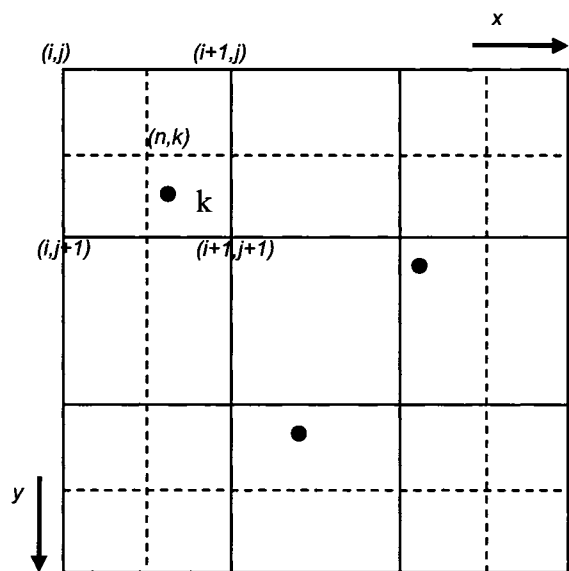


Figure 3.6 A 2-D discretization grid at scales m and $(m+1)$; solid lines define the original spatial resolution at scale m , dashed lines show the grid size at the next higher dyadic scale $(m+1)$, solid circles shows arbitrary raingauge locations.

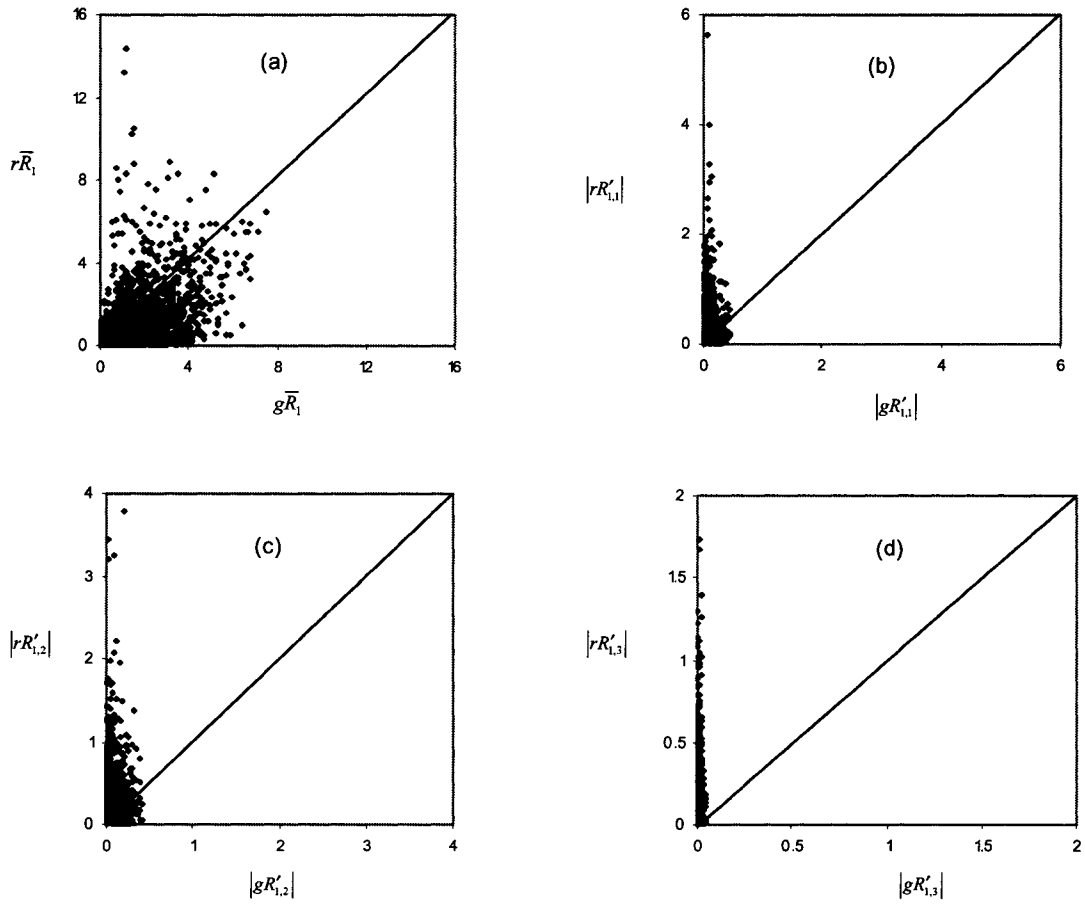


Figure 3.7 Scatterplots of decomposed rainfall fields (mm) between gauge (g) and radar (r) for a typical storm: (a) mean depths, (b) gradients in x direction, (c) gradients in y direction, and (d) gradients in diagonal direction.

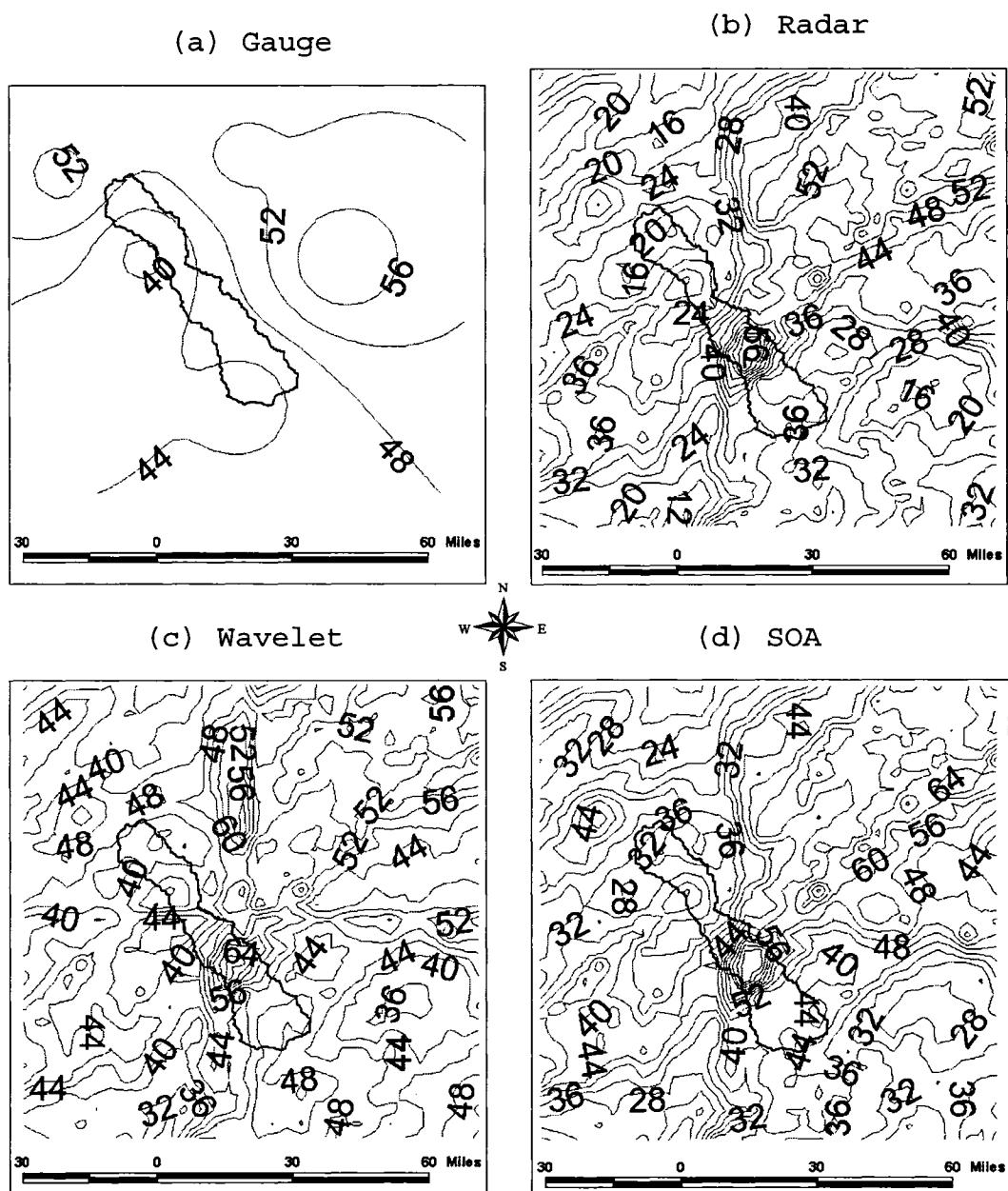


Figure 3.8 Total rainfall contour map (mm) for storm # 13 of December 8 (08:00) – 10 (02:00), 1994 with a 4.0mm contour interval. The original gauge, radar, and radar-gauge merged rainfall fields using wavelet and statistical objective analysis (SOA) schemes are shown from (a) through (d), respectively.

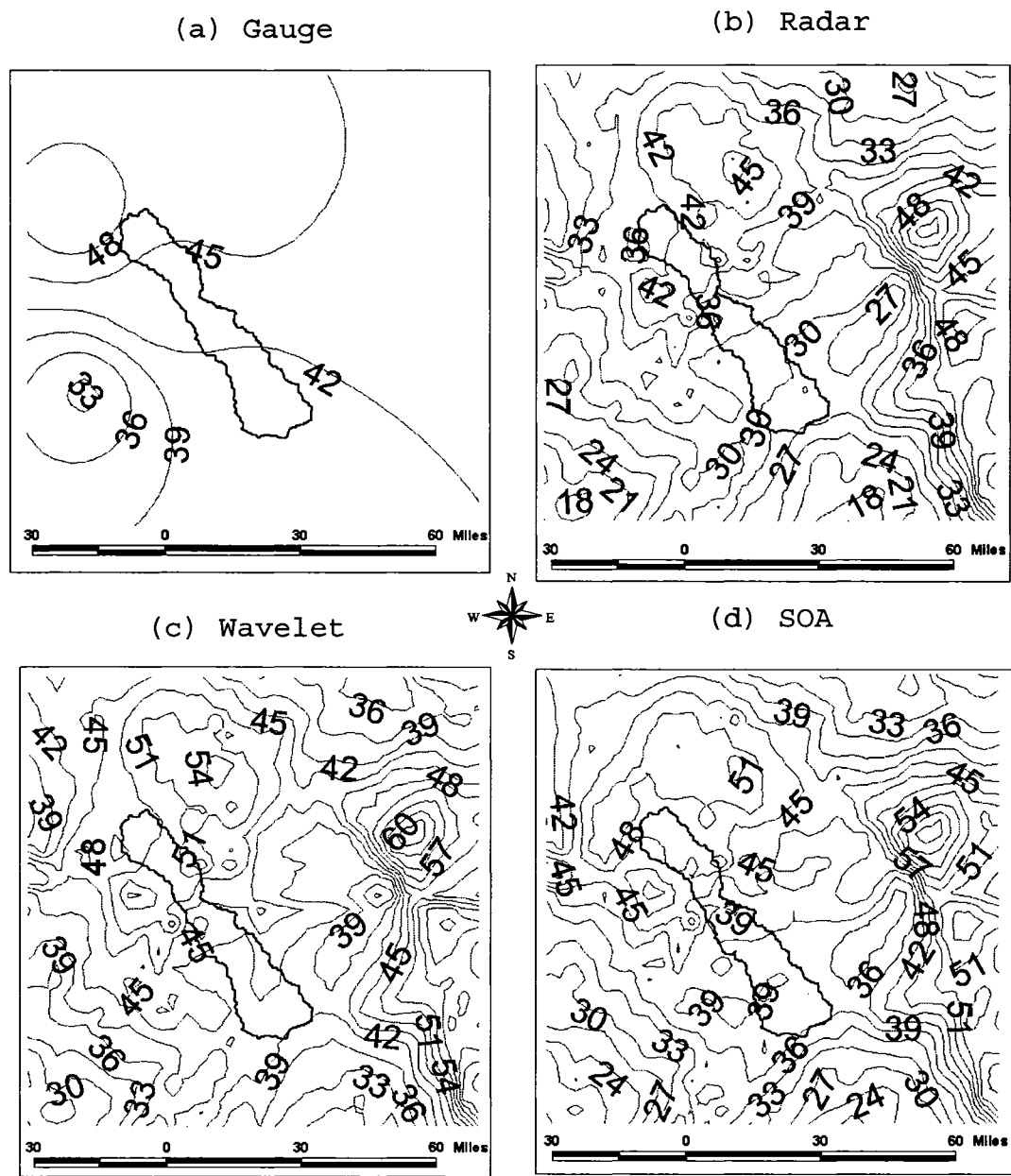


Figure 3.9 Total rainfall contour map (mm) for storm # 9 of October 12 (08:00) – 13 (02:00), 1997 with a 3.0 mm contour interval. The original gauge, radar, and radar-gauge merged rainfall fields using wavelet and statistical objective analysis (SOA) schemes are shown from (a) through (d), respectively.

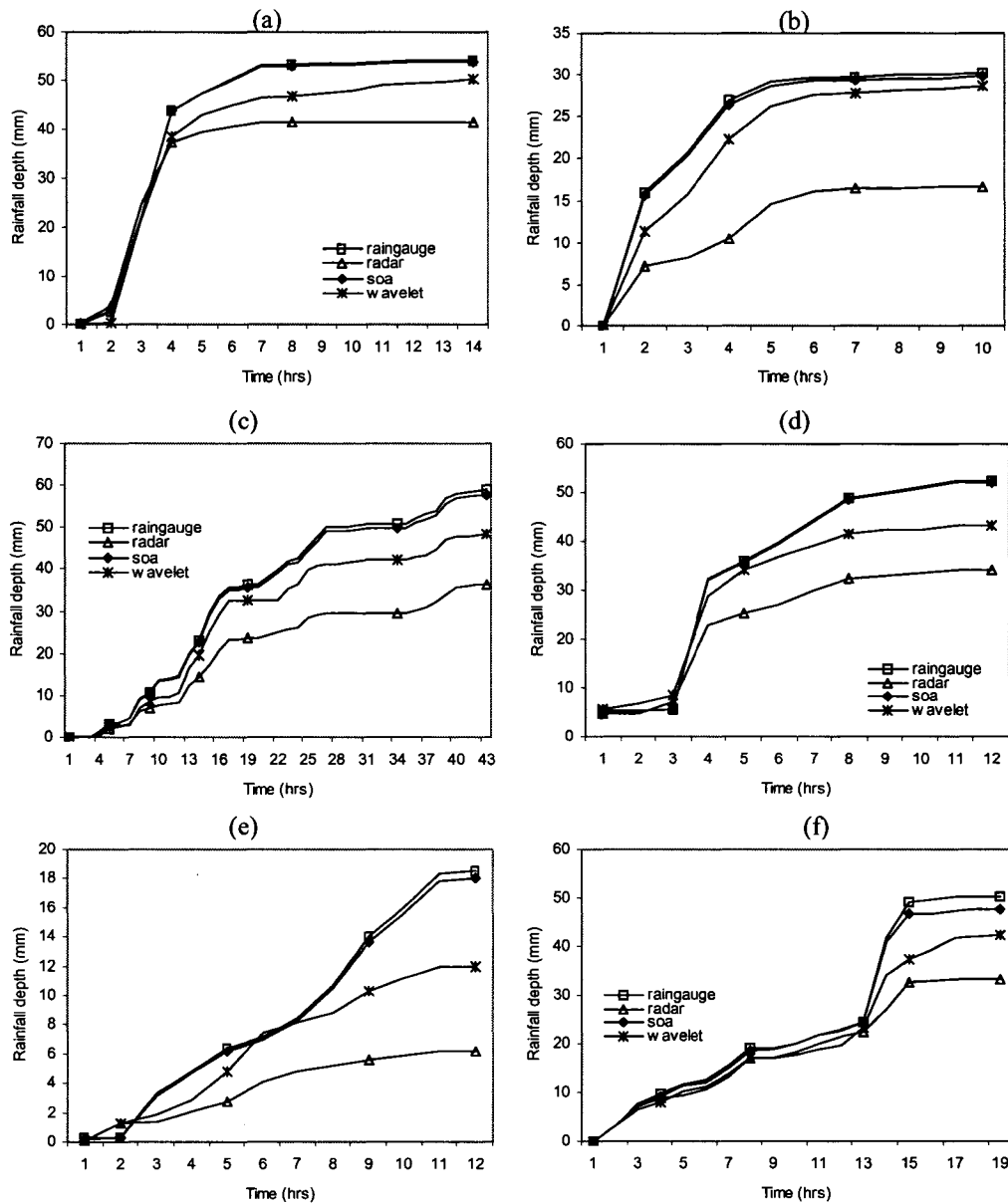


Figure 3.10 Cumulative rainfall plots for all the six storms used in the radar-gauge merging analysis at the raingauge showing the largest radar underestimation of rainfall (see Table 3.4): (a) storm # 8 (1994) at gauge # 2, (b) storm # 10 (1994) at gauge # 2, (c) storm # 13 (1994) at gauge # 5, (d) storm # 1 (1995) at gauge # 3, (e) storm # 2 (1996) at gauge # 2, and (f) storm # 9 (1997) at gauge # 1.

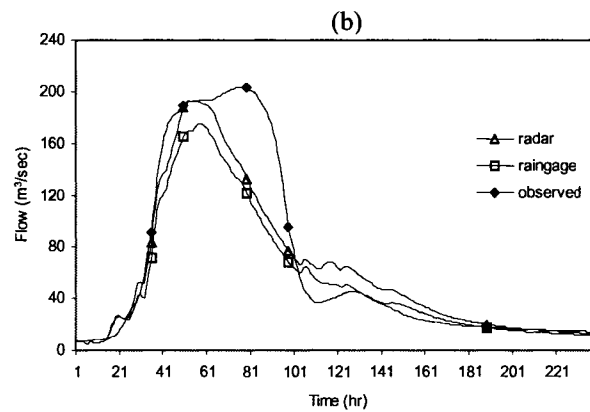
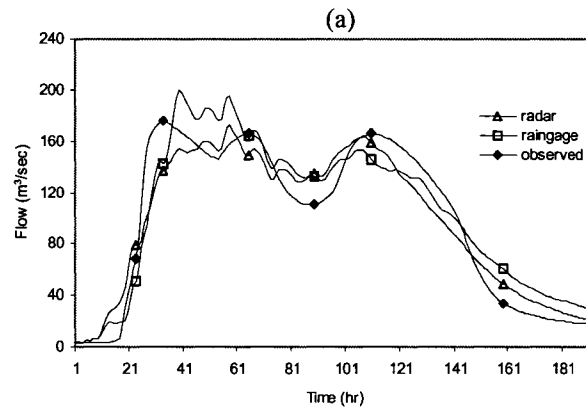


Figure 3.11 Observed streamflow hydrographs simulated by DPHM-RS model forced by gauged and radar rainfall data during (a) model calibration using storm # 2 of January 4 (00:00) – 11 (23:00), 1998, (b) model validation using storm # 6 of March 15 (00:00) – 24 (23:00), 1998.

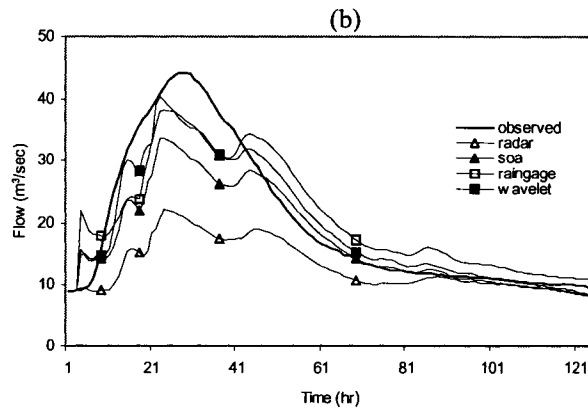
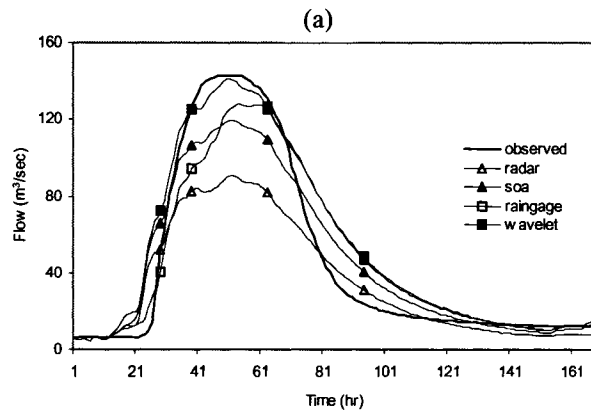


Figure 3.12 Observed streamflow hydrographs simulated by DPHM-RS model forced with gauged, radar, and radar-gauge merged rainfall data for (a) storm # 13 of December 8 (00:00) – 14 (23:00), 1994, and (b) storm # 1 of January 26 (00:00) – 31 (23:00), 1995.

Chapter 4

Influence of Storm Size and Spatial Variability on Radar Data Accuracy and Streamflow Prediction

4.1 Introduction

To account for spatial variability of meteorological and hydrologic variables, distributed and semi-distributed hydrologic models have evolved in the last two decades. This happened as a result of spatially distributed data becoming more readily available through remote sensing. However, their applications are still limited by a general lack of spatially distributed data of appropriate resolution and reliable quality, and the uncertainty associated with parameter estimations for distributed models. For instance, due to a lack of distributed precipitation data, distributed and semi-distributed hydrologic models still used point gauge measurements as the input function (e.g., Biftu and Gan, 2001). This means an under utilization of a complex model, or a mismatch between model complexity and the primary forcing function (precipitation) for computing basin-scale water fluxes (Boyle et al., 2001).

Several studies have been conducted in the past addressing the sensitivity of streamflow hydrographs to the spatial and temporal variations in precipitation. Many of these studies examined the effects of raingauge sampling errors on the outflow hydrograph. Wilson et al. (1979) showed that the spatial distribution of rainfall had a marked influence on the streamflow hydrograph from a small catchment. On the other hand, Beven and Hornberger (1982) stated that rainfall spatial patterns have only a secondary effect on streamflow hydrographs. For a small watershed, Krajewski et al. (1991) found a higher sensitivity to the temporal resolution of precipitation than to the spatial resolution. Ogden and Julien (1994) and Shah et al. (1996) also investigated the effects of precipitation variability on hydrologic simulations. It is interesting to note that most of these studies were based on synthetically generated precipitation and streamflow data due to a lack of appropriate observed data.

With the deployment of weather radars such as the Weather Surveillance Radar - 1988 Doppler (WSR-88D) network of USA (Klazura and Imy, 1993), it is now possible to map detailed precipitation fields due to radar's large aerial coverage, refined spatial and temporal resolutions, and the acquisition of data from some remote areas not quite accessible by ground. However, the accuracy of WSR-88D radar rainfall estimates is influenced by storm type (e.g., convective and stratiform) and storm size (e.g., Smith et al., 1996; Stellman et al., 2001), uncertainties in converting radar echoes to rainfall estimates, data processing problems, and radar range effects (e.g., Smith et al., 1996; Pereira et al., 1998; Stellman et al., 2001). For instance, Stellman et al. (2001) found that for Georgia watersheds, the Mean Areal Precipitation (MAP) derived from WSR-88D stage III data was slightly more than MAP derived from gauge during summer (convective storms), but underestimated the gauge MAP by about 50% during winter (stratiform storms). Jayakrishnan et al. (2004) did a similar assessment of WSR-88D stage III radar data at 24-hour accumulations over the Texas-Gulf basin for 1995-1999. They found that

the radar data underestimated the five-year precipitation at vast majority of the 545 rain gauges tested in their study. They recommended that the quality of stage III radar rainfall should be assessed using rain gauge measurements and necessary improvement be made before applying them in hydrologic studies.

The findings by Jayakrishnan et al. (2004) and references therein suggests that, the bias correction using raingauge data applied to produce WSR-88D stage III rainfall data may not be adequate. This can be attributed to correcting the bias of radar data using sparsely spaced point raingauge data, difficulty of identifying rainfall type resulting in applying wrong bias adjustment factors, georeferencing errors, and data processing errors such as averaging of overlapping radar data. Therefore, it seems beneficial assessing the accuracy of WSR-88D stage III radar rainfall data by comparing its simulated hydrographs with the observed.

There are conflicting views regarding the potential impact of radar rainfall errors in hydrologic modeling. For instance, Numez (1985) argued that errors in precipitation input to a hydrologic (or rainfall-runoff) model would result in significant errors in estimated runoff. Wyss et al. (1990) suggested that runoff prediction errors due to radar rainfall errors are less significant than errors due to rainfall-runoff transformation or modeling errors. Winchell et al. (1998) stated that there is not yet a consensus on the effects of radar data uncertainty on hydrologic modeling, nor has the topic received adequate attention, for most of the research on radar rainfall uncertainty has been to compare radar with their raingauge counterparts without analyzing their influence on basin-scale hydrologic simulations (e.g., Smith et al., 1996; Stellman et al., 2001; Jayakrishnan et al., 2004). Borga (2002) reported that, even though there are problems separating uncertainty in radar rainfall data from possible errors in hydrologic models, hydrologic modeling remains a viable approach to assess the suitability of radar over gauge rainfall data in basin hydrologic studies.

In view of the aforementioned issues, this study applies a semi-Distributed Physically based Hydrologic Model using Remote Sensing (DPHM-RS) of Biftu and Gan (2001, 2004) to address the following issues:

- (1) the effect of storm type and size on WSR-88D stage III radar rainfall data's accuracy and simulated water fluxes,
- (2) the effect of rainfall spatial variability on streamflow prediction, and
- (3) the effect of hydrologic modeling resolution (related to the spatial averaging of rainfall) on the resultant estimated streamflow.

This study is carried out in Blue River Basin (BRB) (Figure 4.1) using hourly WSR-88D stage III radar rainfall data and rain gauge data of Oklahoma Mesonet in event basis. The DPHM-RS model was selected partly because it is designed to assimilate radar rainfall data, and by sub-dividing a basin into an adequate number of sub-basins (Figure 4.1b), the effect of spatial variability can be effectively accounted for without incurring an excessive demand for input data and unnecessary computations. Table 4.1 shows the details of the six selected storm/flood events used in this analysis, subjectively categorized as large if $Q_{peak} \geq 150m^3/sec$, medium if $50 \leq Q_{peak} < 150m^3/sec$, and small if $Q_{peak} < 50m^3/sec$. From here onwards, the term “radar rainfall data” or “radar data” will mostly be used to refer to “WSR-88D stage III radar rainfall data”.

4.2 Study Site and Data Description

The Blue River Basin (BRB) of South Central Oklahoma (USA) (Figure 4.1a) is used as the study site partly because it is not regulated. BRB has a relatively flat terrain with elevation ranging from 153 to 350m above mean sea level. The total catchment area is 1233 km², and the major soil groups are clay and loam mixed with sand or silt (see Table 4.2). Woody Savannah is the dominant vegetation occupying almost 80% of the basin (see Table 4.3). The climate of this region is dominated by

frontal precipitation associated with large synoptic scale low-pressure systems during the fall and winter, with intense convective activity during spring and early summer. The average annual precipitation ranges from about 400mm in the extreme western panhandle to 1420mm in the southeastern corner of the State (Frederick et al., 1977). In winter, Oklahoma lies in the southern range of the polar jet stream and the northern range of the subtropical jet stream, leading to extremely variable temperature, precipitation, and strong winds. The January temperature ranges from a daytime high of 20⁰C to a nighttime low well below zero.

Digital elevation map (DEM) and stream network were used in subdividing the basin into 7 sub-basins (Figure 4.1b). Slope, flow direction, flow accumulation, mean elevation, and topographic soil index at each grid cell of 100m square resolutions were also derived from DEM data. The land use/cover data were derived from the vegetation data (1-Km resolution) of NASA LDAS (Land Data Assimilation Systems) and the leaf area index (LAI) was derived from the monthly Greenness Fraction data (~12-Km resolution) of NOAA-AVHRR data. Soil properties were derived from the DMIP (Distributed Model Inter-comparison Project) soil texture data (1-km resolution) and soil properties table of Rawls and Brankensiek (1985). The channel cross-sections for BRB were taken from the DMIP database.

In BRB there is ready access to operational WSR-88D radar rainfall data, and the Oklahoma Mesonet is a real-time environmental monitoring network that provides data necessary for driving the semi-distributed, physically based hydrologic (DPHM-RS) model. The BRB is within the Arkansas-Red Basin River Forecast Center (ABRFC) and five WSR-88Ds located in Oklahoma, Texas, and Arkansas provides coverage to BRB (Figure 4.1a). The operational radar stage III data at a spatial and time resolution of 4x4 km and 1-hour respectively, were transformed from radar reflectivity in three steps as described in Chapter 3 Section 3.2. The WSR-88D stage III precipitation data from DMIP were provided for the entire

ABRFC region. Using GIS Arc/Info, each hourly rainfall map was clipped to a 32 x 32 pixels window at 4 km x 4 km pixel resolution covering the BRB and its proximity.

The hourly gauge rainfall data were obtained from 6 Oklahoma Mesonet stations located around the basin (see Figure 4.1b). The Oklahoma Mesonet uses tipping bucket raingauges to measure rainfall accumulation at 5-min time intervals. The final data are accumulated to hourly time step. The point gauge rainfall data were interpolated to radar's grid points (Figure 4.1c) by using Gandin's (1963) optimal interpolation described in details in Chapter 3 Section 3.5.2.3. The corresponding hourly-observed streamflow data at the basin outlet stream-gauging station (Figure 4.1b) were obtained from the U.S. Geological Survey (USGS).

4.3 Streamflow Prediction Using DPHM-RS Model

The streamflow prediction using gauge and radar rainfall data was carried out through a semi-Distributed, Physically based, Hydrologic Model using Remote Sensing (DPHM-RS). DPHM-RS is divided into six components: interception, evapotranspiration (ET), soil moisture, subsurface flow, surface flow, and channel routing (Figure 4.2). The Rutter interception model (Rutter et al., 1971) is used to model rainfall interception, and the two-source model of Shuttleworth and Gurney (1990) is used to estimate the actual ET based on the amount of sensible and latent heat fluxes available at three layers (above canopy, within canopy, and at the soil). Land surface evaporation and vegetation canopy transpiration are computed separately. A three-layer (active, transmission and saturated layers) soil profile is used to model the soil moisture. A uniform soil type is used for the active layer (usually ranges between 15 and 30cm deep), transmission, and saturated zones. The active layer simulates the rapid changes of soil moisture under high frequency atmospheric forcing, while the transmission zone simulates the relatively slow, seasonal soil moisture behavior. To model the saturated subsurface flow, the spatial

variability of topography, soil properties, and the average water table depth for each sub-basin, in terms of the local soil index, is parameterized by the wetness or topographic soil index of Sivapalan et al (1987). Unsaturated soil's water transport is assumed vertical and its lower boundary is at the top of the capillary fringe.

DPHM-RS can simulate two types of runoff generation mechanisms: (1) Hortonian or infiltration-excess and (2) saturation-excess, for vegetated and bare land separately. The surface runoff for each of the 7 sub-basins of BRB (Figure 4.1b) is based on its average response function derived by the kinematic wave equation. To obtain this response function, a reference rainfall excess of 1cm depth is supplied to all grid cells within each sub-basin for one time step. Then for each grid cell, the kinematic wave function is applied and the flow is routed from cell to cell based on eight possible flow directions until the reference rainfall excess for each sub-basin is exhausted. The response functions of the 7 sub-basins vary widely (Figure 4.3), e.g., the response function of sub-basin 3 has a quick hydrograph peak of $22.1\text{m}^3/\text{sec}$, followed by a few smaller peaks of about $4\text{m}^3/\text{sec}$ because of its narrow shape and the presence of few channels at its mid to upstream portion (see Figure 4.1b) which means a quick transfer of generated runoff from this sub-basin to the main channel. The latter smaller peaks can be associated with the small average slope of this sub-basin and the increased channel network from mid to downstream portion (Figure 4.1b). The bi-modal response functions for sub-basins 6 and 7 are caused by the presence of large tributaries contributing flows to the main channel (Figure 4.1b). Routing through the drainage network is accomplished by the Muskingum-Cunge routing method whose variable parameters are obtained by an iterative four-point approach (Ponce and Yevjevich, 1978).

The DPHM-RS model input data are summarized in Table 4.4. The Exponential decrease parameter for saturated hydraulic conductivity (F), and surface & channel Manning roughness (n_m) are the only calibrated parameters and all of them have moderate model sensitivity (Table 1 in Biftu and Gan, 2001). The initial values of

these parameters were estimated based on land use classes or literature values and then were refined through calibration. The other parameters were either directly derived from field observation, satellite data, and literature. The simulations began with BRB at a “near wet” antecedent moisture condition (AMC), because the events selected were preceded by other storms. By using this “near wet” AMC, we expect more dynamic responses from BRB to rainstorms. Relatively dry AMC will result in passive hydrologic responses because a large portion of rainfall will first have to soak up the dry soil mantle before surface runoff can expect to occur.

4.4 Analysis of Results

The comparison of radar and gauge rainfall data estimated for BRB and the corresponding simulated water fluxes (i.e., soil moisture, evapotranspiration, and streamflow) are first presented, then the effect of rainfall spatial variability and hydrologic model resolution on streamflow prediction are discussed.

4.4.1 Comparison of Radar and Gauge Basin MAP over BRB

Because storm types of BRB are primarily season dependent, the data are grouped into three seasons, namely, winter - November, December, January, and February (NDJF); spring and early summer - March, April, May, and June (MAMJ); and late summer and fall - July, August, September, and October (JASO). The hourly mean areal precipitation (MAP) of BRB for gauge and radar data were computed by averaging the hourly rainfall values for the 57 grid points falling within BRB (see Figure 4.1c) from four years of hourly rainfall data, i.e., 1994, 1995, 1998, and 1999 from which the events in Table 4.1 were selected except 1999. Radar and gauge data are compared in terms of R^2 and Mean Field Bias (MFB), the ratio of cumulative radar to cumulative gauge data, i.e.,

$$MFB = \sum radar_data / \sum gauge_data .$$

Figure 4.4 shows the scatter plots for the NDJF, MAMJ, and JASO periods for gauge vs. radar data. Figures 4.4a to 4.4c clearly show a significant under-estimation of rainfall measurements by radar as compared to gauge for the NDJF period than those of MAMJ and JASO periods, as is also revealed by the lower R^2 for NDJF (0.52) as compared to MAMJ (0.72) and JASO (0.58). This is because NDJF represents winter dominated by shallow stratiform storm systems which radar tends to significantly underestimate. Even though in basin MAP the averaging of data can smooth out individual differences, the under-estimation of winter radar rainfall was still visible. During MAMJ generally dominated by convective storms (Frederick et al., 1977), radar and gauge data are much closer to each other (Figure 4.4b, $R^2 = 0.72$), which suggests that radar measures convective storms more accurately than stratiform storms.

The mixed scatter-plot and a lower R^2 (0.58) indicated by Figure 4.4c can be attributed to the possibility that both convective and stratiform storms were present in the JASO period because JASO includes both summer (July and August) and fall (September and October). Because radar tends to underestimate stratiform storms, data points falling well below the 45 degrees line seems to represent that of the fall season (September and October) when BRB might be dominated by stratiform storms.

In terms of MFB, the MFB for NDJF equals to 0.69 that represents a 31% under-estimation by the radar rainfall as compared to gauge rainfall. However, Figure 4.4b show that for MAMJ radar even reported slightly more rainfall than the gauge (MFB=1.03). For JASO the MFB for the radar vs. gauge data was 1.0 (Figure 4.4c). For MAMJ dominated by convective storms, an MFB >1 indicates that radar data tend to estimate more rainfall than gauge data when convective storms dominate. This is partly because in scanning such storms radar data are less affected by the radar range effect associated with the averaging of overlapping radar

bins, because such storms are not shallow as stratiform storms (e.g., Pereira et al., 1998). Beyond that, since convective storms are more highly variable spatially and radar has much denser sampling points than sparsely spaced rain gauges, we expect radar to measure such storms more accurately than gauge data. Because JASO seems to consist of both convective (JA) and stratiform (SO) storms, the effect of radar under-estimation of stratiform storms was more or less cancelled out by the over-estimation of convective storms, resulting in a MFB of 1.00.

4.4.2 Effect of Storm Type on Simulated Water Fluxes

The effect of driving DPHM-RS (Biftu and Gan, 2001, 2004) with different precipitation data and storm types are assessed in terms of simulated streamflow, evapotranspiration (ET), and soil moisture of the active layer on event basis. The results for soil moisture and ET are based on the combined simulations for seven sub-basins. Figure 4.5 shows the scatterplots for radar versus gauge rainfall, and the corresponding simulated soil moisture and ET for convective (Figures 4.5a to 4.5c) and stratiform (Figures 4.5d to 4.5f) storms. Rainfall plots indicates that radar reports 19% more rainfall than gauge for convective rainfall ($R^2 = 0.74$, MFB = 1.19) while for stratiform rainfall gauge reports considerable more rainfall (about 26%) than radar ($R^2 = 0.46$, MFB = 0.74). For convective storms, as expected soil moisture simulated from radar data was higher than that simulated from gauge data (Figure 4.5b), with R^2 of 0.97 and MFB of 1.01. For stratiform storms, the amount of soil moisture simulated from both data sources (Figure 4.5e) appear to be similar again with R^2 of 0.94 and MFB value of 0.99. The relatively large differences between radar and gauge rainfall (Figure 4.5d) did not result in much differences in the simulated soil moisture, except slightly more scatter points lying below the 45^o degree line.

For convective storms, MFB for rainfall was 1.19 (radar > gauge rainfall), yet ET simulated by radar data was slightly less than that for gauge data (Figure 4.5c), with MFB of 0.96, which is slightly less than the MFB for soil moisture of 1.01. This is

not quite as expected because more moisture should mean more ET. However, the difference between the two MFB is very small. For stratiform storms, gauge data resulted in slightly more ET than radar data (MFB=0.93) (Figure 4.5f).

The corresponding simulated streamflow shows a more sensitive response to radar and gauge rainfall data (scatterplots not shown), where for convective storms MFB was 1.32 because radar reported more rainfall than gauge, and vice versa for stratiform storms, where radar reported less rainfall than gauge with a MFB of 0.73. The result by DPHM-RS is expected because during a storm, we would expect a river basin to generally show more dynamic hydrologic response in terms of runoff generations than in terms of changes to soil moisture and ET (which should be relatively small because of high humidity), particularly for big storms that generate surface runoff. Therefore we should assess the effect of precipitation data accuracy on simulated water fluxes in terms of streamflow, not soil moisture or ET. Further, we don't have observed data for the latter.

DPHM-RS's simulated streamflow forced with rainfall input from gauge and radar data are analyzed further. The discrepancies between simulated and observed hydrographs are assessed in terms of % Error in peak discharge, % Error in total discharge volume, Time to peak discharge error, and the Efficiency coefficient (E_f) of Nash and Sutcliffe (1970).

The rainfall histograms for each sub-basin, and corresponding streamflow hydrographs for the six selected flood events simulated by DPHM-RS are shown in Figures 4.6 and 4.7 respectively. Once again, it can be observed that radar tend to report more rainfall than gauges for convective storms (Figures 4.6a to 4.6c), and less rainfall for stratiform storms (Figures 4.6d to 4.6f), with the exception of sub-basin 5 for the medium stratiform storm where radar reported more rainfall than gauges (Figure 4.6e), which can be attributed to: (i) the ability of the radar to record intense localized storms which can be entirely missed by the sparse rain gauges

(e.g., for sub-basin 5 the largest difference between grid point rainfall was 13.14mm/hr from radar data as compared to 0.59mm/hr from gauge data), and (ii) errors associated with data processing; for instance, for missing radar data values, a maximum-recorded rainfall at the gauge's site was assigned to all grid points falling within the gauge's radius of influence; also, it is possible that the MFB used to correct the radar data for this particular stratiform storm (Dec 8 – Dec 14, 1994) was not representative of the actual rainfall rate at sub-basin 5.

The inability of a few raingauges to capture the spatial variability of rainfall is reflected by the difference in time-to-peak-flow error, which is smaller for radar than for raingauge derived streamflow hydrographs (Table 4.5). In Figure 4.7c, which represents a small convective storm, both radar and raingauge data derived hydrographs substantially under-estimated the observed counterpart. Because the magnitude of backscattered signals (radar echoes) detected by radar is heavily dependent on the target size and the number of targets within the scanned volume (Smith et al., 1996), radar measurement of small storms tends to suffer from severe under-estimation problem. Also, tipping bucket raingauges tend to underestimate small and large rainfall rates because of wind and under-catch problems (Legates and DeLiberty, 1993). In Figures 4.6d and 4.7d, it seems that this large stratiform storm was associated with a deep convective system that resulted to a more accurate radar rainfall data, and its simulated streamflow hydrograph being more or less equal to that of gauged rainfall data.

4.4.3 Effect of Rainfall Spatial Variability on Streamflow Prediction

To assess the effect of spatial variations of rainfall on estimated streamflow, hydrographs derived from distributed radar rainfall are compared to lumped radar rainfall derived hydrographs for the six flood events (Figures 4.8a to 4.8f). Also, the effect of representing the rainfall for the whole catchment with radar rainfall series

of a few pixels (grids), which are sparsely distributed over the catchment area, is assessed. To accomplish this, three pixels were randomly selected within the Blue River Basin area and numbered from A to C (see Figure 4.1b). Figures 4.8a to 4.8f indicate the results of this assessment.

Even for the least spatially variable stratiform events 4, 5, and 6 (Figures 4.8d to 4.8f), the use of a few radar pixels to represent rainfall for the whole basin area can lead to significant errors. These results are totally in agreement with the findings of Wilson et al. (1979) and Pessoa et al. (1993) from their synthetic experiments. Additionally, the hydrographs derived from the fully distributed and averaged (lumped) radar rainfall data are not so different from one another. Thus for event studies, appropriate spatially averaged rainfall data (at hourly time step) seem adequate to drive the Blue River Basin.

4.4.4 Effect of Hydrologic Model Resolution on Streamflow Prediction

The influence of model resolution on streamflow hydrographs is analyzed by integration of sub-basins that exhibit similar response functions (i.e., sub-basins 1 and 2; 6 and 7) (see Figures 4.1b and 4.3) and comparison of the generated hydrographs. The model parameters were held constant for this case where 5 sub-basins represent the entire basin as it was for the 7 sub-basins scenario. Distributed radar and raingauge rainfall data were used to predict streamflows. Figures 4.9a to 4.9d show the results of the large and medium flood events (i.e., 1, 2, 4, and 5). It can be seen that model resolution has significant effect on the hydrological response of this basin, and the use of 5 sub-basins setup adopted in this case study could lead to a marked loss in hydrograph accuracy. This is partly because the hydraulic behavior for the processes involved in modeling the subsurface flow by DPHM-RS (i.e., groundwater rise and saturation from below) is highly affected by topographic differences. Our results agree with the findings of Krajewski et al. (1991) who, in a

synthetic experiment, reported a severe underestimation of flood peaks by the lumped model as compared to the distributed model.

In addition, the 5 sub-basins setup was used to assess whether the inability to predict the second observed peaks of events 1 and 2 can be attributed to the basin subdivisions and their response functions. Because the integrated sub-basins have bimodal response functions (see Figure 4.3), it was expected that it would enhance their influence in simulating hydrographs with a second peak. In order to raise the peak flow for the 5 sub-basins case obtained above, the infiltration was set to zero (Figures 4.10a to 4.10d), which in practice applies to runoff situations where either rainfall rates are much higher than the infiltration rates or soils are of very low permeability. There is now a second peak especially for event 2 (Figure 4.10b), however, this happened at the expense of less accurate recession limbs possibly because of the absence of infiltration to dampen the recession process.

When BRB was sub-divided into 13 and 20 sub-basins, the sub-basins' response functions became highly variable, with several relatively large and many small response functions (see Figure 4.11). The streamflow simulated by these response functions for the 13 and 20 sub-basins (results not shown) revealed that the few large response functions tended to dictate the shape of the resulting hydrographs, which turn out to be less representative of BRB's observed hydrographs. Even though using large number of sub-basins (e.g., 13 or 20 sub-basins) reduces the averaging effect of rainfall as compared to small number of sub-basins (such as the case of 5 sub-basins) that could give rise to non-representative rainfall, this advantage seems to be outweighed by the dominating effect of a few large response functions which can be undesirable.

Apparently there is a need to strive a balance or trade-off between a coarse subdivision of a river basin to avoid an excessive averaging effect of input rainfall data (to properly account for the spatial distribution of rainfall) or an overly refined sub-

division, which could lead to the dominating effect of a few large response functions. However, the effect of excessive averaging of input rainfall data seem to have less influence as shown in Section 4.4.3 where the simulated hydrograph from distributed and lumped (i.e., basin MAP) rainfall inputs were almost identical. On the basis of simulated hydrographs, subdividing the BRB into 7 sub-basins appears to be more or less the optimum.

4.5 Discussion and Conclusions

As the primary input for modeling basin hydrologic processes, it is essential that we use representative precipitation data. Even though radar data such as the WSR-88D radar rainfall data can generally capture the spatial variability of precipitation fields, the accuracy of its rainfall depth depends on the storm type (i.e., convective or stratiform) and size. The spatial variability of rainfall is known to decrease with increase in time and spatial scales, but there are few guidelines on what should be an appropriate choice of resolution for hydrologic modeling. Pessoa et al. (1993) showed that a time integration of less than 1 hour has no significant effect on the hydrological response. Here we used 1-hour time step (limitation from available data), so implicitly we assume that hourly time step represent accurate time distribution of rainfall. The results presented here may be limited by the choice of sizes of sub-basins and the time scale of available data.

On a whole, the degree of basin subdivision should be dependent on the terrain complexity, and the availability of landuse, soil and channel network data of appropriate resolution (e.g., Laurenson and Mein, 1988). This study used a trial and error approach based on the surface runoff response functions to determine the optimum sub-division for a river basin. Because basin hydrology is a dynamic outcome of terrain features, land use, soil properties, channel networks, and climate that interact with each other over a range of scales, there is likely no one universal

optimal resolution, even to the same basin subjected to a wide range of hydrologic experiences.

The published soil types and properties were assumed to be true in this study, but there are uncertainties associated with both the soil types and the soil properties defined in terms of soil type. Inaccuracies in channel cross sections can give rise to errors in hydrograph shape and timing, but this may not be a problem here because field-measured values were used. Overall, the conclusions of this research are:

- (a) The storm type (convective/stratiform) and size play a significant role in the accuracy of WSR-88D stage III radar rainfall estimates, and is reflected in the quality of simulated hydrographs in terms of peak flow and total runoff volume. The problem of radar underestimation of rainfall generally grows with a decrease in storm magnitude, even for convective storms.
- (b) To obtain reliable streamflow predictions, the spatial variability of rainfall should be properly accounted for. Point rainfall collected by rain gauges may not realistically represent the spatial precipitation field over a river basin particularly for convective storms that are highly variable spatially. This justifies the expensive and tedious effort to account for spatial variability of rainfall either via dense rain gauge monitoring networks (which is logistically impractical and expensive), radar meteorology, and meteorological satellites.
- (c) To produce reliable flood peaks, besides representative distributed rainfall data, the resolution of sub-basins divided from a river basin also plays an important role for effectively handling the spatial variability of rainfall, and for avoiding the dominating effects of certain large sub-basins on the overall hydrograph. It seems dividing BRB into 7 sub-basins is more or less the optimum resolution.

References

- Beven, K. J., and Hornberger, G. M. (1982), Assessing the effect of spatial pattern of precipitation in modeling stream flow hydrographs. *Water Resources Bulletin*, 823-829.
- Biftu, G. F., and Gan, T. Y. (2001), Semi-distributed, physically based, hydrologic modeling of the Paddle River Basin, Alberta, using remotely sensed data. *J. of Hydrology*, 244, 137-156.
- Biftu, G. F., and Gan, T. Y. (2004), Semi-distributed, Hydrologic Modeling of Dry Catchment with Remotely Sensed and Digital Terrain Elevation Data. *Int. J. of Remote Sensing*, 25(20), 4351-4379.
- Frederick, R. H., Miller, J. F., and Tracey, R. J. (1977), *Five to Sixty Minute Precipitation Frequency for the Eastern and Central U.S.*, NOAA Technical Memorandum NWS Hydro-35, Silver Springs, MD.
- Gandin, L. S. (1963), *Objective Analysis of Meteorological Fields*. Translated by R. Harding, Israel Program for Scientific Translation, 242pp.
- Klazura, G. E., and Imy, D. A. (1993), A description of the set of analysis products available from the NEXRAD WSR-88D system. *Bulletin of the American Meteorological Society*, 74, 1293-1311.
- Krajewski, W. F., Lakshmi, V., Georgakakos, K. P., and Jain, S. C. (1991), A monte-carlo study of rainfall sampling effect on a distributed catchment model. *Water Resources Research*, Vol. 27, No. 1, 119-128.
- Laurenson, E. M., and Mein, R. G. (1988), RORB-version 4 runoff routing program, user manual, Department of Civil Engineering, Monash University, Victoria, 186pp. In: Sun, X., Mein, R. G., Keenan, T. D., and Elliott, J. F., 2000. Flood estimation using radar and rain gauge data. *J. of Hydrology*, 239, 4-18.
- Legates, D. R., and DeLiberty, T. L. (1993), Measurement biases in the United States rain gauge network. *Water Resources Bulletin*, 29, 855-861.
- Nash, J. E., and Sutcliffe, J. V. (1970), River flow forecasting through conceptual models, 1. A discussion of principles. *J. of Hydrology*, 10, 282-290.

- Ogden, F. L., Julien, P. Y. (1994), Runoff model sensitivity to radar rainfall resolution. *J. of Hydrology*, 158, 1-18.
- Pereira Fo, A. J., Crawford, K. C., and Hartzell, C. L. (1998), Improving WSR-88D Hourly Rainfall Estimates, *Weather and Forecasting*, 13, 1016-1028.
- Pessoa, M. L., Bras, R. L., and Williams, E. R. (1993), Use of weather radar for flood forecasting in the Sieve river basin: a sensitivity analysis. *J. of Applied Meteorology*, 32 (3), 462-475.
- Ponce, V. M. and Yevjevich, V. (1978), Muskingum-Cunge method with variable parameters. *Pro. Am. Soc. Civil Eng.*, 104 ,HY12.
- Rawls, W. J., and Brakensiek, D. L. (1985), Prediction of Soil water properties for hydrologic modeling. *Water Management in the Eighties*, ASCE, 293-299.
- Rutter, A. J., Kershaw, K. A., Robins, P. C., Morton, A. J. (1971), A predictive model of rainfall interception in forests. I. Derivation of the model from observations in a plantation of Corsian pine. *Agricultural Meteorol.*, 9, 367-384.
- Shah, S. M. S., O'Connell, P. E., and Hosking, J. R. M. (1996), Modeling the effects of spatial variability in rainfall on catchment response. 2. Experiments with distributed and lumped models. *J. of Hydrology*, 175, 89-111.
- Shuttleworth, J. W., and Gurney, R. J. (1990), The theoretical relationship between foliage temperature and canopy resistance in sparse crops. *Q. J. R. Meteorological Society*, 116, 497-519.
- Sivapalan, M., Wood, E. F., and Beven, K. J. (1987), On hydrologic similarity, 2, a scaled model of storm runoff production. *Water Resources Research*, 23, 12, 2266-2278.
- Smith, J. A., Seo, D. J., Baeck, M. L., and Hudlow, M. D. (1996), An intercomparison study of NEXRAD precipitation estimations. *Water Resources Research*, 32, 7, 2035-2045.
- Stellman, K. M., Fuelberg, H. E., Garza, R., and Mullusky, M. (2001), An examination of Radar Rain Gauge-Derived Mean Aerial Precipitation over Georgia Watersheds. *Weather and Forecasting*, 16, 133-144.

Wilson, C. B., Valdes, J. B., and Rodriquez-Iturbe, I. (1979), On the Influence of the spatial distribution of rainfall on storm runoff. *Water Resources Research*, Vol 15(2), 321-328.

Table 4.1 Characteristics of the six selected flood/storm events used in the study.

Event	Storm Type	Storm Size	Period	Total rainfall depth (mm) ^a	Flood peak (m ³ /sec)
1	Convective	Large	March 15-24, 1998	81.93	202.65
2	Convective	Medium	March 13-22, 1995	67.31	148.15
3	Convective	Small	March 9-12, 1994	4.47	34.81
4	Stratiform	Large	January 4-11, 1998	124.85	175.84
5	Stratiform	Medium	December 8-14, 1994	48.55	142.35
6	Stratiform	Small	January 26-31, 1995	21.26	44.15

^a Total rainfall depth is computed from the Mean Areal Precipitation (MAP) for the entire basin using raingauge data

Table 4.2 Area, slope, and dominant soil types for each sub-basin of Blue River Basin.

Sub-basin #	Area [Km ²]	Soil type	Average Slope [%]
1	170.57	Silty clay loam	2.11
2	150.34	Silty clay loam	2.18
3	169.68	Silty clay loam	2.03
4	221.51	Sandy clay	2.19
5	188.41	Clay	2.20
6	204.25	Clay	2.30
7	130.37	Clay	2.62

Table 4.3 Percentage of different land cover types for each sub-basin of Blue River Basin.

Sub-basin #	Land use classes					
	Woody Savannah	Deciduous Broadleaf Forest	Water body	Grasslands	Croplands	Urban and Built-Up
1	91.57	2.45	0.01	3.74	1.42	0.81
2	88.73	0.01	0.01	11.24	0.01	0.01
3	86.43	10.53	0.01	1.36	1.67	0.01
4	68.70	28.02	0.01	0.01	3.23	0.01
5	83.46	16.28	0.01	0.01	0.25	0.01
6	78.34	16.72	0.01	0.33	1.50	3.10
7	48.00	51.97	0.01	0.01	0.01	0.01

Table 4.4 Input data of DPHM-RS model (modified from Biftu and Gan, 2001).

Data type	Parameters	Source
Topographic	Mean altitude, aspect, flow direction, surface slope, drainage network, and topographic soil index	DEM of USGS National Elevation Dataset (NED)
Land use	Spatial distribution of land use classes, surface albedo, and vegetation index	NOAA-AVHRR satellite data
Soil properties	Spatial distribution of soil types, antecedent moisture content, and soil hydraulic properties	U.S. State Soil Geographic (STATSGO)
Stream flow	Hourly stream flow data at the catchment outlet, channel cross-sections	U.S. Geological Survey (USGS)
Meteorological	Hourly: precipitation, short-wave radiation, air temperature, ground temperature, wind speed, and relative humidity	Oklahoma Mesonet stations and NWS Hydrology Laboratory (NWS-HL)

Table 4.5 Statistics of simulated hydrographs by DPHM-RS model for radar and gauge rainfall data.

Event	Data source	% Error in peak discharge	% Error in total discharge volume	Time to peak discharge error ^a	Efficiency (E_f)
1	Radar	-5.32	-6.48	-25	0.87
	Raingage	-14.07	-18.05	-20	0.82
2	Radar	-0.85	-7.88	-23	0.95
	Raingage	-13.36	-30.39	-24	0.79
3	Radar	-44.51	-40.73	-8	0.24
	Raingage	-61.14	-59.53	-19	-1.34
4	Radar	-1.72	-0.75	+25	0.92
	Raingage	+13.90	+5.52	+6	0.89
5	Radar	-36.24	-23.53	+4	0.75
	Raingage	-10.10	+3.55	+7	0.90
6	Radar	-49.95	-35.51	-3	0.15
	Raingage	-8.52	+4.88	-4	0.81

Negative error denotes underestimation

^a Underestimation of observed peak discharge led to large time to peak error (see Figure 4.7)

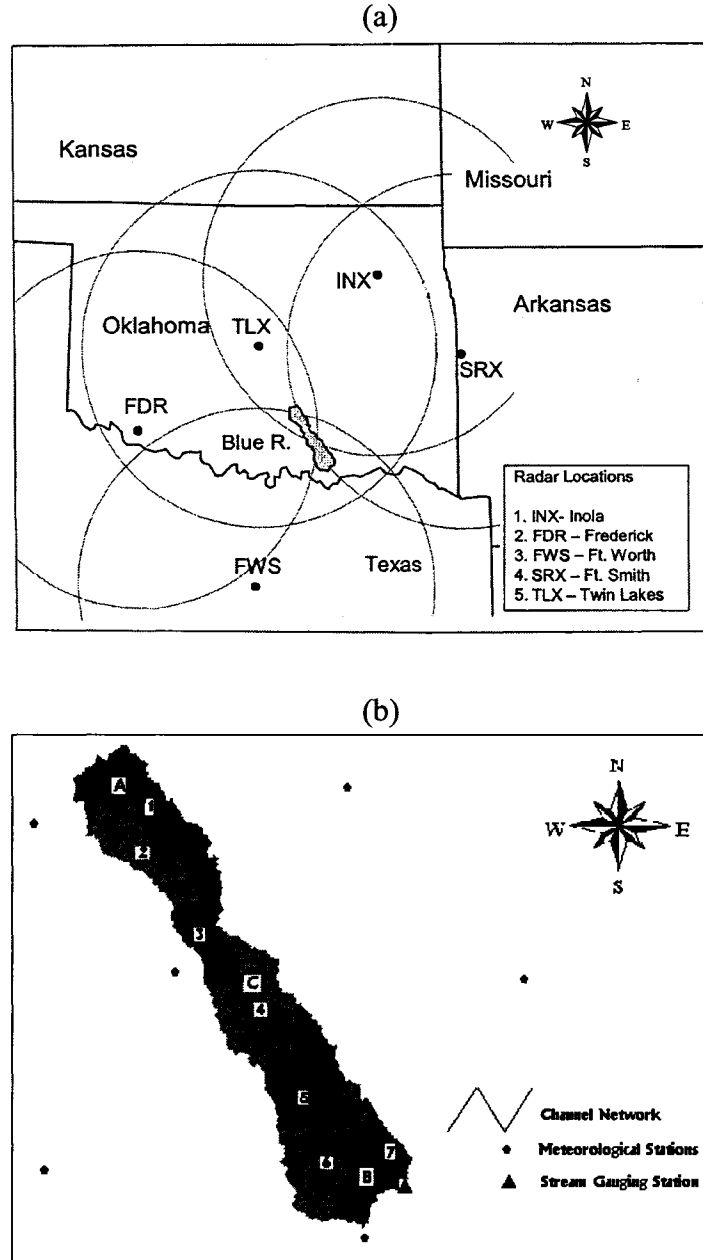


Figure 4.1 Map of Blue River Basin (BRB) indicating (a) WSR-88D radar sites providing coverage to BRB: Circles show the radar range rings with a radius of 230 km, (b) seven sub-basins (label 1-7) of BRB derived in this study: Letters A-C shows the locations of arbitrary selected grids used in rainfall spatial distribution analysis, and (c) 57 radar grid points falling within BRB.

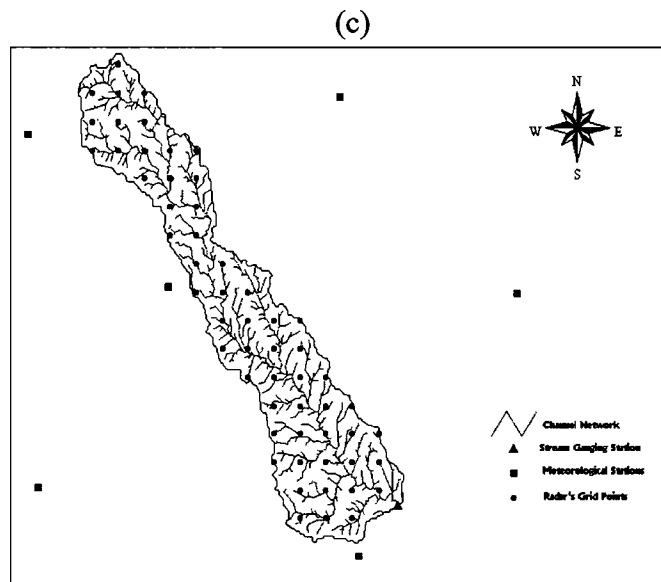


Figure 4.1 continued

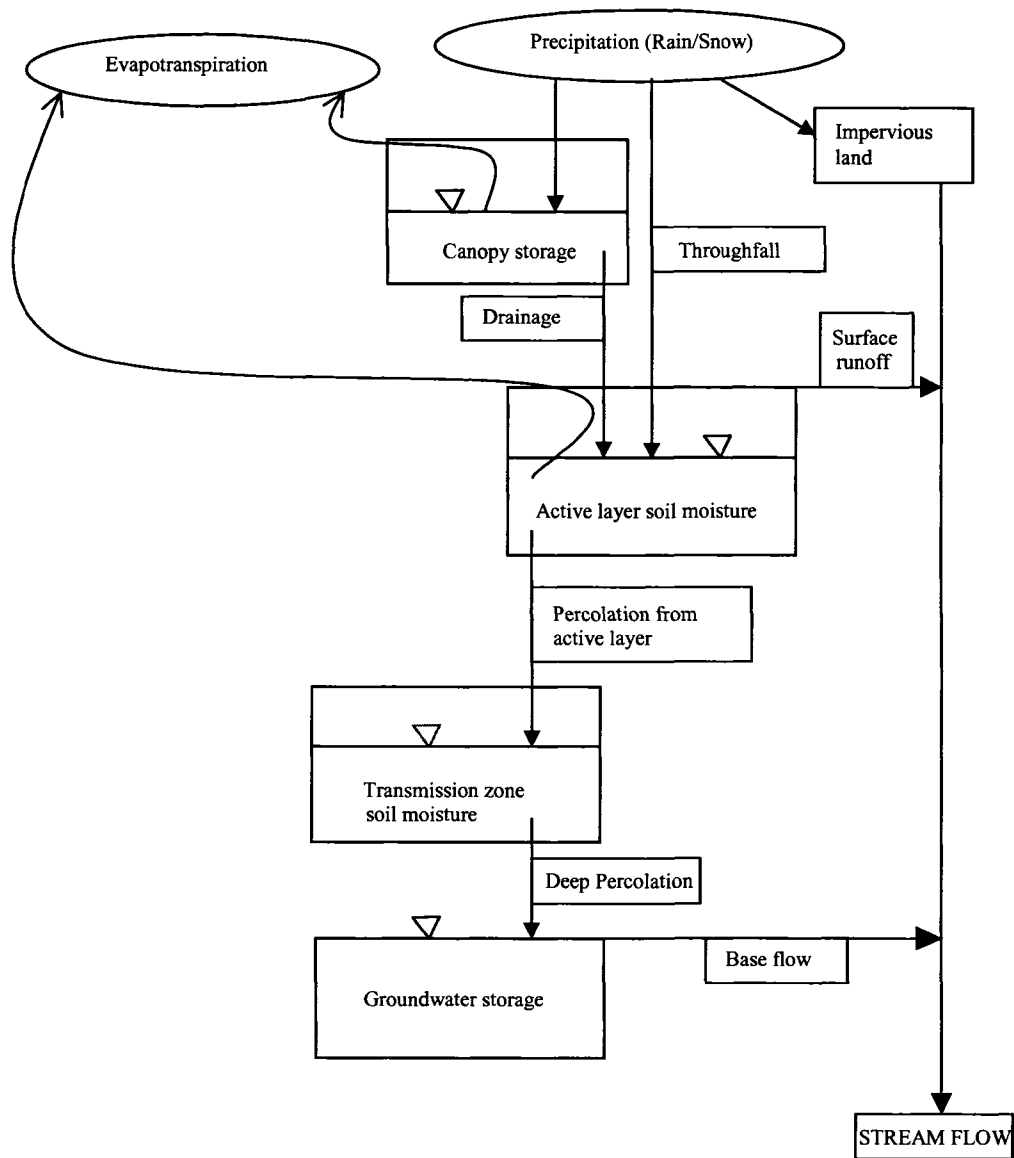


Figure 4.2 A schematic diagram showing the major components of DPHM-RS rainfall-runoff model.

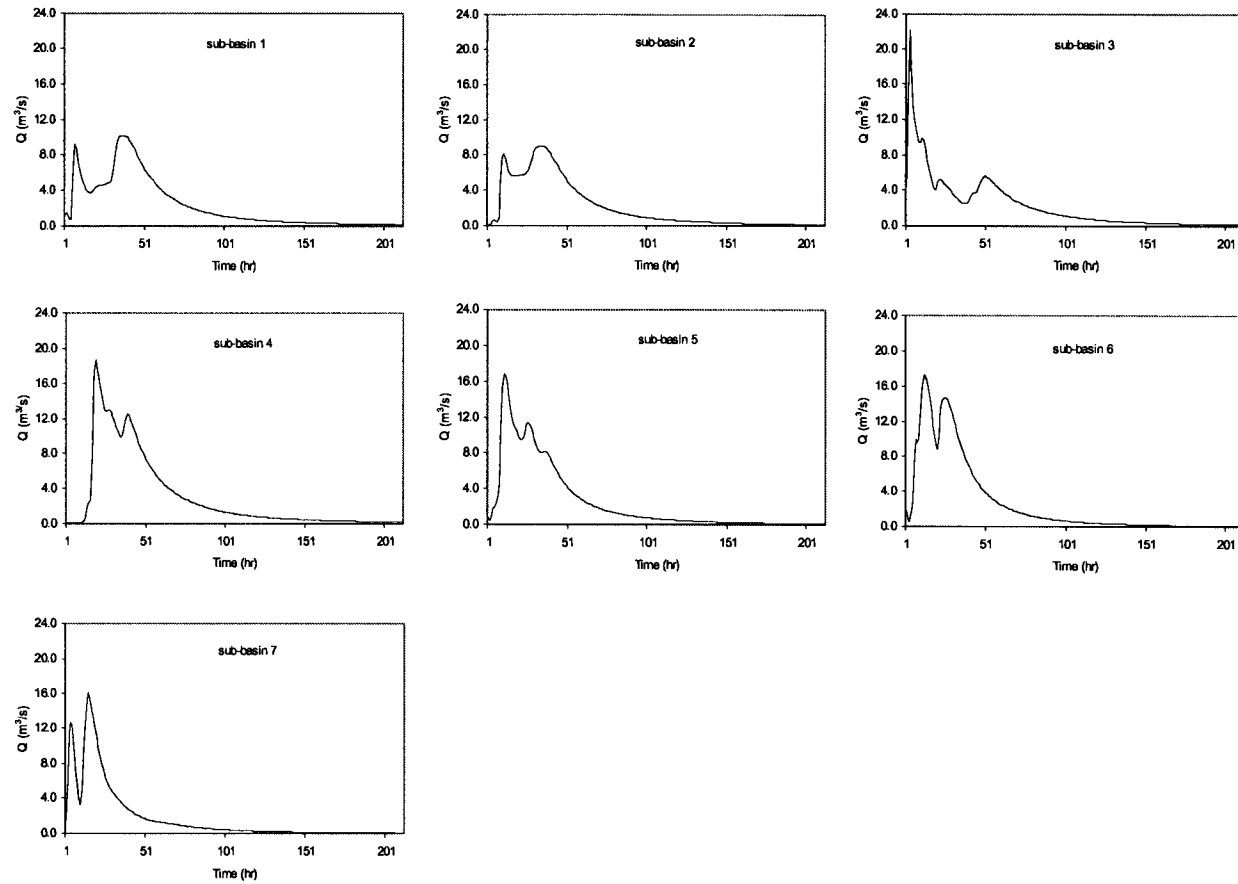


Figure 4.3 Kinematic surface runoff response functions for each of the seven sub-basins of Blue River Basin (see Figure 4.1b).

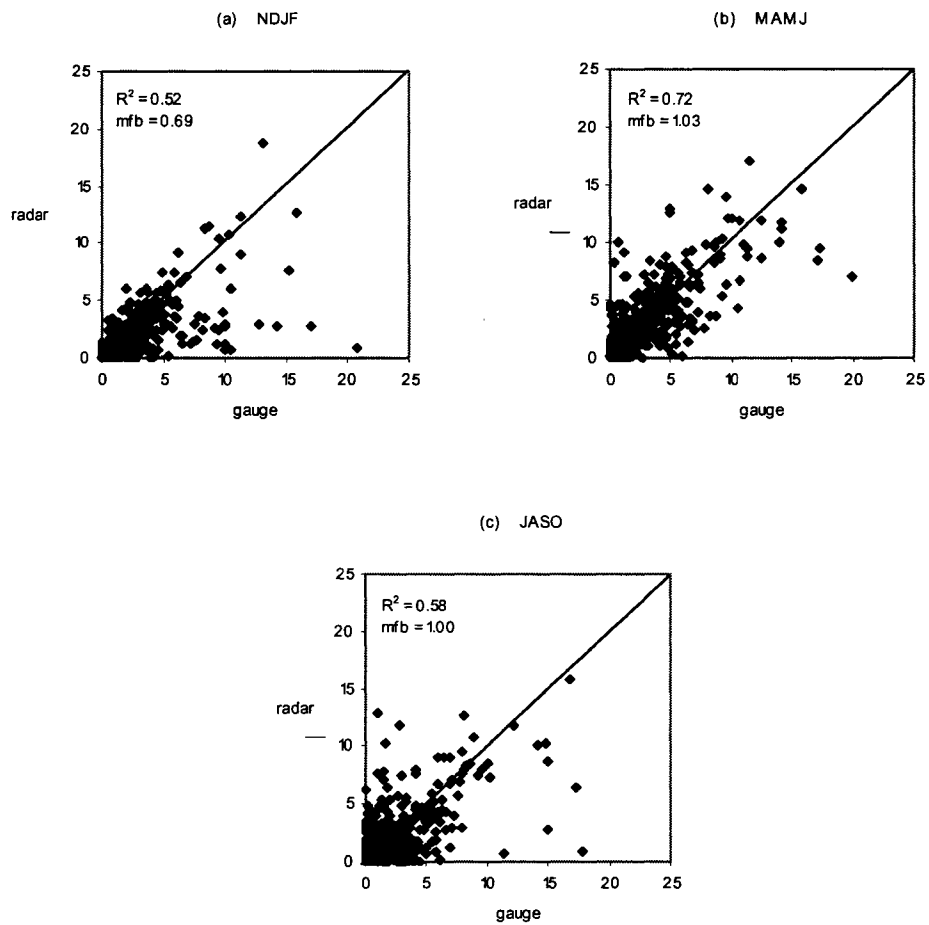


Figure 4.4 Comparison of hourly rainfall measurements (mm) from gauge and radar. Four years of hourly data were used: 1994, 1995, 1998, and 1999.

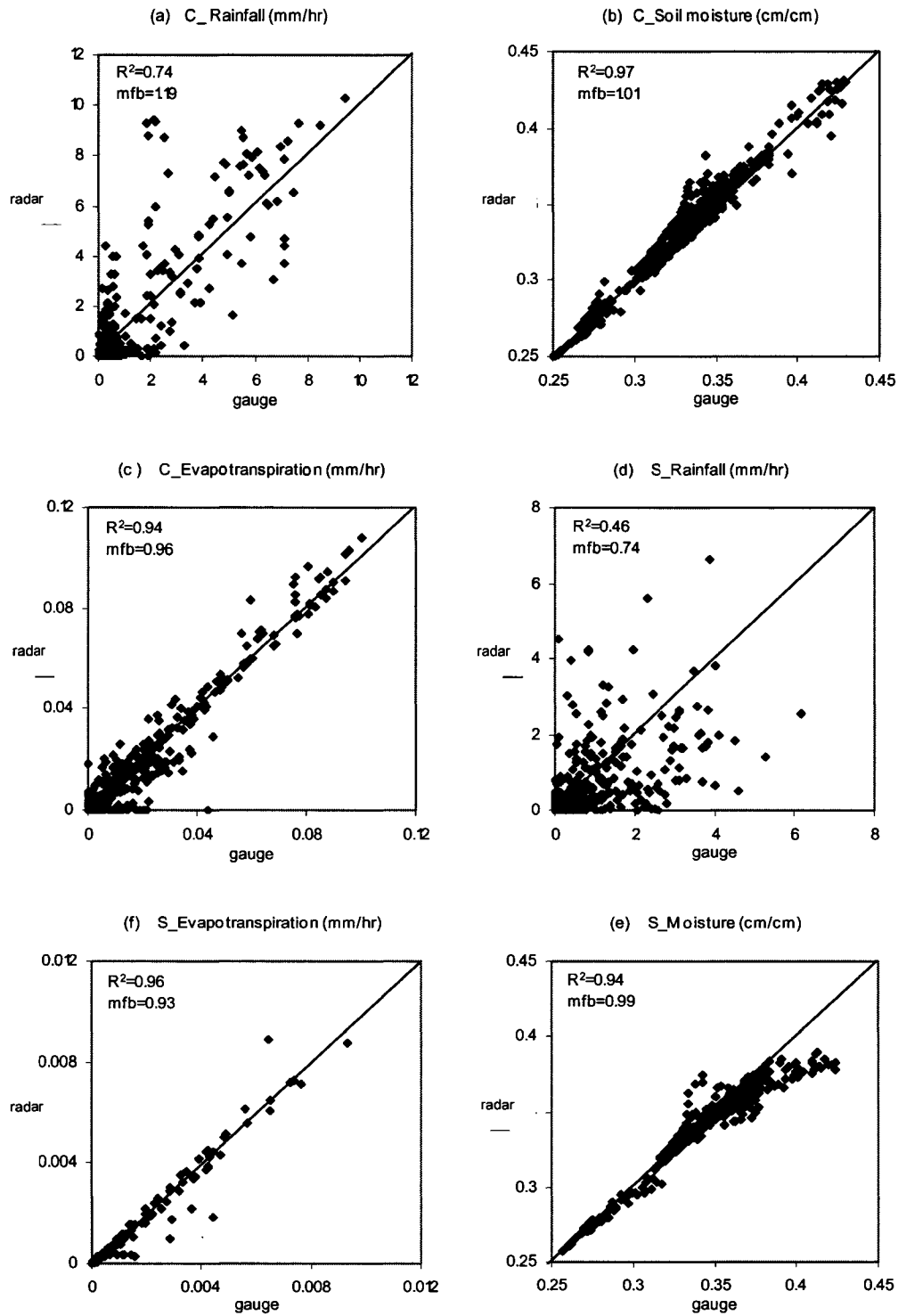


Figure 4.5 Scatterplots of radar and gauge hourly rainfall data and their corresponding simulated evapotranspiration and soil moisture at the active layer, where C= Convective storm, and S = Stratiform storm.

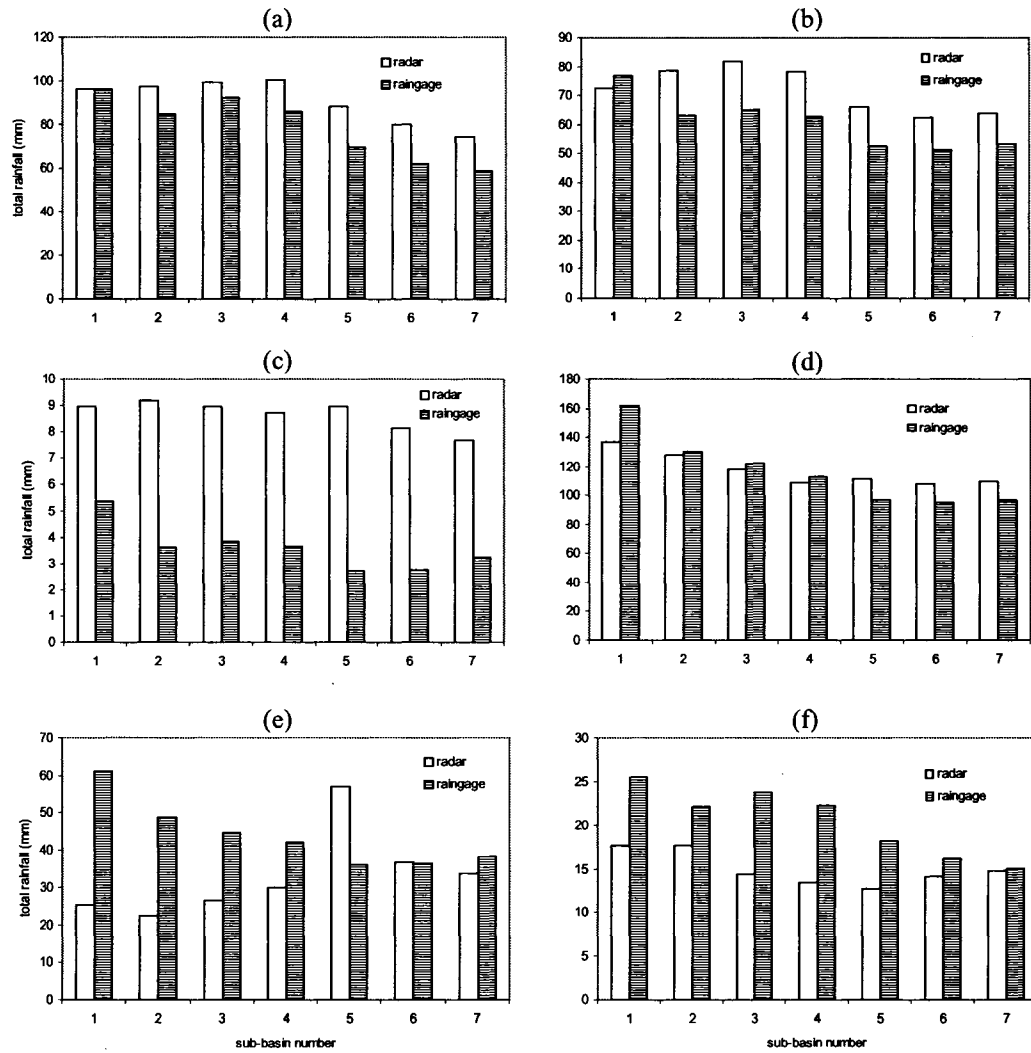


Figure 4.6 Total radar and gauged rainfall depths (mm) computed for seven sub-basins of Blue River Basin, for convective storms: (a) Event 1, (b) Event 2, (c) Event 3; and stratiform storms: (d) Event 4, (e) Event 5, and (f) Event 6.

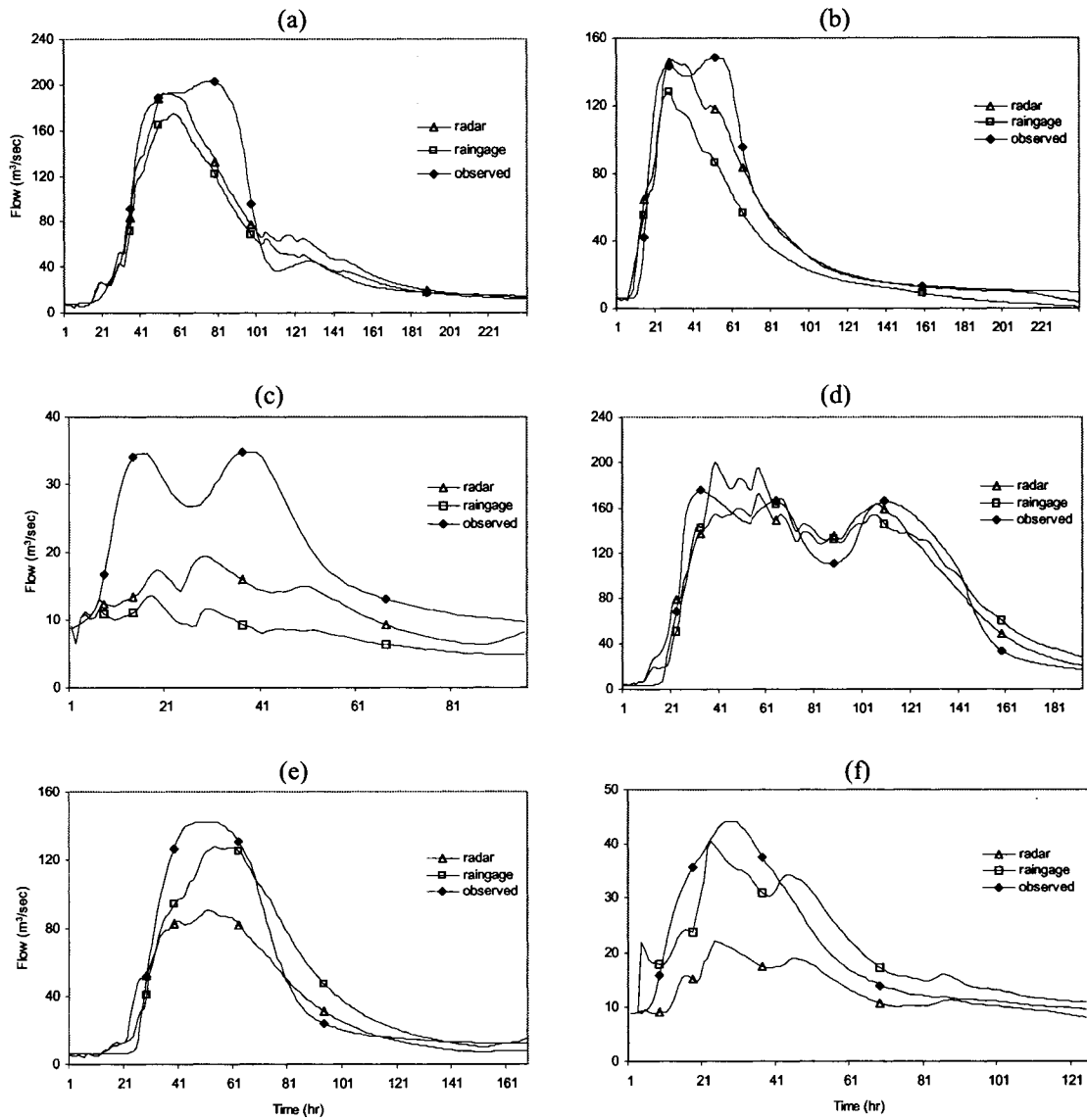


Figure 4.7 Observed streamflow hydrographs simulated by DPHM-RS model forced by gauged and radar rainfall data, for convective storms: (a) Event 1, (b) Event 2, (c) Event 3; and stratiform storms: (d) Event 4, (e) Event 5, and (f) Event 6.

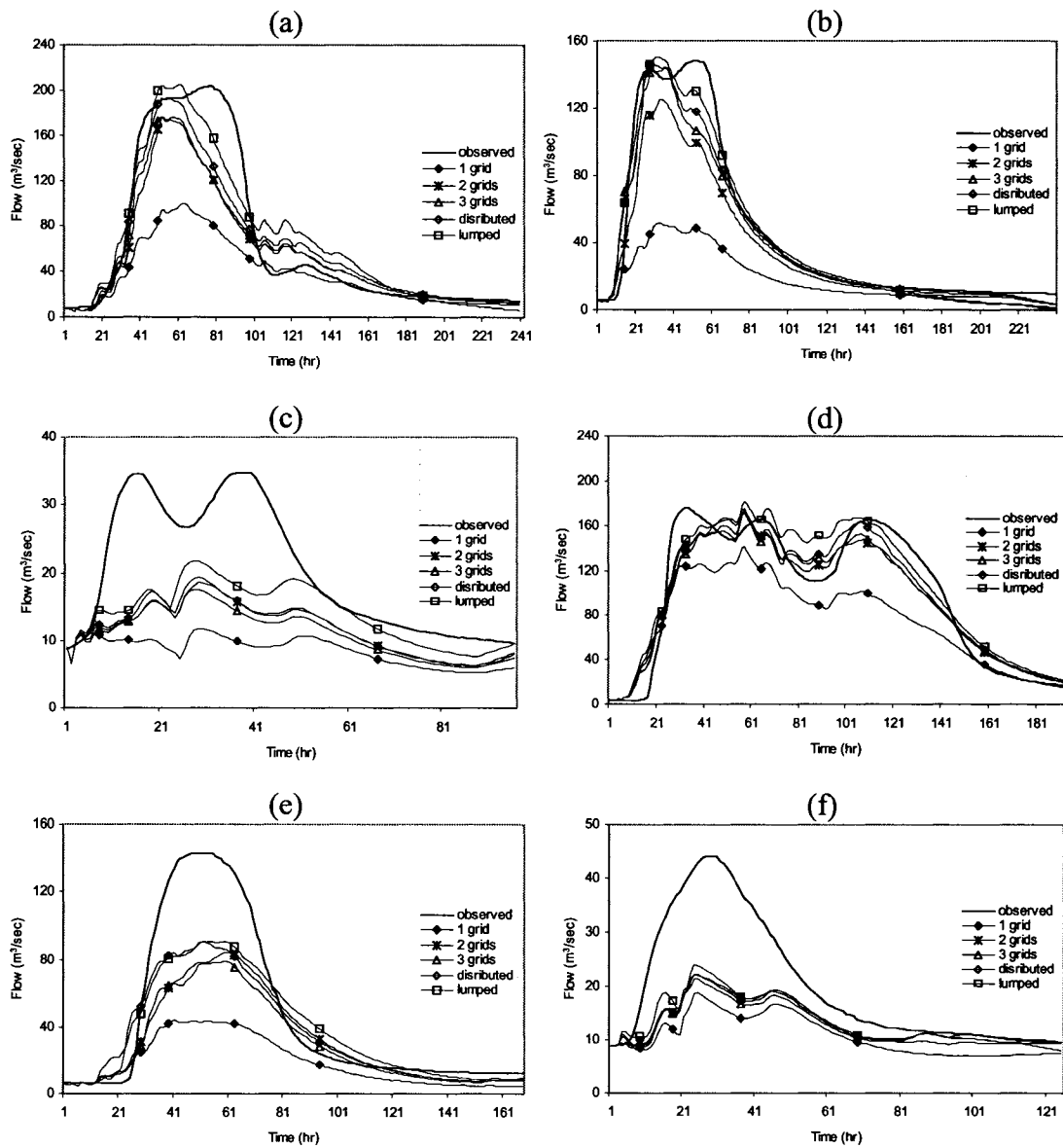


Figure 4.8 Streamflow prediction by radar inputs for averaged (lumped), fully distributed (distributed), one, two, and three grids for: convective storms: (a) Event 1, (b) Event 2, (c) Event 3; and stratiform storms: (d) Event 4, (e) Event 5, and (f) Event 6.

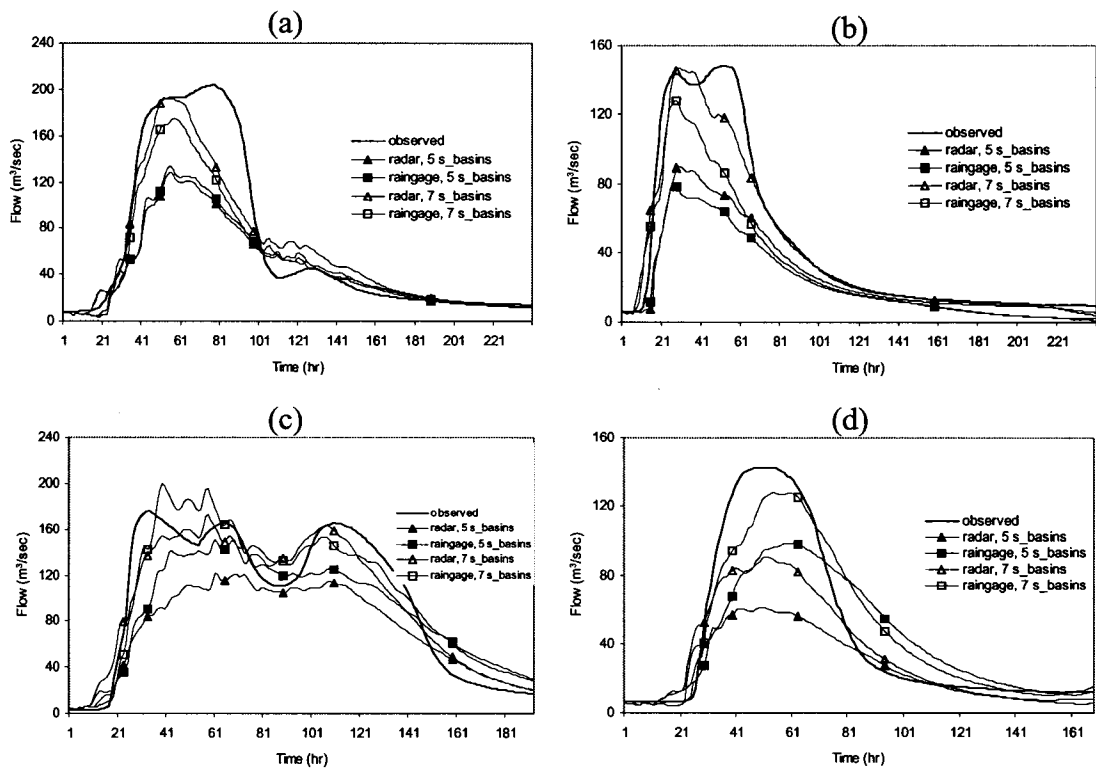


Figure 4.9 Streamflow prediction indicating hydrographs corresponding to radar and raingauge inputs for the case of 5 and 7 sub-basins for: convective storms: (a) Event 1, (b) Event 2; and stratiform storms: (c) Event 4, and (d) Event 5.

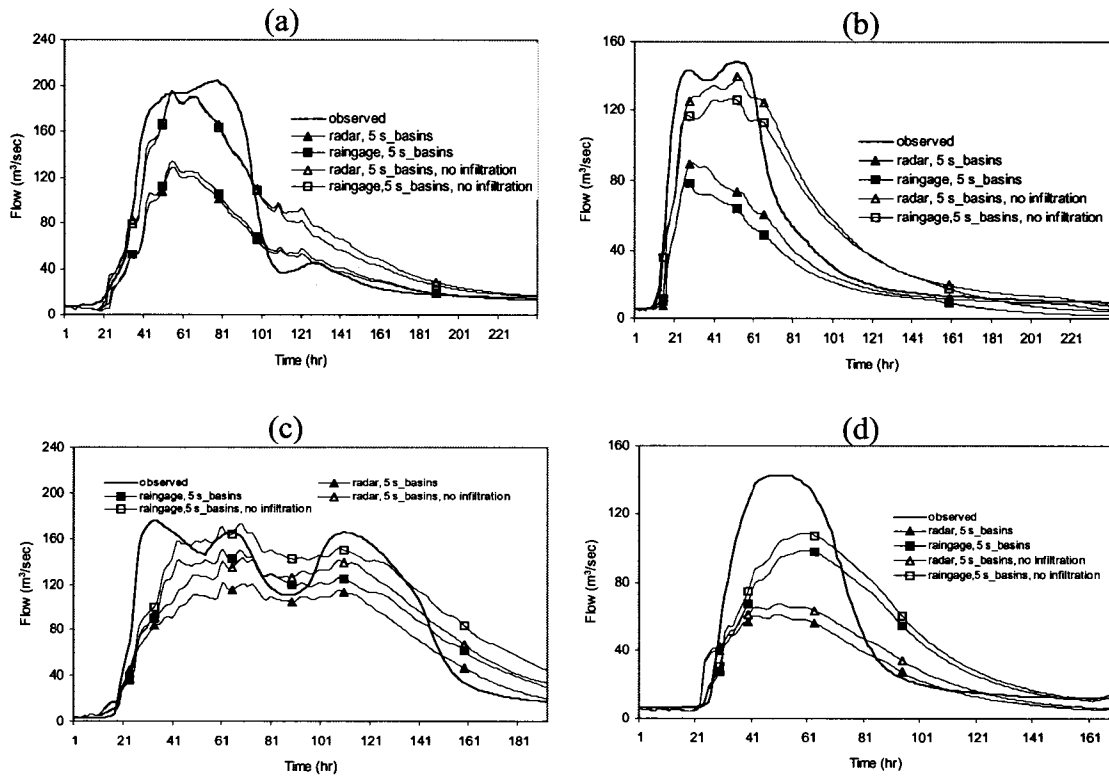


Figure 4.10 Peak flow prediction indicating hydrographs corresponding to radar and raingauge inputs for the case of 5 sub-basins for: convective storms: (a) Event 1, (b) Event 2; and stratiform storms: (c) Event 4, and (d) Event 5.

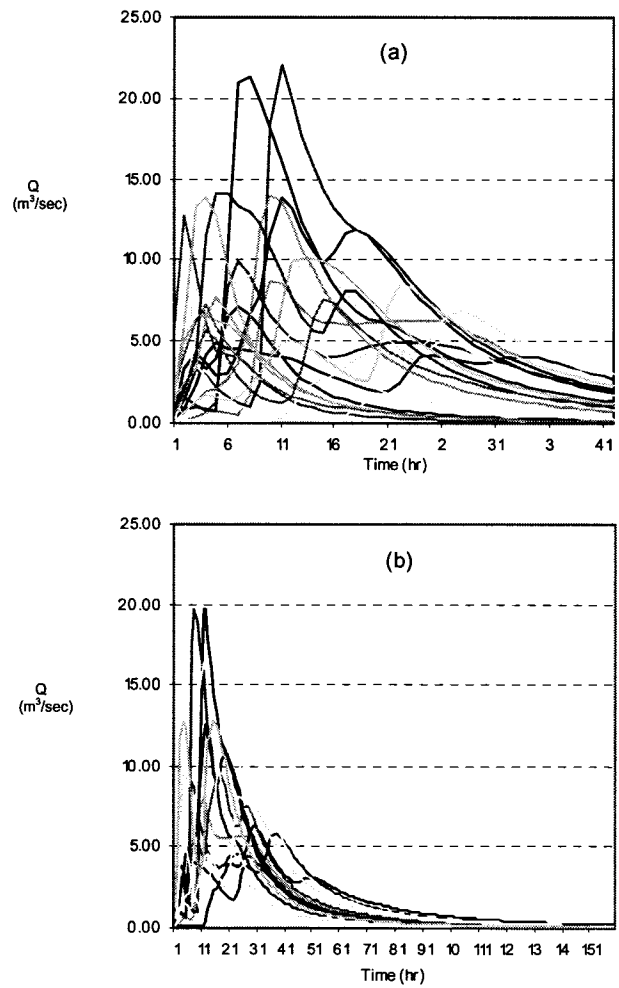


Figure 4.11 Kinematic surface runoff response functions of the Blue River Basin for the case of: (a) 20 sub-basins, (b) 13 sub-basins.

Chapter 5

Summary, Conclusions and Recommendations for Future Research

5.1 Summary and Conclusions

The Infrared-Microwave Rainfall Algorithm (IMRA) was developed to estimate rainfall field from satellite data for basin hydrologic modeling. IMRA is designed to utilize infrared (IR) brightness temperatures (TBs) as the main satellite information input. It uses the 243° K IR threshold temperature, Slope technique (ST) and Hessian technique (HT) to determine the IR image cloud-top temperature gradient for discriminating rain/no-rain pixels. IMRA allows for the adjustment of derived IR-rainfall estimates using microwave (MW) TBs information and spatial filtering/smoothing techniques. The testing of the IMRA algorithm was based on four months of data: June-July 2002 (relatively light rainfall) and August-September 2003 (relatively heavy rainfall) data. Detailed analysis of these datasets showed that the 2002 dataset were dominated by stratiform rainfall while those of 2003 were dominated by convective rainfall.

IMRA rainfall estimates were validated both on hourly and daily basis for different spatial scales (4 km, 12 km, 20 km, and 100 km). Two sets of observed rainfall data were used in this validation: high-temporal-and-spatial resolutions NCEP stage IV gauge-adjusted radar rainfall data and high-quality daily rain gauge data. The hourly NCEP stage IV radar rainfall products were chosen as the primary ground-truth for the IMRA rainfall estimates because they are at similar spatial resolution (i.e., 4 km x 4 km) as the GOES IR data used for satellite rainfall estimation.

IMRA rainfall estimates are assessed by comparing rainfall data from gauge, radar, and satellite estimates and the streamflow predicted by Sacramento Soil Moisture Accounting (SAC-SMA) model with the observed data. Generally, the Slope technique provided good rainfall estimates for both stratiform and convective systems (i.e., 2002 and 2003 datasets respectively), while the Hessian technique provided good estimates for convective systems and significantly underestimated the stratiform rainfall (2002 dataset). However, the Slope technique performed slightly poorer than the Hessian technique for convective rainfall systems (i.e., 2003 dataset). Independent qualitative and quantitative analysis of the Hessian technique (Rozumalski, 2000) showed reasonable performance of the technique for well-defined and short duration convective systems. The Hessian technique was originally developed for intense convective systems, and hence the technique is expected to perform better during these events, although there has been overestimation of daily rainfall accumulations (e.g., Vicente et al., 1998; Rozumalski, 2000), which agrees with the results obtained in this study.

The use of microwave (MW) data as an adjustment factor generally led to underestimation of observed rainfall in both hourly and daily basis. This can be partly due to poor sampling frequency of microwave data (once or twice per day) as compared to hourly GOES IR data, and partly due to diurnal characteristics of rainfall system, such that precipitation occurs quite regularly during certain time

periods of the day over the study site, which can potentially be missed by the less frequent (once or twice per day) satellite acquiring MW data. The satellite can potentially be making overpasses at a time when it usually does not rain.

Driving the SAC-SMA model with IMRA rainfall estimates, instead of gauge rainfall did improve the model performance slightly, for the case when the basin was subdivided into 4 sub-basins defined by the same SAC-SMA model parameters partly because parameters could not be recalibrated due to a lack of observed streamflow data at sub-basin scale. Apparently it is possible to use such satellite rainfall estimates for hydrologic modeling in regions where no ground based rainfall measurements are available. Andersen et al. (2002) pointed out that improved simulation at sub-basin scale seems to depend partly on the precipitation input, and partly on the process relations, grid scale, and other types of input data and the calibration method. Hence, IMRA rainfall estimates can potentially improve model performance because hydrologic responses from a hydrologic model generally depends on the precipitation forcing, which are generally better if they are of relatively high spatial resolutions (i.e., satellite versus raingauges data) (Guetter et al., 1996; Tsintikidis et al., 1999).

Even though the WSR-88D stage III radar rainfall data can generally capture the spatial variability of precipitation fields, the accuracy of its rainfall depth depends on the storm type (convective or stratiform storms). The various errors associated with WSR-88D stage III data may be caused by the use of sparsely spaced point measurements from raingauges to correct for the bias of radar data, difficulty in identifying rainfall type resulting in use of wrong bias adjustment factors, errors in geo-referencing, sampling errors and errors due to radar data processing, such as averaging of overlapping radar data.

This research component involves: (a) assessing the accuracy of WSR-88D stage III radar rainfall data using point gauge rainfall data, (b) the development of Haar wavelet scheme to merge radar and gauged rainfall data by exploiting the strength of radar that captures the spatial variability of rainfall and the strength of raingauges that provide accurate measurements of mean rainfall depth, so that the underestimation of radar rainfall depths is corrected for while the spatial variability of the original radar data is maintained. The Haar wavelet was used because the wavelet coefficients serve as directional gradients of the rainfall process. The wavelet scheme and the Statistical Objective Analysis (SOA) scheme of Pereira et al. (1998) were compared in terms of individually merged rainfall data and the streamflow hydrographs simulated by the semi-distributed, physics-based rainfall-runoff model (DPHM-RS of Biftu and Gan; 2001, 2004) driven by these two datasets, (c) the suitability of operational WSR-88D stage III radar rainfall data over rain gauge data in basin-scale hydrologic modeling with respect to storm type and size, and (d) the effect of rainfall spatial variability, based on the modeling resolution of DPHM-RS, on streamflow prediction.

The analysis was carried out in the Blue River Basin (BRB) of Oklahoma on event basis because of the availability of radar rainfall estimates, topographical, land use/cover, solar energy, and meteorological data at a relatively long period (i.e., from 1994 to 2000). The WSR-88D's underestimation of precipitation was generally more pronounced during the cold season (September to February) normally dominated by stratiform storms than the warm season (March to August) normally dominated by convective storms. With respect to gauged data, the wavelet technique is generally better than SOA in predicting the mean field depths. However, it tends to slightly under-estimate while SOA tends to slightly over-estimate the standard deviation of radar rainfall data. Though the wavelet method may have an edge over SOA, more extensive testing are necessary before we can conclude which technique is better.

Radar data generally simulated more accurate runoff hydrographs than gauged data for convective storms but poorer for stratiform storms because radar significantly under-estimated stratiform storms. This implies that, for hydrologic applications, it is important to identify the storm types associated with the WSR-88D radar rainfall data because for convective rainfall cases, WSR-88D stage III radar rainfall data are generally useful for basin-scale hydrologic simulations because it can better capture both the depth and the spatial variability of precipitation than raingauge data, while for stratiform storms, WSR-88D stage III radar rainfall data tend to under-estimate the streamflow significantly unless the data were first corrected using rain gauge measurements. The problem of radar under-estimating rainfall generally grows with a decrease in storm magnitude, even for convective storms. Thus, storm size plays a significant role in the accuracy of WSR-88D radar rainfall.

The SOA and Wavelet data merging schemes substantially reduced radar's under-estimation of observed streamflow hydrographs for stratiform storms, but the adjustment seems to depend on how accurate are the depth measurements of gauges and whether radar data under-estimate the rainfall significantly, such as the case of stratiform storms. The results also indicate that a raingauge network of 6 gauges in 1233 km² is sufficient to improve the underestimation of radar rainfall data, and the improvement increases with increasing difference between gauged and radar rainfall depths. The results also show the general necessity of considering the spatial variability of precipitation data, particularly for convective storms that are highly variable spatially and so cannot be adequately represented by point measurements collected by rain gauges over a river basin. This justifies the expensive and tedious effort to account for the spatial variability of rainfall either via dense raingauge networks, radar meteorology, or meteorological satellites. Furthermore, besides distributed rainfall data, it is usually necessary discretizing a river basin into sub-basins of appropriate resolution so as to effectively handle the spatial variability of

rainfall.

5.2 Recommendations for Future Research

Even though IMRA gave encouraging results in Peace River Basin of Florida, USA, the improvement in the predicted streamflow was marginal when compared to hydrographs produced by gauged rainfall, and it was tested with GOES infrared (IR) data at 1-hour temporal resolution only. To adequately assess the potential of satellite rainfall estimates derived by IMRA in hydrologic modeling, we need to acquire GOES infrared (IR) data at 30-minutes temporal resolution, and data such as topographical, land use/cover, solar energy, and other hydro-meteorological data necessary for running more physics-based hydrologic models than the SAC-SMA model. If the aforementioned data are available, the following recommendations can be implemented to improve the quality of rainfall estimates from satellite data.

- (1) Develop techniques for identifying rainfall regime/type, preferably from satellite information, such as the convective/stratiform rain classification technique using microwave data and the 2A23 rain type product provided by **Precipitation Radar (PR)** on board the TRMM satellite (Grecu and Anagnostou, 2001), although both suffer from poor time resolution (i.e., once or twice per day);
- (2) Implement the IMRA-Slope method using GOES IR data at 30-minutes temporal resolution. The derived rainfall estimates should be assessed by driving distributed or semi-distributed physically based hydrologic models such as the DPHM-RS model (Biftu and Gan, 2001, 2004) to test the advantage offered by spatially distributed satellite rainfall data of high temporal resolution over gauged rainfall;
- (3) Further test the satellite rainfall estimation by the cloud growth technique of Vicente et al. (1998) modified by Boi et al. (2004), which requires GOES IR data at 30-minute temporal resolution because it compares cloud growth

between two consecutive IR images.

Lastly, the quality of raw WSR-88D stage III radar rainfall data and the subsequent merging of radar and raingauge data using wavelet or SOA schemes is affected by geo-referencing errors inherent with such radar rainfall data, sampling issues associated with different rainfall measurement technique between radar (i.e., areally averaged) and gauge (i.e., point observations) and its interpolated derivative. It is recommended that future work should try to quantify the amount of these errors and incorporate them in the analysis.

References

- Andersen, J., Dybkjaer, G., Jensen, K. H., Refsgaard, J. C., and Rasmussen, K. (2002), Use of remotely sensed precipitation and leaf area index in a distributed hydrological model. *J. of Hydrology*, 264, 34-50.
- Biftu, G. F., and Gan, T. Y. (2004), Semi-distributed, Hydrologic Modeling of Dry Catchment with Remotely Sensed and Digital Terrain Elevation Data. *Int. J. Remote Sensing*, 25(20), 4351-4379.
- Biftu, G. F., and Gan, T. Y. (2001), Semi-distributed, physically based, hydrologic modeling of the Paddle River Basin, Alberta, using remotely sensed data, *J. of Hydrology*, 244, 137-156.
- Boi, P., Marrocu, M., and Giachetti, A. (2004), Rainfall estimation from infrared data using an improved version of the Auto-Estimator Technique. *Int. J. Remote Sensing*, 25 (21), 4657-4673.
- Greco, M., and Anagnostou, E. N. (2001), Overland precipitation estimation from TRMM passive microwave observations. *J. of Applied Meteorology*, 40, 1367-1380.
- Guetter, A. K., Georgakakos, K. P., Tsonis, A. A. (1996), Hydrologic applications of satellite data 2. Flow simulation and soil water estimates. *J. Geophys. Res.*, 101, 26527-26538.
- Jain, A. K., (1989), *Fundamentals of Digital Image Processing*. Prentice Hall, 350 pp.
- Jayakrishnan, R., Srinivasan, R., and Arnold, J. G. (2004), Comparison of raingage and WSR-88D stage III precipitation data over the Texas-Gulf basin, *J. of Hydrology*, 292, 135-152.
- Rozumalski, R. A., (2000), A quantitative assessment of NESDIS Auto-Estimator. *Weather and Forecasting*, 15, 397-415.
- Tsintikidis, D., Georgakakos, K. P., Artan, G. A., and Tsonis, A. A. (1999), A feasibility study on mean areal rainfall estimation and hydrological response in the Blue Nile region using METEOSAT images. *J. of Hydrology*, 221, 97-116.

Vicente, G. A., Scofield, R. A., and Menzel, W. P. (1998), The operational GOES infrared rainfall estimation technique. *Bull. American Meteorological Soc.*, 79 (9), 1883-1898.